博士論文

Magnetic Rare-Earth Ion Doping Effect on Phase IV of Ce$_x$La$_{1-x}$B$_6$

(Ce$_x$La$_{1-x}$B$_6$ の IV 相への希土類磁性イオン添加効果)

近藤 晃弘

広島大学大学院先端物質科学研究科

2009 年 9 月

論 文 の 要 旨

氏 名　　近 藤 晃 弘

論 文 題 目　　Magnetic Rare-Earth Ion Doping Effect on Phase IV of Ce$_x$La$_{1-x}$B$_6$
（Ce$_x$La$_{1-x}$B$_6$ の IV 相への希土類磁性イオン添加効果）

1　背景と目的

　近年、Ce などの希土類イオンや U などのアクチノイドイオンを含む f 電子化合物において、軌道の自由度（多極子モーメント）が物性に大きな影響を及ぼすことが明らかとなった。この多極子モーメントが規則的に配列した秩序（多極子秩序）は、通常の磁性体では見られない異常な振る舞いを示すため、現在盛んに研究が行われている。

　ここ 10 年ほどの間に多極子秩序を示す物質は数多く発見されているが、その中でもわが国を中心に古くから研究されてきた有名な物質として CeB$_6$ がある。特に II 相は様々な異常を示すことから詳細な研究が行われ、高次の項である T_{xyz} 型の八極子モーメントがその異常に大きく関わっていることが明らかとなった。さらに、CeB$_6$ の低温・低磁場での様々な異常は磁気双極子、四極子、八極子の 3 つの自由度の共存・競合を起源とすることがわかった。

　CeB$_6$ の Ce を La で置換した Ce$_{0.75}$La$_{0.25}$B$_6$ において、IV 相と呼ばれる新たな相が 1996 年に発見された。現在、IV 相は $0.3 \leq x \leq 0.8$ において存在することがわかっている。IV 相では弾性定数 C_{44} が大きなソフト化を示す、I-IV 相転移温度（$T_{\mathrm{IV-I}}$）で磁化率がピークを示す、磁気抵抗が非常に小さいなど特徴的な振る舞いが見られる。IV 相については中性子散乱、NMR、μSR などのミクロな測定が盛んに行われたが、磁気秩序相であるという証拠は得られなかった。倉本らは IV 相が $T_\beta(\Gamma_{5u})$ 型の反強八極子 (AFO) 秩序であるとするモデルを提案し、IV 相の特徴の多くを説明することに成功した。一方、最近行われた共鳴 X 線散乱および中性子散乱の実験から、IV 相は $Q=(1/2\ 1/2\ 1/2)$ の長周期構造を持った長距離秩序であることが明らかになり、詳細な解析が解析が行われ、IV 相が T_β-AFO 秩序であることを支持する結果が得られた。以後、T_β-AFO 秩序が IV 相秩序変数の有力な候補となっている。しかしながら、T_β-AFO 秩序では Ce$_x$La$_{1-x}$B$_6$ に元来存在する複数の多極子相互作用を考慮していないなどいくつかの問題点が存在する。そこで、本研究では IV 相秩序変数に関する情報を得ることを目的として、IV 相に希土類磁性 (R) イオン (R =Nd、Pr) を添加した試料（Ce$_x$R$_y$La$_{1-x-y}$B$_6$ (x = 0.7, 0.65, 0.6, 0.5, 0.4)）を作製し、R イオン添加の影響を詳しく調べた。また、T_β-AFO 秩序により Ce$_x$La$_{1-x}$B$_6$ の全体像が説明可能かどうかを調べるため、T_β-AFO 秩序に複数の多極子相互作用を取り入れた 2 部分格子模型による分子場計算を行った。

2 結果と考察

2.1 複数の異なるタイプの多極子相互作用を取り入れた分子場計算

T_β-AFO 秩序に O_{xy}-AFQ、T_{xyz}-AFO 相互作用を加えていくと、計算から得られた磁気相図は反強磁性相の有無を除けば $x = 0.75$ および $x = 0.7$ の磁気相図をおおよそ再現する。しかしながら、磁化の温度依存性は O_{xy}-AFQ、T_{xyz}-AFO 相互作用を加えていくことにより T_β 相への転移温度で見られた IV 相を特徴づける磁化のカスプが消失し、T_β 相への転移後も温度降下に伴い増大することがわかった。この磁化の増大は T_β-AFO 秩序によって誘起された O_{xy} 型の強四極子（FQ）秩序が O_{xy}-AFQ 相互作用により容易に抑制されたためと考えられる。このように、IV 相を T_β-AFO 秩序としたときには、$Ce_xLa_{1-x}B_6$ の全体像を説明できないことを明らかとした。

2.2 IV 相への R イオン添加効果

$x \geq 0.6$ では R イオン添加により IV 相は急速に抑制され、III 相が安定化することがわかった。これは R イオン添加による III 相の安定化は R イオンが反強磁性相の形成に寄与していることを示唆している。また、T_{IV-I} は R イオン添加によりほとんど変化せず、T_N へ連続的にシフトしていくことが明らかとなった。これは IV 相と III 相の秩序変数の間には何らかの関係があることを示唆する結果である。一方、$x \leq 0.5$ では $x \geq 0.6$ の結果とは大きく異なり、T_{IV-I} が R イオン添加によって急激に上昇することがわかった。この結果は $x \leq 0.5$ では R イオン添加によって IV 相が安定化していること、さらに IV 相の性質が $x \sim 0.6$ を境に変化している可能性を示唆している。$x \sim 0.6$ では IV 相と III 相のエネルギー差が小さいため、R イオン添加によって IV 相が急速に抑制し III 相が安定化したと考えられる。Ce 濃度が薄まると IV 相と III 相のエネルギー差が大きくなっていくことから、$x \leq 0.5$ では IV 相への R イオン添加の本質、つまり R イオン添加による T_{IV-I} の増大が明瞭に観測されたと考ることができる。Nd、Pr 添加が共に T_{IV-I} を増大させることから、T_{IV-I} 増大の起源は R イオンの持つ磁気双極子モーメントである可能性が高い。もし $x \leq 0.5$ においても IV 相が T_β-AFO 秩序であるとするならば、この場合基底状態は非磁性の一重項であるため、R イオンの持つ磁気双極子モーメントは Γ_{5u} 型の八極子モーメントとは結合できず、T_{IV-I} は増大しないはずである。このように $x \leq 0.5$ では添加された R イオンの磁気双極子モーメントが IV 相を安定化することを見出し、IV 相を T_β-AFO 秩序とする従来のモデルでは、その説明が困難であることを指摘した。

3 まとめ

複数の多極子相互作用を取り入れた分子場計算、および IV 相への R イオン添加効果の結果から、少なくとも $x \leq 0.5$ では IV 相が T_β-AFO 秩序ではない可能性があることが明らかとした。本研究では IV 相秩序変数を決定するまでには至らなかったが、IV 相を理解する上で大きな進展があったと考える。今後、$x \leq 0.5$ における R イオン添加による T_{IV-I} 増大の起源を明らかにするため、中性子散乱や共鳴 X 線実験などのミクロな測定を行う必要がある。

目次

主論文

博士論文

Magnetic Rare-Earth Ion Doping Effect on Phase IV of $Ce_xLa_{1-x}B_6$

($Ce_xLa_{1-x}B_6$ の IV 相への希土類磁性イオン添加効果)

近藤 晃弘

広島大学大学院先端物質科学研究科

2009 年 9 月

Abstract

Recently, the importance of the orbital degrees of freedom (the multipole moment) has been clarified in the f-electron systems. In particular, the multipole ordering that the multipole moment orders spontaneously have been intensively studied because of the appearance of the unusual behaviors which have not known.

Recently, many compounds showing the multipolar ordering have been discovered. CeB_6 is one of the most famous compound which has been studied since 40 years ago. CeB_6 is the first example in which the octupole interaction is verified to play an essential role in the unusual antiferro-quadrupole (AFQ) ordered phase. CeB_6 shows the AFQ order at T_Q=3.3 K, the antiferro (AF) magnetic order at $T_N = 2.3$ K. These two phases are called as phases II and III, respectively. The paramagnetic phase is called as phase I. The unusual behaviors of this compound originate from the coexistence and competition of the different kinds of the interactions, $i.e.$, O_{xy}-type AFQ, T_{xyz}-AF octupolar (AFO), and AF magnetic interactions. Recently, a possibility of the pure octupolar ordering was pointed out in NpO_2. The physics of the octupolar ordering is the exciting theme in the f-electron systems.

In the course of the study of $Ce_xLa_{1-x}B_6$, a new phase called as phase IV was discovered. Phase IV exhibits the following unusual features. The magnetic susceptibility exhibits a peak at the IV-I transition temperature, T^{IV-I}. The elastic constant of the C_{44} mode exhibits a large softening in phase IV The magnetoresistance in phase IV is very small. Although the intensive studies by the neutron diffraction, NMR and μSR are performed, the evidence of the magnetic ordering could not be obtained. However, the recent resonant X-ray diffraction indicated that the long-range order(LRO) with $Q = (1/2\ 1/2\ 1/2)$ is realized in phase IV. Soon after their discovery of the LRO in phase IV, Kusunose and Kuramoto were able to explain their results by assuming the Γ_{5u}-type AFO order. Thus, the Γ_{5u}-type AFO ordering is said to be a strong candidate for the LRO in phase IV.

Although the Γ_{5u}-type AFO ordering is the most plausible candidate for the LRO in phase IV, there exist the difficulties which remain to be explained by the Γ_{5u}-type AFO ordering. Thus, the order parameter of phase IV is still controversial and further studies are necessary to clarify its nature.

In order to obtain the information on the order parameter of phase IV, we have studied $Ce_xR_yLa_{1-x-y}B_6$ ($x = 0.7, 0.65, 0.6, 0.5$ and 0.4) with $R =$ Pr and Nd up to $y = 0.1$. Although for $x \geq 0.6$ T_{IV-I} shows a small y dependence, T_{IV-I} for $x \leq 0.5$ shows a drastic enhancement by Pr and Nd doping. The results for $x \leq 0.5$ indicate that the order parameter in phase IV for $x \leq 0.5$ is coupled with the magnetic dipole moment of Pr and Nd ions. The ground state of the Γ_{5u}-type AFO ordered phase which is the nonmagnetic singlet cannot be coupled with the magnetic dipole moment of R ions. Thus, the present results strongly suggest that phase IV is different from the Γ_{5u}-type AFO ordering at least for $x \leq 0.5$.

We have also carried out the mean field calculation for the two-sublattice model in which the O_{xy}-AFQ, T_{xyz}-AFO, Γ_{5u}-type AFO, and AF exchange interactions are taken into account and discussed the effect of the above three interactions on the Γ_{5u}-type order. The magnetic phase diagram obtained by the calculation seems to reproduce those of $Ce_xLa_{1-x}B_6$. However, a peak of the magnetic susceptibility which is one of the most characteristic properties in phase IV disappears easily by introducing the O_{xy}-AFQ interaction as a result that which is because the O_{xy}-FQ order accompanied with the Γ_{5u}-AFO order is easily suppressed by the O_{xy}-AFQ interaction. Thus, it seems to be difficult to explain the overall properties in this system with phase IV by Γ_{5u}-AFO model.

Contents

Chapter 1

Introduction

1.1 Multipole ordering

1.1.1 $4f$-electron in the cubic crystalline electric field

In the $4f$-electron systems, in general, the electronic state is described by the total angler momentum, $J=L+S$ because the spin-orbit interaction is much larger than the effect of the crystalline electric field.

Here, we consider the case of Ce^{3+} ($4f^1$, $L = 3$, $S = 1/2$) ion. In the case of $L = 3$ and $S = 1/2$, J is 5/2 or 7/2. For Ce^{3+} ion, $J = 5/2$ (sixfold degenerate) is known to be the ground J multiplet with a $J = 7/2$ excited state which is situated ~ 2700 K above the $J = 5/2$ multiplet. The sixfold degenerate $J = 5/2$ multiplet is split due to the cubic crystalline electrical field (CEF) effect. The CEF Hamiltonian in the cubic symmetry, $\mathcal{H}_{CEF}$ is given by

$$\mathcal{H}_{CEF} = B_4(O_4^0 + 5O_4^4) + B_6(O_6^0 - 21O_6^4), \tag{1.1}$$

where B_4 and B_6 are are factors which determine the scale of the CEF splittings and O_l^m are the Stevens' operators. O_4^0, O_4^4, O_6^0 and O_6^4 are expressed by using J_z, J_+ and J_- as follows.

$$
\begin{cases}
O_4^0 = 35J_z^4 - [30J(J+1) - 25]J_z^2 - [6J(J+1) - 3J^2(J+1)^2] \\
O_4^4 = \dfrac{1}{2}(J_+^4 + J_-^4) \\
O_6^0 = 231J_z^6 - 105[3J(J+1) - 7]J_z^4 + [105J^2(J+1)^2 - 525J(J+1) + 294]J_z^2 \\
\qquad - [5J^3(J+1)^3 - 40J^2(J+1)^2 + 60J(J+1)] \\
O_6^4 = \dfrac{1}{4}[11J_z^2 - \{J(J+1) + 38\}](J_+^4 + J_-^4) + \dfrac{1}{4}(J_+^4 + J_-^4)[11J_z^2 - \{J(J+1) + 38\}].
\end{cases}
\tag{1.2}
$$

In the case of $J = 5/2$, $\mathcal{H}_{CEF}$ are given by using $|J, m\rangle$ as the basis functions as follows.

$$
\mathcal{H}_{CEF} =
\begin{array}{c}
\langle +\frac{5}{2}| \\
\langle +\frac{3}{2}| \\
\langle +\frac{1}{2}| \\
\langle -\frac{1}{2}| \\
\langle -\frac{3}{2}| \\
\langle -\frac{5}{2}|
\end{array}
\begin{pmatrix}
60B_4 & 0 & 0 & 0 & 60\sqrt{5}B_4 & 0 \\
0 & -180B_4 & 0 & 0 & 0 & 60\sqrt{5}B_4 \\
0 & 0 & 120B_4 & 0 & 0 & 0 \\
0 & 0 & 0 & 120B_4 & 0 & 0 \\
60\sqrt{5}B_4 & 0 & 0 & 0 & -180B_4 & 0 \\
0 & 60\sqrt{5}B_4 & 0 & 0 & 0 & 60B_4
\end{pmatrix}
$$

with column headers $|+\frac{5}{2}\rangle$, $|+\frac{3}{2}\rangle$, $|+\frac{1}{2}\rangle$, $|-\frac{5}{2}\rangle$, $|-\frac{3}{2}\rangle$, $|-\frac{1}{2}\rangle$.

The $J = 5/2$ ground multiplet splits into the Γ_7 doublet and Γ_8 quartet in the cubic CEF. The eigen values and eigenfunctions are obtained by diagonalizing the above Hamiltonian. We define the wave functions for Γ_8
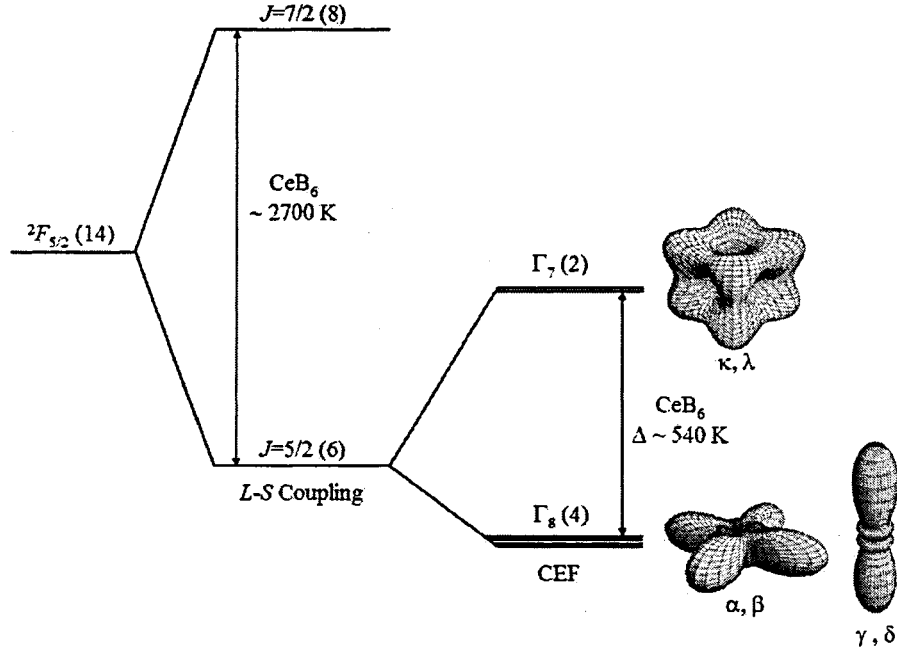
Fig. 1.1   Energy level scheme for the Ce^{3+} ion in the cubic crystalline electric field and the charge clouds of the Γ_8 and Γ_7 wave functions. In the case of CeB_6, the splitting of the $J=5/2$ multiplet by CEF $\Delta \sim 540$ K. The splitting between $J=5/2$ and $J=7/2$ due to the L-S couplings is ~ 2700 K as descried latter.

quartet (α, β, γ, δ) and Γ_7 doublet (κ, λ) as follows.

$$\Gamma_8 \text{ quartet} \begin{cases} |\alpha\rangle = \sqrt{5/6}\,|5/2\rangle + \sqrt{1/6}\,|-3/2\rangle \\ |\beta\rangle = \sqrt{5/6}\,|-5/2\rangle + \sqrt{1/6}\,|3/2\rangle \\ |\gamma\rangle = |1/2\rangle \\ |\delta\rangle = |-1/2\rangle \end{cases} \qquad (1.3)$$

$$\Gamma_7 \text{ doublet} \begin{cases} |\kappa\rangle = \sqrt{1/6}\,|5/2\rangle - \sqrt{5/6}\,|-3/2\rangle \\ |\lambda\rangle = \sqrt{5/6}\,|-5/2\rangle - \sqrt{1/6}\,|3/2\rangle \end{cases} \qquad (1.4)$$

Here, we assume that the CEF ground state is the Γ_8 quartet. In CeB_6, the CEF ground state is known to be the Γ_8 quartet and the excited Γ_7 doublet is situated above ~ 540 K as will be described later [1]. Figure 1.1 shows the energy level scheme for the Ce^{3+} ion in the CEF and the charge clouds of the Γ_8 and Γ_7 wave functions.

In general, within the n-th degenerate state, the number of independent operators is $n^2 - 1$. Thus, the Γ_8 quartet has 15 independent operators. When we regard the multipole moments as the independent operators, the multipole moments in the Γ_8 quartet system are three dipoles, five quadrupoles and seven octupole moments [2].

1.1.2 Electrical quadrupole moment

The orbital motion of the $4f$-electron is not free in the crystal. Then, the charge distribution of the $4f$-electron is expected to be anisotropic so as to reduce the Coulomb repulsion from the surrounded ions. The anisotropic charge distributions is expressed by the quadrupole moment [3].

First, we assume that there exists a localized $4f$ electron at the origin. We define the charge distribution of this $4f$ electron and the electrostatic potential at point as $\rho(\vec{r}')$ and $\varphi(\vec{r})$. Then, $\varphi(\vec{r})$ can be expressed as

follows.

$$\varphi(\vec{r}) = \int \frac{\rho(\vec{r}')}{|\vec{r} - \vec{r}'|} d\vec{r}'$$

$$= \sum_{l=0}^{\infty} \sum_{m=-l}^{l} \int \rho(\vec{r}') \frac{r'^l}{r^{l+1}} \frac{4\pi}{2l+1} Y_{lm}^*(\theta, \phi) Y_{lm}(\theta', \phi') d\vec{r}'$$

$$= \sum_{l=0}^{\infty} \varphi^{(l)},$$
(1.5)

where

$$\varphi^{(l)} = \frac{1}{r^{l+1}} \sum_{m=-l}^{l} \sqrt{\frac{4\pi}{2l+1}} Q_m^{(l)} Y_{lm}^*(\theta, \phi)$$

$$Q_m^{(l)} = \int \rho(\vec{r}') r'^l \sqrt{\frac{4\pi}{2l+1}} Y_{lm}(\theta', \phi')$$
(1.6)

and $Y_{lm}(\theta, \phi)$ is surface harmonics. $Q_m^{(l)}$ corresponds to the 2^l-th electrical multipole moment. $Q_m^{(l)}$ has the $2l + 1$ independent components. Thus, the quadrupole moment in the case of $l = 2$ has five independent components.

On the other hand, $Q_m^{(l)}$ is the basis of the irreducible representation in rotation group. Considering $Q_m^{(l)}$ in the CEF, it is necessary to transform the representation in rotation group into the other representation which has the same symmetry as the crystalline field. Here, we assume that the symmetry around a rare-earth ion is represented by cubic-symmetry group O_h. Then, $Q_m^{(l)}$ is transformed into five independent components which has the same conversion property as the irreducible representation in O_h group. As a result, the quadrupole moment is represented as follows.

$$\Gamma_3 - \text{symmetry} \begin{cases} Q_u & = Q_0^{(2)} \\ Q_v & = \frac{1}{\sqrt{2}}(Q_2^{(2)} + Q_{-2}^{(2)}) \end{cases}$$
(1.7)

$$\Gamma_5 - \text{symmetry} \begin{cases} Q_\xi & = \frac{i}{\sqrt{2}}(Q_1^{(2)} + Q_{-1}^{(2)}) \\ Q_\eta & = -\frac{1}{\sqrt{2}}(Q_1^{(2)} - Q_{-1}^{(2)}) \\ Q_\zeta & = \frac{i}{\sqrt{2}}(Q_2^{(2)} + Q_{-2}^{(2)}) \end{cases}$$
(1.8)

Next, we find the expectation value of the quadrupole moments on f-electron wave functions expressed by $|J, m\rangle$. In this case, the quadrupole moments can be represented by J_x, J_y and J_z by using the Stevens equivalent operator method. Finally, the quadrupole moments is given as

$$\Gamma_3 - \text{symmetry} \begin{cases} O_2^0 & = \frac{1}{2}\{3J_z^2 - J(J+1)\} \\ O_2^2 & = \frac{\sqrt{3}}{2}(J_x^2 - J_y^2) \end{cases}$$
(1.9)

$$\Gamma_5 - \text{symmetry} \begin{cases} O_{xy} & = \frac{\sqrt{3}}{2}(J_x J_y + J_y J_x) \\ O_{yz} & = \frac{\sqrt{3}}{2}(J_y J_z + J_z J_y) \\ O_{zx} & = \frac{\sqrt{3}}{2}(J_z J_x + J_x J_z). \end{cases}$$
(1.10)

Figure 1.2 shows the schematic pictures of components of quadrupole moments [27].

(a) O_2^0 (b) O_2^2 (c) O_{xy}

(d) O_{yz} (e) O_{zx}
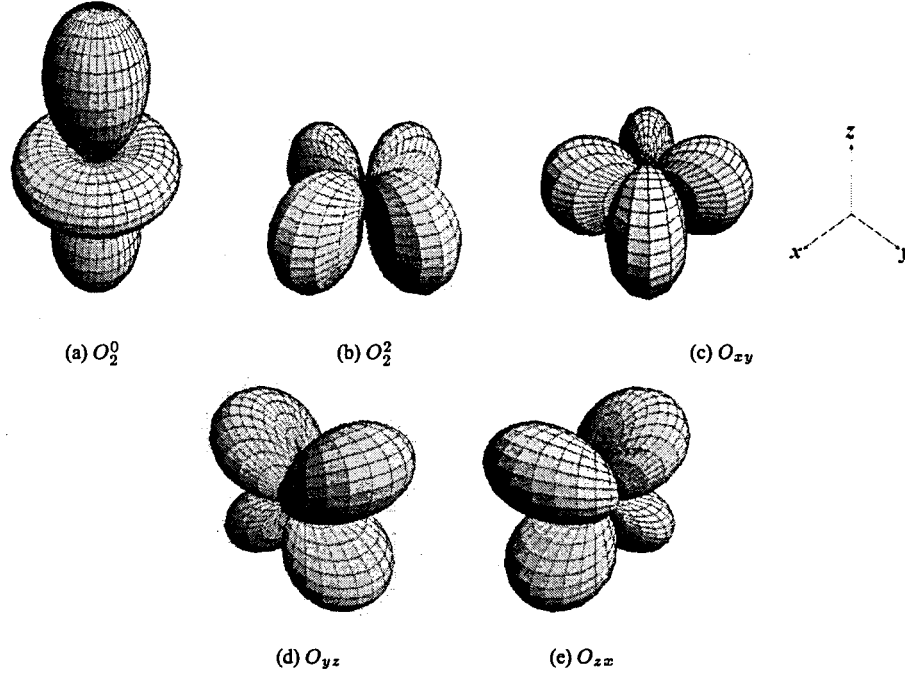
Fig. 1.2   Schematic pictures of components of quadrupole moments.

Quadrupolar interaction [4,5]

The quadrupolar ordering is a phenomenon that the quadrupole moment orders spontaneously. The quadrupolar ordering takes place by the quadrupolar interaction if there exists the degeneracy of the orbital degrees of freedom in the ground state of the CEF such as Γ_8 quartet. The quadrupolar interaction, $\mathcal{H}_Q$ is written as follows.

$$\mathcal{H}_Q = -K_3 \sum_{i,j} [O_2^0(i)O_2^0(j) + 3O_2^2(i)3O_2^2(j)]$$

$$- K_5 \sum_{i,j} [O_{xy}(i)O_{xy}(j) + O_{yz}(i)O_{yz}(j) + O_{zz}(i)O_{zz}(j)], \tag{1.11}$$

where K_3 and K_5 are the magnitudes of the quadrupole interactions.

When $K_\Gamma > 0$, the ferro-quadrupolar (FQ) ordering takes place and when $K_\Gamma < 0$, the antiferro-quadrupolar (AFQ) ordering takes place. Figure 1.3 shows the schematic picture of the O_{xy}-type FQ and AFQ ordering. When the ground state of the cubic CEF is the Γ_8 quartet, the competition between the quadrupolar and magnetic interaction exists. If the quadrupolar ordering takes place at higher temperature, the magnetic ordering should take place at lower temperature in order to release two-fold degeneracy of the spin degrees of freedom. When the FQ ordering takes place, the collinear spin ordering may take place. When AFQ ordering takes place, the non-collinear spin ordering is expected to appear. On the other hand, if the magnetic moment orders at high temperature, the quadrupolar ordering is hard to take place because the orbital degrees of freedom disappears due to the strong spin-orbit interaction.

Characteristic of AF quadrupolar ordering

We summarize the characteristic properties of the AFQ ordering in the case where the CEF ground state is the quartet [5].

Ferro Quadrupolar Ordering   Anti-ferro Quadrupolar Ordering
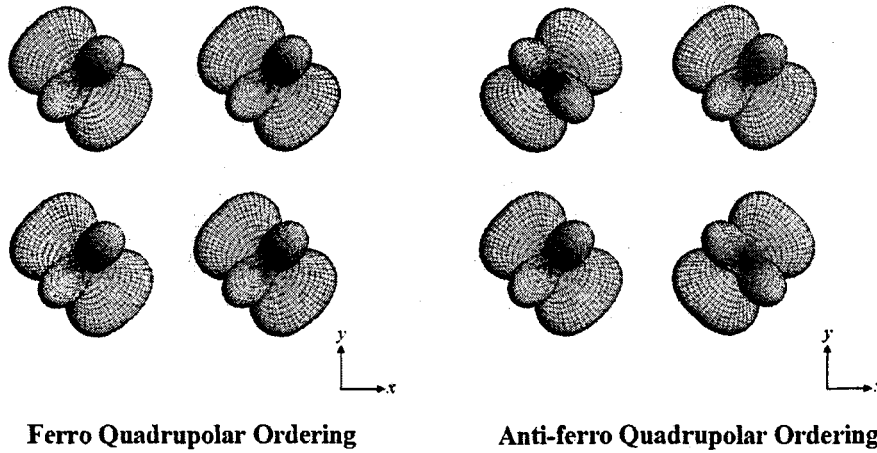
Fig. 1.3 Schematic pictures of the O_{xy}-type FQ and AFQ ordering.

(1) The specific heat at T_Q shows a large and sharp peak.

This is because the quartet in paramagnetic region splits into two doublets below T_Q and then the entropy of $R \ln 4$ is released at T_Q.

(2) Since the ground state below T_Q is doublet, the two-fold degeneracies of the spin degrees of freedom remains below T_Q. Therefore, the microscopic measurements such as neutron scattering or NMR experiment cannot observe the AFQ ordering at H=0. However, the direct observation of this ordering by the microscopic measurements is possible by applying magnetic fields because of the appearance of field induced AF magnetic components.

(3) The ground state of the AFQ ordered phase has the spin degrees of freedom. Then, with decreasing temperature, the AF magnetic ordering should takes place at T_N which is lower than T_Q. The entropy of $R \ln 2$ is released below T_N. In this case, the AF structure is complicated due to the effect of the AFQ ordering because the quadrupole moment has the anisotropic charge cloud and this anisotropy determines the direction of the spin alignment through the spin-orbit coupling. In general, the non-collinear spin ordering is expected to appear because the quadrupole moment is orthogonal to each other.

(4) The elastic constant below T_Q shows the same behavior as the parallel and perpendicular magnetic susceptibilities in the AF magnetic state below T_N.

Here, We consider the mechanism of (2) taking the O_2^0-type AFQ ordering as an example.

Using the wave function in (1.3), the expectation value of J_z is as follows.

$$\langle \alpha | J_z | \alpha \rangle = \frac{11}{6} \ , \ \langle \beta | J_z | \beta \rangle = -\frac{11}{6} \ , \ \langle \gamma | J_z | \gamma \rangle = \frac{1}{2} \ , \ \langle \delta | J_z | \delta \rangle = -\frac{1}{2}$$

Figure 1.4 shows the magnetic field dependence of the energy levels for the O_2^0-type AFQ ordering case. There exists two-fold degeneracy in the ground state of the AFQ ordered state at H=0. With increasing magnetic field, two-fold degeneracy of the spin degrees of freedom shows the Zeeman splittings, and the saturated magnetization of A and B sublattice become 11/6, 1/2, respectively. Then, the whole magnetization of this system is $1\mu_B$/Ce (=$g_J 1/2$ (11/6+1/2) =6/7×1/2 (11/6+1/2) =1). On the other hand, in the finite magnetic field, the difference of the magnetization between two sublattice is $4/7\mu_B$/Ce (=$g_J 1/2$ (11/6-1/2) =6/7×1/2 (11/6-1/2) =4/7). This means that A and B sublattice have the staggered magnetization, M_{AF}=$4/7\mu_B$/. Thus, there exists M_{AF} in the finite magnetic field but not exist in the zero magnetic field. M_{AF} and the uniform magnetization, M_U show the field dependence following the Brillouin function because the paramagnetic state is realized at H=0. M_{AF} induced by the magnetic field can be observed in the neutron scattering or NMR. In the case of the
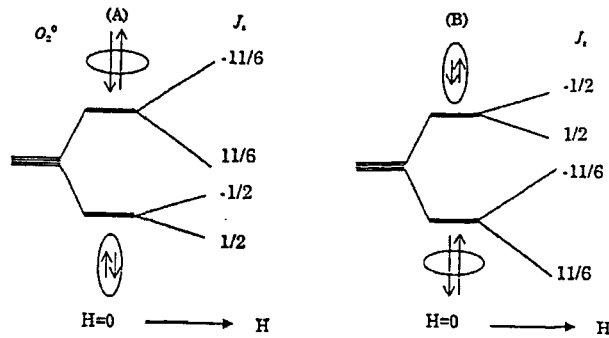
Fig. 1.4   Magnetic field dependence of the energy levels for the O_2^0-type AFQ ordering case [5].
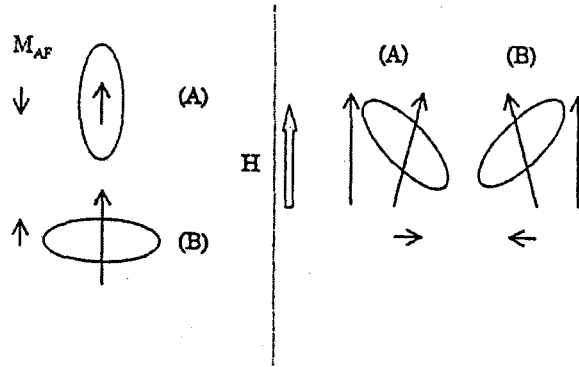
Fig. 1.5   (a) O_2^0 and (b) O_{xy} AFQ moment in magnetic field along the z direction [5]. In (a), M_{AF} is induced by the magnetic field parallel to the magnetic field but in (b) it is perpendicular to the field.

O_2^0 AFQ ordered state, M_{AF} is parallel to the magnetic field direction. In the case of the O_{xy} AFQ ordered state, M_{AF} is also perpendicular to the magnetic field as shown in Fig.1.5. This is because the orbital moment is easy to be induced along the direction perpendicular to the plane of the orbital motion.

One of the most famous compound showing the AFQ ordering is CeB_6. The AFQ ordered phase in CeB_6 will be described in the next section. In addition, recently, many compounds showing the AFQ ordering ($TmTe$ [6], DyB_2C_2 [7], $PrPb_3$ [8] and $PrOs_4Sb_{12}$ [9] etc.) have been discovered and studied extensively.

1.1.3 Magnetic octupole moment

Magnetic multipole moments is defined by the multipole expansion of vector potential as well as electrical multipole moments defined by the multipole expansion of electrostatic potential [10, 11].

Electromagnetics says that the existence of magnetic monopoles has never confirmed. Thus, the magnetic dipole moments is the lowest order moment in the magnetic multipole expansion. The localized $4f$ electrons has no magnetic quadrupole moments because the space inversion symmetry of these moments is not broken. Thus, the magnetic octupole moments corresponds to the second order moment in the magnetic multipole expansion.

When the $4f$ electron is widely distributed in the CEF, the situation where the upward or downward spins partly exists in the $4f$ electron is considered. This magnetic moment distribution is expressed by the octupole moment. Although the octupole moments has localized magnetic moments, the sum of these magnetic moments is zero. The octupole moments is rank-3 tensors and has seven independent components. In the case of where the $4f$ ion exists in cubic-symmetry group O_h, the octupole moments is represented by equivalent operator in
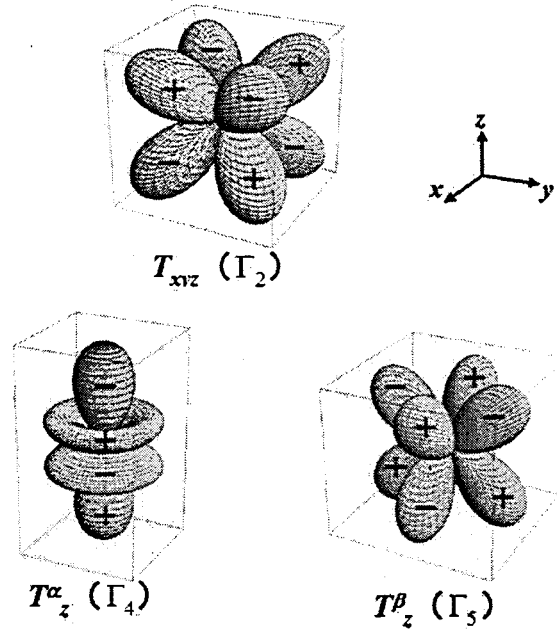
Fig. 1.6 Schematic pictures of components of octupole moments. As for Γ_4 and Γ_5 type octupole moments, the z components of octupole moments is only shown. The sign in this figure shows the polarization of localized magnetic moment.

Table 1.1. Figure 1.6 shows the schematic pictures of components of octupole moments.

Recent studies of the multipole moment have been shown that there exists the RKKY interaction between the quadrupole moments. It has been considered that the octupole moments has the RKKY type interaction as well as the quadrupole moments. In general, the multipole moments of higher order such as the octupole moments is weak in classical physics. However, in the case of the RKKY interaction originating from the mixing between $4f$ and conduction electrons, it has a possibility that the all kinds of multipole interaction is equally the same strengthIn CeB$_6$, the octupole moments plays an important role, as described latter.

Since the octupole moments has no net magnetic moment, it is difficult to observe them by using the general method to observe the magnetic moments. In addition, the external field to respond the octupole moment has never confirmed, so that the direct observation of the octupole moments is quite difficult.

On the other hand, Murakami et al. developed resonant x-ray scattering (RXS) in 1995 [12]. RXS makes the direct observation of orbital ordering possible. Recently, it turns out that RXS is very useful for the observation

Irreducible representation	Octupole operator
Γ_2	$T_{xyz} = \frac{\sqrt{15}}{6}\overline{J_xJ_yJ_z}$
Γ_4	$T_x^\alpha = \frac{1}{2}(2J_x^3 - \overline{J_xJ_y^2} - \overline{J_z^2J_x})$
	$T_y^\alpha = \frac{1}{2}(2J_y^3 - \overline{J_yJ_z^2} - \overline{J_x^2J_y})$
	$T_z^\alpha = \frac{1}{2}(2J_z^3 - \overline{J_zJ_x^2} - \overline{J_y^2J_z})$
Γ_5	$T_x^\beta = \frac{\sqrt{15}}{6}(\overline{J_xJ_y^2} - \overline{J_z^2J_x})$
	$T_y^\beta = \frac{\sqrt{15}}{6}(\overline{J_yJ_z^2} - \overline{J_x^2J_y})$
	$T_z^\beta = \frac{\sqrt{15}}{6}(\overline{J_zJ_x^2} - \overline{J_y^2J_z})$

Table. 1.1 The octupole moments listed as the irreducible representation in O_h group. Here, $\overline{J_xJ_yJ_z} = J_xJ_yJ_z + J_yJ_zJ_x + J_zJ_xJ_y$ [2]

of the multipole moments of higher order such as the octupole moments. In fact, the RXS measurements show that Γ_5-type octupole ordering is realized in NpO_2 [13].

Presently, the possibility of octupole ordering has been discussed in URu_2Si_2 [14], $SmRu_4P_{12}$ [15] and $Ce_xLa_{1-x}B_6$.

1.2 CeB$_6$

1.2.1 Outline of CeB$_6$

CeB$_6$ crystallizes into the cubic CaB$_6$ structure as shown in Fig.1.7. The cerium ions are situated on a simple cubic lattice, while the boron atoms form an octahedron around the center of the cubic cell.
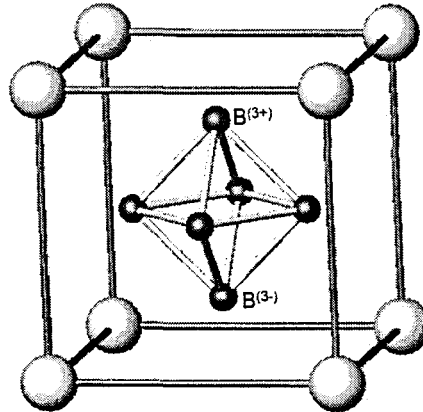
Fig. 1.7 Crystal structure of CeB$_6$. The cerium ions are sited on a simple cubic lattice, while the boron atoms form an octahedron around the center of the cubic cell.

As previously mentioned, the CEF ground state of CeB$_6$ is the Γ_8 quartet and the Γ_7 doublet lies about 540 K from Γ_8 quartet ground state. Therefore, the low temperature properties of this compound are dominated by the Γ_8 quartet.

Figure 1.8 shows the magnetic phase diagram of CeB$_6$ [16–18]. CeB$_6$ has three phases as follows.

- phase I : paramagnetic phase
- phase II : anti-ferro quadrupole (AFQ) ordered phase
- phase III : AFQ ordered state+anti-ferro (AF) magnetic state

Phase I is the paramagnetic state. Phase II is the anti-ferro quadrupole (AFQ) ordered state. Phase III is the anti-ferro (AF) magnetic state dominated by the AFQ ordering in phase II. The wave vector in phase II is Q=(1/2, 1/2, 1/2) as shown in Fig.1.9 (b) [17]. Phase III consists of three equivalent domains defined as K_{xy}, K_{yz} and K_{zz} at zero magnetic field. The non-collinear 2-k-k' antiferro-magnetic structure is realized in a single domain state. Magnetic wave wave vector in phase III are k_1=(1/4, 1/4, 0), k_1'=(1/4, 1/4, 1/2), k_2=(1/4, -1/4, 0), k_2'=(1/4, -1/4, 1/2) as is shown in Fig.1.9 (a) [17]. Magnetic moment in the K_{xy} domain is along the two-fold axis in the xy plane. For $H \parallel$ [111], phase III' which is characterized by a single-k-k' ordering vector exists in an intermediate region between phase III and II.

1.2.2 Historical background of CeB$_6$

Here, we briefly survey the history of CeB$_6$ to clarify how CeB$_6$ has attracted so many physicists. The history of CeB$_6$ is divided into 3 stages.

The first stage : Studies using polycrystals (1967~1976)

Paderno et al. first reported the magnetic susceptibility of the polycrystal of CeB$_6$ in 1967. Gaballe et al. measured the magnetization of CeB$_6$ and found that the magnitude of the magnetization for T =1.3K and H =50kOe was 0.56μ_B/Ce in 1968 [19]. Nickerson and White analyzed the magnetic susceptibility of CeB$_6$
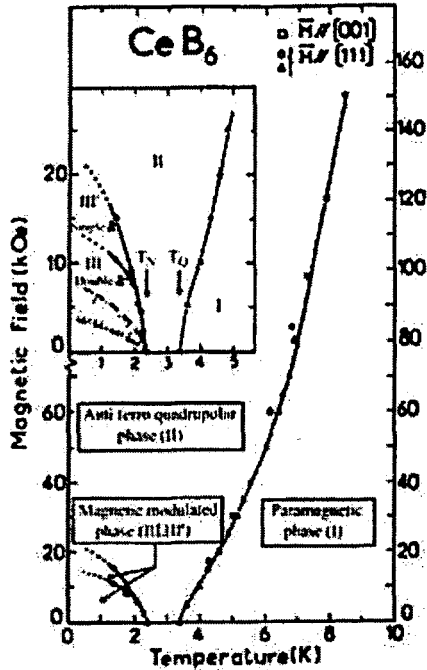
Fig. 1.8   Magnetic phase diagram of CeB$_6$ [16].
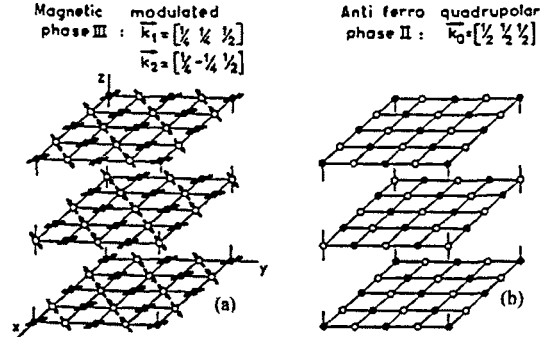
Fig. 1.9   Magnetic structures of phase III and II [17].
(a) Magnetic structure of phase III (k_1 = [1/4, 1/4, 1/2], k_2 = [1/4, −1/4, 1/2], k_1' = [1/4, 1/4, 0], k_2' = [1/4, −1/4, 0]). (b) AFQ structure of phase II (k_0 = [1/2, 1/2, 1/2]).

and proposed that the Γ_7 doublet is the ground state and the Γ_8 quartet is situated above ~75K in 1969 [20]. These experiments and analysis strongly suggested that the CEF ground state of CeB$_6$ was the Γ_7 doublet because the saturation magnetization for the Γ_7 state is estimated as 0.71μ_B/Ce from gJ_z=6/7×5/6μ_B/Ce.

Figure 1.10 shows the temperature dependence of the inverse magnetic susceptibility, χ^{-1} reported by Paderno et al.. The dashed and solid lines show the fitting curves obtained from the model proposed by Nickerson and White [20]. The closed circles are the experimental data of the magnetic susceptibility of CeB$_6$ [19]. The paramagnetic Curie temperature, θ_p estimated from χ^{-1} of CeB$_6$ in the high temperature region was ~60 K. Furthermore, χ^{-1} of CeB$_6$ decrease largely with decreasing temperature and simple Curie Weiss law was not observed. These behaviors were ascribed to the CEF energy level scheme that the ground state is Γ_7 doublet and the excited state is Γ_8 quartet and the splitting between the Γ_7 doublet and Γ_8 quartet, Δ is ~70 K. Nickerson and White performed the fitting of χ^{-1} assuming the Γ_7 ground state. They noted the anisotropic wave function of the Γ_7 doublet and Γ_8 quartet in Fig.1.11 and assumed that the effective intersite exchange interaction for Γ_7-Γ_7 is different from that for Γ_8-Γ_8. Namely, they assumed that the indirect exchange interaction between Γ_8 excited state is larger than that between Γ_7 ground state. As a result, they obtained the best fitting curve which corresponds to the solid line in Fig.1.10 and Δ ~75 K.

In 1972, Lee and Bell reported the temperature dependence of the specific heat at T~25 K and H=0 [21]. Figure 1.12 shows the temperature dependence of the specific heat of CeB$_6$. They found two peaks in the temperature dependence of the specific heat. Very large and sharp peak was observed at T ~2.31 K, and the other small peak at T ~3.3 K. They considered that the small tiny peak at 3.3 K originated from the impurity phase.

The second stage : Studies using single crystals (1978~1987)

Ten years after the study of the poly crystals, the single crystals of CeB$_6$ was made in Japan and Germany independently. Particularly, the single crystals made in Tohoku University was large with a high quality. Thus, CeB$_6$ had been intensively studied by Kasuya's group in Tohoku University.

In 1980, Takase et al. measured the electrical resistivity, ρ of CeB$_6$ [16]. Figure 1.13 shows the temperature
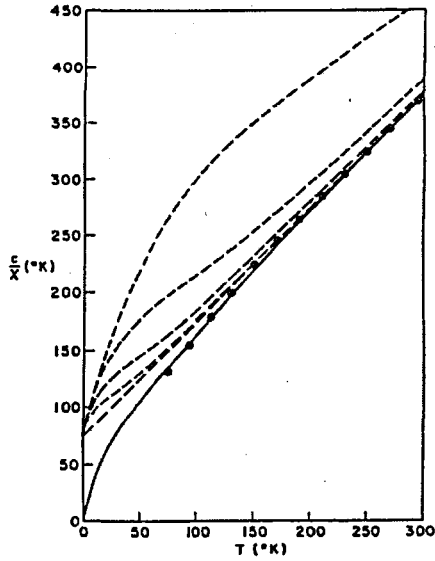
Fig. 1.10 Temperature dependence of the inverse magnetic susceptibility. [20]The various dashed and solid lines correspond to the calculated results by Nickerson and White. The closed circles correspond to the experimental results measured by Gaballe *et al.* [19].
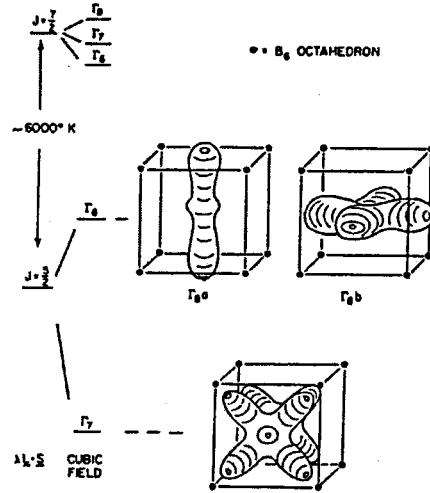
Fig. 1.11 Energy level scheme for Ce³⁺ ion in a cubic CEF [20].
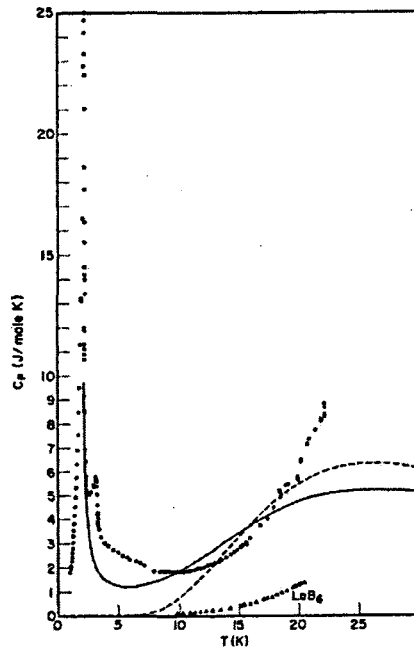
Fig. 1.12 Temperature dependence of the specific heat at $T \sim 25K$ and $H=0$ measured by Lee and Bell [21]

(T) dependence of ρ of CeB₆. ρ of CeB₆ at zero magnetic field shows the log T dependence even without subtracting the contribution from the electron-phonon scattering to ρ. This log T dependence of ρ was ascribed to the Kondo effect. Now, CeB₆ is known as the typical dense Kondo compound.
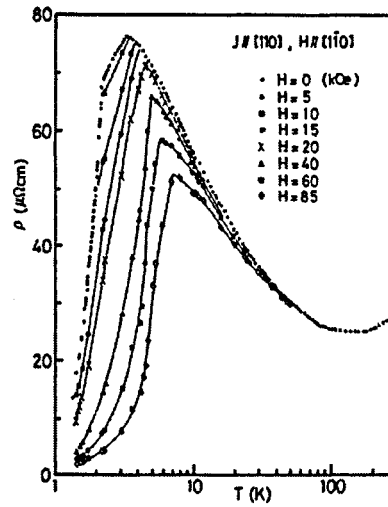
Fig. 1.13   Temperature dependence of the electrical resistivity of CeB_6 [16].
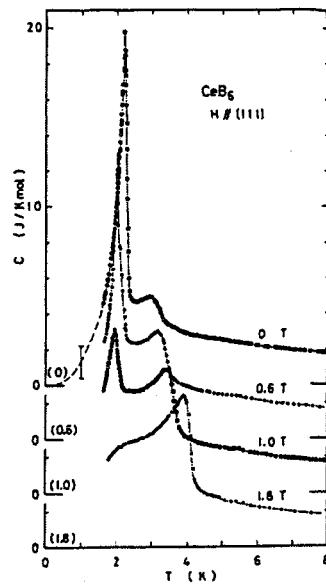
Fig. 1.14   Temperature dependence of the the specifi c heat of
CeB_6 for $H \parallel$ [111] [22].
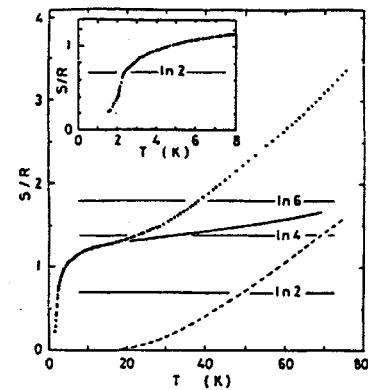
Fig. 1.15   Temperature dependence of the entropies of CeB_6
at zero fi eld [22]. the solid line corresponds to the
magnetic entropy of CeB_6 at zero fi eld.

At zero magnetic field, two kinks are observed in Fig.1.13. The kink at 3.3 K corresponds to the phase transition I-II, T_Q. The other one at 2.3 K corresponds to the phase transition II-III, T_N and ρ shows a drastic decrease below 2.3 K. The anomaly at T_Q becomes sharp with increasing magnetic field, while T_N disappears above 10 kOe.

In the same year, Fujita *et al.* measured the specific heat under the magnetic field [22]. Figure 1.14 shows the T dependence of the the specific heat, C of CeB_6 for $H \parallel$ [111]. They observed two peaks as was reported by Lee and Bell. However, they found that a small peak at $\sim$3.3K grows and shifts to the higher temperature with increasing magnetic field. Thus, the small peak at T $\sim$3.3K was found to be intrinsic in CeB_6. Figure 1.15 shows the T dependence of the entropy, S at zero magnetic field. The magnetic entropy, S_{mag} of CeB_6 at
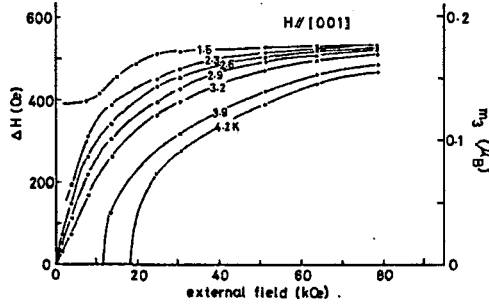
Fig. 1.16 Magnetic field dependence of ΔH for $B^{(3+)}$ and $B^{(3-)}$ site for $H \parallel [001]$ [26].
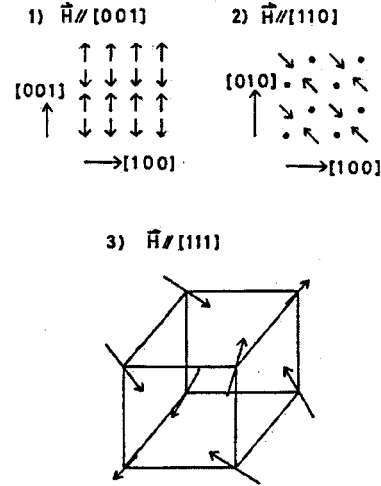
Fig. 1.17 Proposed spin structure of the AF magnetic moment in phase II for $H \parallel [001]$, $H \parallel [110]$ and $H \parallel [111]$. For $H \parallel [110]$, the solid dots show no AF magnetic moment on these sites [26].

zero magnetic field was obtained from the magnetic specific heat by subtracting the specific heat of LaB₆ from that of CeB₆. Here, the phonon contribution of CeB₆ was assumed to be the same as that of LaB₆. S_{mag} of CeB₆ was $R \ln 2$ at $T_N = 2.3$ K. Here, R denotes the gas constant. This suggested that the ground state was the Γ_7 doublet. Furthermore, S_{mag} was ~0.88R at T_Q and is $1.39R(R \ln 4)$ at $T \sim 33$ K. At high temperature of ~70 K, S_{mag} reaches to $R \ln 6$, which was expected from $^2F_{5/2}$ multiplet. The results were explained by the Γ_7 doublet with the Γ_7 excited state which is situated ~ 70 K above the Γ_7 ground state.

The magnetization, M was also investigated [23,24]. The magnitude of M at H_c^{III-II} was ~ 0.7μ_B/Ce at $T = 1.4$ K. 0.7μ_B/Ce is close to 0.71μ_B/Ce expected for the Γ_7 ground state. 1.54μ_B/Ce is expected for the Γ_8 ground state. Thus, the Γ_7 ground state and Δ_7^8 ~70 K became believed to be the correct CEF energy level scheme.

In 1983, an important pioneering work on CeB₆ was done by Ohkawa [28]. He proposed that the Γ_8 quartet is the ground state and phase II is the orbital ordered state, although the ground state of the CEF was believed to be the Γ_7 doublet at that time. Furthermore, he could explain the unusual T_Q with increasing magnetic field by considering the higher coupling between orbital and spin.

In 1984, the inelastic neutron scattering measurement was performed by Zirngiebl et al. [1]. They found that the Γ_8 quartet is the ground state and $\Delta_8^7 \sim 540$ K. After the confirmation of the CEF level scheme, the earlier experimental results were reconsidered.

In 1983, the appearance of the magnetic field induced AF components (M_{AF}) was discovered in phase II by the NMR experiment performed by Takigawa et al. [26] and the neutron scattering measurement performed by Rossat-Mignod et al.. However, the AF magnetic structures proposed by Takigawa and Rossat-Mignod were different.

In 1984, Rossat-Mignod proposed that the O_{xy}-AFQ ordering with $Q=[1/2,1/2,1/2]$ is realized in phase II.

(a) The easy axis of phase III was found to be two-fold axis. The phase transition from phase II to III is of second order. These can be explained by assuming the O_{xy}-AFQ ordering in phase II [17].

(b) For $H\parallel[111]$, phase III' which is characterized by a single-k-k' ordering vector appears in an intermediate region between phase III and II [17]. However, for the other magnetic field directions, phase III'

does not appear.

(c)   When magnetic field is applied along the [110] direction, M_{AF} with $Q = [1/2,1/2,1/2]$ is induced along the [001] direction. This fact strongly suggests that O_{yz}, O_{zx} or $(O_{yz} + O_{zx})/\sqrt{2}$ type AFQ ordering is realized in phase II for $H \| [110]$ [25].

On the other hand, Takigawa *et al.* obtained the AF structure shown in Fig. 1.17 by analysing the NMR spectrum and proposed the $3-Q$ (= [1/2 0 0], [0 1/2 0], [0 0 1/2]) structure and denied the possibility of $Q=[1/2,1/2,1/2]$ proposed by Rossat-Mignod [26]. For $H \| [110]$, he found that the direction of the dipole field from Ce^{3+} ion which surround B_6 octahedra is reversal on $B^{(3+)}$ and $B^{(3-)}$ sites. This result could be explained only by the $Q=[0,0,1/2]$ ordering but not by the $Q=[1/2,1/2,1/2]$ ordering.

The discrepancy of the explanations between NMR and neutron scattering results remained as a long mystery until Sakai *et al.* resolved it in 1997, although phase II was believed to be the AFQ ordered phase.

The third stage : (1994~)

In 1997, Shiina *et al.* examined the orbital ordering of CeB_6 proposed by Ohkawa and classified the spin, orbital spin and the coupling them between spin and orbital spin proposed by Ohkawa by using the group theory [2]. The mechanism of the enhancement of T_Q by magnetic field proposed by Ohkawa is expressed as follows by using the representation of the multipole classified by Shiina *et al.*.

We consider the O_{xy} quadrupolar, T_{xyz} octupolar interaction and Zeeman term. When the order parameter in phase II is O_{xy} AFQ moment, the Hamiltonian is expressed as follows.

$$\mathcal{H} = -\sum_{i,j} K_Q O_{xy}(i) O_{xy}(j) - \sum_{i,j} K_{oct} T_{xyz}(i) T_{xyz}(j)$$

$$- \sum_i g_J \mu_B J_z(i) H \tag{1.12}$$

Here, K_Q and K_{oct} denote the magnitude of the O_{xy} AFQ and T_{xyz} AFO interactions, respectively. T_{xyz} octupole moment is expressed as

$$T_{xyz} = \frac{\sqrt{5}}{3}(J_x O_{yz} + J_y O_{zx} + J_z O_{xy}). \tag{1.13}$$

For $H \| z$, T_{xyz} is approximated as $T_{xyz} \sim J_z O_{xy}$. Then, the Hamiltonian is rewritten as follows.

$$\mathcal{H} \approx -\sum_{i,j} (K_Q + \langle J_z \rangle_{av}^2 K_{oct}) O_{xy}(i) O_{xy}(j) - \sum_i g_J \mu_B J_z(i) H \tag{1.14}$$

$$= -\sum_{i,j} K_{eff} O_{xy}(i) O_{xy}(j) - \sum_i g_J \mu_B J_z(i) H \tag{1.15}$$

$$K_Q^{eff} = K_Q + \langle J_z \rangle_{av}^2 K_{oct} \tag{1.16}$$

Here, K_Q^{eff} is the magnitude of the effective O_{xy} AFQ interaction. We consider the case where $K_5 < 0$ and $K_8 < 0$. The spin state in phase II is paramagnetic. Therefore, K_{eff} is a function of the magnetic field through the field dependence of $\langle J_z \rangle$, which increases with increasing the magnetic field until $\langle J_z \rangle$ saturates at the high field. This indicates that the magnetic field stabilizes the O_{xy} AFQ ordering. Until $\langle J_z \rangle$ saturates, T_Q continues to increase with increasing magnetic field. Once after $\langle J_z \rangle$ saturates at high fields, K_{eff} becomes constant and the closing of phase II is expected at higher field. Thus, reentrant phase diagram is obtained.

As for the reason why T_Q increases with magnetic field, another two mechanisms were proposed.

In 1984, Rossat-Mignod proposed that the following explanation for unusual increasing T_Q [17]. At zero field, the quadrupole moment is reduced by the Kondo effect, which reduce T_Q. By applying the magnetic field, the magnitude of the quadrupole moment is restored as a result of the destruction of the Kondo effect. Therefore, the increase of T_Q with magnetic field is expected.
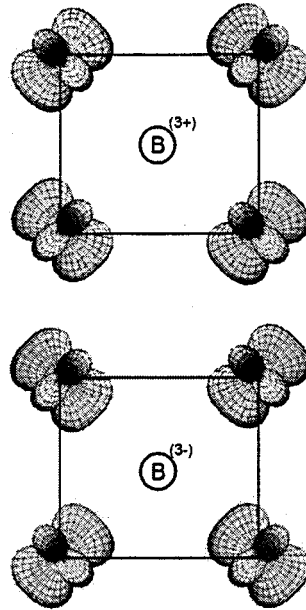
Fig. 1.18   Arrangement of the charge distribution of 4f electron in an xy plane for $H \parallel$ [110].

In 1996, Kuramoto *et al.* proposed that the fluctuation of the multipole moment plays an important role in the increase of T_Q with increasing magnetic field [32]. At zero field, T_Q is suppressed by the fluctuation of the quadrupole moment because of the existence of five components of the quadrupole moment. With increasing magnetic field, T_Q increases due to the suppression of the fluctuation of the quadrupole moment by the magnetic field.

In 1997, Sakai *et al.* solved the long-standing mystery in phase II, namely, the inconsistency of the explanations between the neutron scattering and NMR by considering the T_{xyz} AFO moment in the O_{xy} AFQ ordering phase II [33].

We assume that the order parameter in phase II is O_{xy} AFQ moment with $Q_0 = [1/2, 1/2, 1/2]$. Figure 1.18 shows the arrangement of the charge distribution of 4f electrons in an xy plane for $H \parallel$ [001]. It is noted that the charge distribution of 4f electrons around B$^{(3+)}$ is different from that around B$^{(3-)}$. By applying the magnetic field for $H \parallel$ [001], the T_{xyz} octupole moment is induced. Figure 1.18 shows the schematic picture of the induced the T_{xyz} octupole moment around B$^{(3+)}$ and B$^{(3-)}$ site. The internal field on B$^{(3+)}$ and B$^{(3-)}$ site from the magnetic moment generated by the T_{xyz} octupole moment at the Ce site is different. Thus, the ^{11}B NMR lines splits into two lines in phase II as shown in fig.1.16. Sakai *et al.* could reproduce the complicated angle dependence of the NMR spectrum by considering the the T_{xyz} octupole moment, and explained that the neutron scattering observed the AF magnetic moment but NMR mainly observed the T_{xyz} anti-ferro octupole (AFO) moment.

In 2000, Hanzawa claimed that the origin of the splitting of the NMR spectrum in phase II is the transfered hyperfine field (THF) on B sites from the surrounding Ce ions. This is clearly seen in Fig.1.18.

However, various unusual properties at low fields below T_Q remained to be explained. In 1999, Sera and Kobayashi proposed that the origin of the unusual properties at low fields below T_Q is the competition between the AF exchange and T_{xyz} AFO interactions in the O_{xy} AFQ ordered state [34]. They carried out the mean field calculation for the 4 sublattices model where three interactions of exchange, quadrupole and octupole are taken into account and could reproduce the unusual properties in phase II and III observed in the experiments.
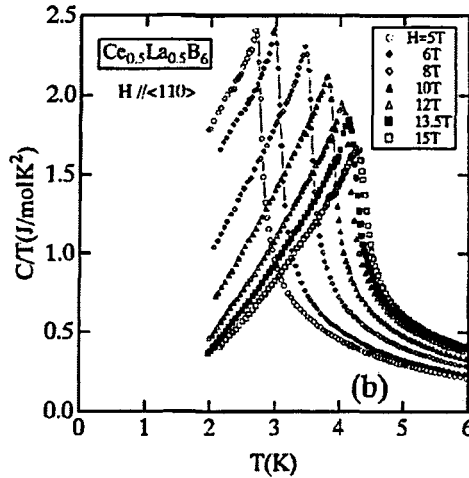
Fig. 1.19   Temperature dependence of the specific heat of $Ce_{0.5}La_{0.5}B_6$ up to 15T for $H \parallel [001]$ [30].
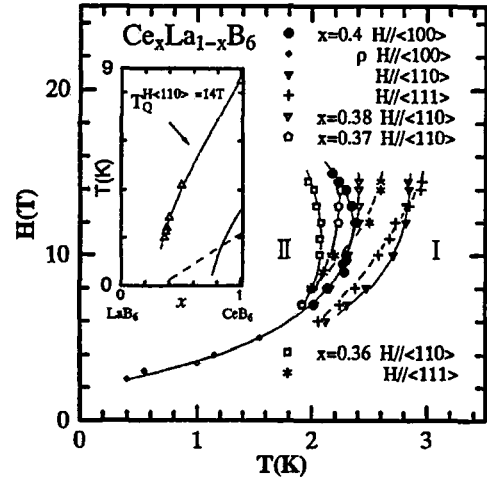
Fig. 1.20   The II-I boundary of $Ce_xLa_{1-x}B_6$ up to 15T for three field directions [31].

In addition, the temperature and magnetic field dependence of the unusual field induced AF moment expected by the mean field calculation was confirmed by the neutron scattering experiment measured by Akimitsu *et al.*. Thus, it is confirmed that the origin of the unusual properties is the competition between three interactions in the O_{xy} AFQ ordered state.

On the other hand, as for the experimental studies of CeB_6, there were big progresses. The biggest is the discovery of new phase, called phase IV, in $Ce_xLa_{1-x}B_6(x < 0.8)$. The detail of phase IV is described in 1.4. Also in CeB_6, there was a big progress in the II-I phase boundary.

In 1998, Hiroi *et al.* performed the specific heat measurements of $Ce_{0.5}La_{0.5}B_6$ under the magnetic field and found that there exists the clear peak at high magnetic fields in $Ce_{0.5}La_{0.5}B_6$ as is shown in Fig.1.19 [30]. Hiroi *et al.* also performed the specific heat measurements of $Ce_xLa_{1-x}B_6(x < 0.4)$ under the magnetic field and confirmed the tendency to close of phase II at high fields as is shown in Fig.1.19. Furthermore, they also found that the large anisotropy of the II-I phase boundary exists at high fields in $Ce_xLa_{1-x}B_6$ as is shown in Fig.1.20.

$$H_C^{II-I\langle 100 \rangle} < H_C^{II-I\langle 110 \rangle} < H_C^{II-I\langle 111 \rangle}$$
$$T_Q^{\langle 100 \rangle} < T_Q^{\langle 110 \rangle} < T_Q^{\langle 111 \rangle}$$

Here, H_C^{II-I} denotes the critical magnetic field from phase II to I.

1.3 $Ce_xR_{1-x}B_6$ (R = Pr, Nd)

RB_6 (R = Pr, Nd) also have been studied intensively since a few decades ago. These compounds show the AF magnetic order at low temperatures. The resent studies suggest that the AFQ interaction have a important role in the AF magnetic order of PrB_6 and PrB_6.

PrB_6

PrB_6 is the interesting compound where the AFQ interaction may play an important role in its non-collinear AF magnetic structure whose structure is similar to that of CeB_6. The ground multiplet of Pr^{3+} ion in PrB_6 by the spin-orbit interaction is $J = 4$ which is split into Γ_5 (triplet)-Γ_3 (314 K, doublet)-Γ_4 (377 K, triplet)-Γ_1 (464 K, singlet) due to the cubic CEF effect [36]. PrB_6 exhibits two successive first order phase transitions at low temperatures, as shown in Fig. 1.22 [45]. The magnetic structures in the commensurate (C) and IC phases

Γ_1 ——————— 464 K

Γ_4 ========= 377 K

Γ_3 ========= 314 K

Γ_6 ========= 278 K

$\Gamma_8{}^{(1)}$ ========= 135 K

Γ_5 ========= 0 $\Gamma_8{}^{(2)}$ ========= 0

PrB$_6$ NdB$_6$
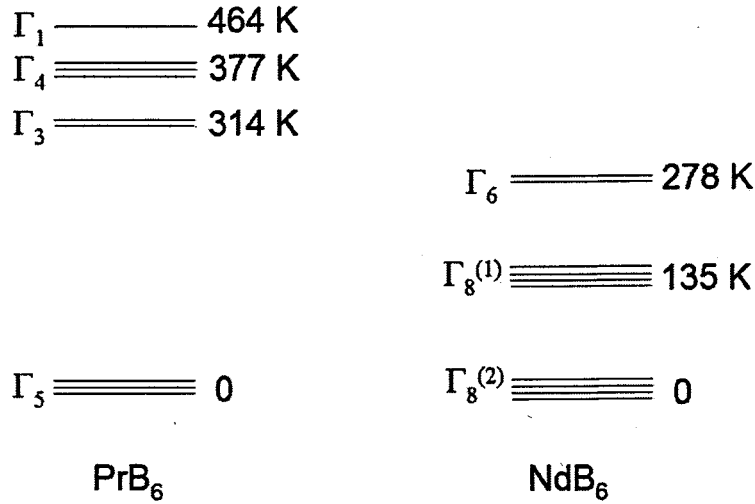
Fig. 1.21   Crystal fi eld level schemes for PrB$_6$ and NdB$_6$ determined by inelastic neutron scattering experiments [36].

at $H = 0$ and the C phase above $\sim$ 2 T for $H \parallel$ [110] determined by the neutron scattering experiment is shown in Figs. 1.23 (a)- 1.23 (c), respectively [46]. The IC double-k structure appears at $T_N = 7$ K, which is shown in Fig. 1.23 (b) and the lock-in transition to the C double-k structure appears at $T_{IC} = 4.2$ K, which is shown in Fig. 1.23 (a). Here, the double-k structure in the IC phase is characterized by the ordering vector of $k_1 = [1/4 - \delta, 1/4, 1/2]$ with $\delta = 0.05$ and that in the C phase by $k_1 = [1/4, 1/4, 1/2]$. The magnetic structures in both phases are that of the planer-type. In the C phase, the non-collinear AF magnetic structure with the two-fold easy axis similar to that in phase III of CeB$_6$ is realized. From these results, also in PrB$_6$ the O_{xy}-type AFQ interaction is believed to play an important role in the C phase and the origin of the IC magnetic structure in the IC phase is considered to be a result of the competition between the O_{xy}-type AFQ and AF exchange interactions. By applying the magnetic field along the [110] direction in the C phase, the collinear single-k AF magnetic structure is realized above $\sim$ 2 T, where the $\chi_\perp$ configuration is realized as shown in Fig. 1.23 (c).
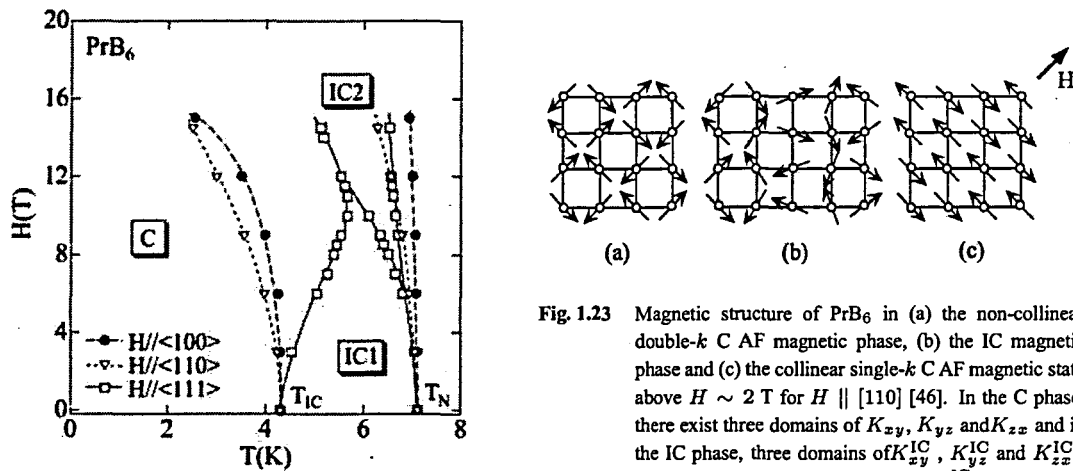
Fig. 1.22   Magnetic phase diagram of PrB$_6$ [45].

Fig. 1.23   Magnetic structure of PrB$_6$ in (a) the non-collinear double-k C AF magnetic phase, (b) the IC magnetic phase and (c) the collinear single-k C AF magnetic state above $H \sim$ 2 T for $H \parallel$ [110] [46]. In the C phase, there exist three domains of K_{xy}, K_{yz} and K_{zx} and in the IC phase, three domains of K_{xy}^{IC}, K_{yz}^{IC} and K_{zx}^{IC}. (a) and 1(b) correspond to K_{xy} and K_{xy}^{IC}, respectively.
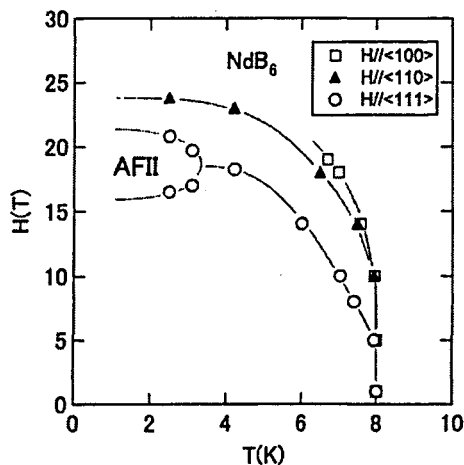
Fig. 1.24   Magnetic phase diagram of NdB$_6$ [39].
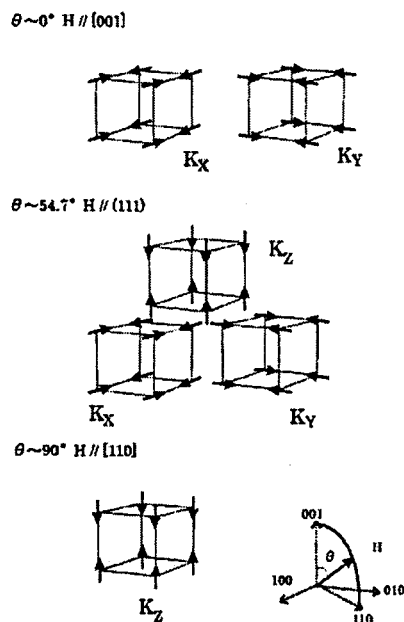
Fig. 1.25   Magnetic structure of NdB$_6$ for $H \parallel$ [001], [110] and [111] [40].

NdB$_6$

The ground multiplet of Nd^{3+} ion in NdB$_6$ by the spin-orbit interaction is $J = 9/2$ which is split into $\Gamma_8^{(2)}$ (0 K, quartet)-$\Gamma_8^{(1)}$ (135 K, quartet)-Γ_6 (278 K, doublet) due to the cubic CEF effect, as shown in Fig. 1.21 [36]. Figures 1.24 and 1.25 show the magnetic phase diagram and the magnetic structure of NdB$_6$, respectively [39,40]. NdB$_6$ exhibits the type I (Q = (0 0 1/2)) AF magnetic order with the ordered below $T_N = 8$ K [37]. The easy axis of the magnetization in the AF magnetic state is a fourfold one, although the point-charge model based on the CEF favors a threefold easy axis. The reason why the fourfold easy axis is realized in the AF magnetic state is that there exists a sizable magnitude of the O_2^0-type FQ interaction in NdB$_6$ [38].

Ce$_x$Pr$_{1-x}$B$_6$

Figures 1.26 (a) and 1.26 (b) show the magnetic phase diagram of Ce$_{0.7}$Pr$_{0.3}$B$_6$ for $H \parallel$ [001] and [110], respectively [47]. By substituting Pr into CeB$_6$, the magnetic phase diagram becomes more complex than that of Ce$_x$Nd$_{1-x}$B$_6$ system. In the present sample, six LRO phases appear : IC1, IC1′, IC2, IC2′, C and II. The magnetic phase diagram for $H \parallel$ [111] is similar to that for $H \parallel$ [110]. For $H \parallel$ [001], the results of Ce$_{0.7}$La$_{0.3}$B$_6$ are also shown. T_Q of at high magnetic fields is smaller than that of Ce$_{0.7}$Pr$_{0.3}$B$_6$, but this relation is reversed at low magnetic fields. For $H \parallel$ [001], the boundary between the IC′ and II phases is not recognized in the present experiments. The C phase exists for $H \parallel$ [110] and [111] but not for $H \parallel$ [001].

Figure 1.27 shows the Pr concentration dependence of the phase transition temperatures of Ce$_x$Pr$_{1-x}$B$_6$ [48]. With increasing x to $\sim$ 0.2, the Néel temperature, T_C decreases and disappears at $x \sim$ 0.2. For $x \leq$ 0.2, a new phase, IC2 with the IC component of its k vector oriented along a twofold axis appears in an intermediate temperature interval between T_{IC1} and T_N. Here, T_N is the transition temperature from paramagnetic phase to phase IC2. T_{IC1} and T_N show decrease with increasing x and disappear at $x \sim$ 0.7 and $x \sim$ 0.8, respectively. In the Ce-rich composition range, T_Q and T_N of CeB$_6$ decrease with decreasing x although T_N shows a increase up to $x \sim$ 0.9.
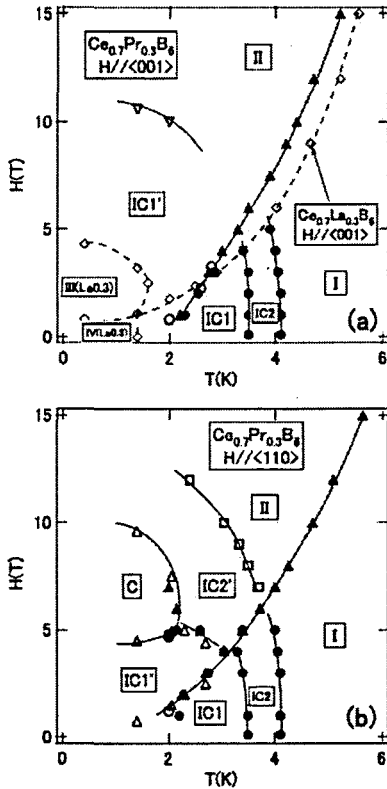
Fig. 1.26 Magnetic phase diagram of $Ce_{0.7}Pr_{0.3}B_6$ for (a) $H \parallel [001]$ and (b) [110]. For $H \parallel [001]$, the results of $Ce_{0.7}La_{0.3}B_6$ are also shown [47].
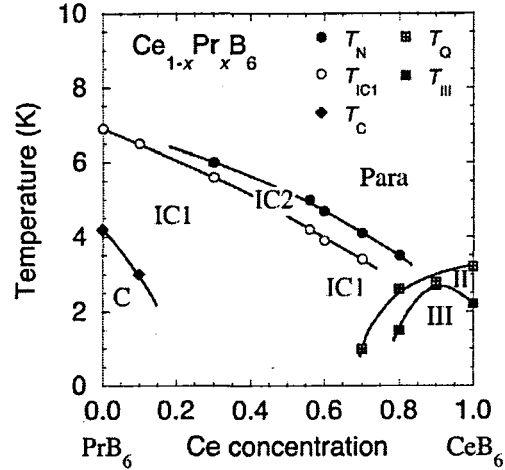
Fig. 1.27 Pr concentration dependence of the phase transition temperatures of $Ce_xPr_{1-x}B_6$ [48].

$Ce_xNd_{1-x}B_6$

Figure 1.28 shows the magnetic phase diagrams of $Ce_xNd_{1-x}B_6$ ($x = 0.9, 0.8, 0.5$ and 0.4) for for $H \parallel [001]$ [41]. The magnetic phase diagram for $x = 0.9$ is in principle the same as that of CeB_6 apart from the different values of T_Q, T_N and H_c^{III-II}. For $x = 0.8$, a marked change takes place in a low magnetic field region. A new phase, called as phase V appears on the high-temperature side of phase IIIA. Recent neutron diffraction experiments revealed that phase V for $x \geq 0.5$ is the incommensurate (IC) magnetic order and for $x \leq 0.5$, phase V changes to the type I AF magnetic order as in NdB_6 [42]. Phase IIIA is also the AF magnetic order where all types of quadrupole interaction becomes weak compared with phase III of CeB_6. With decreasing x, T_Q is rapidly suppressed down to $H \sim 3$ T. Phases IIIA and II are separated by phase V. In $Ce_{0.4}Nd_{0.6}B_6$, phase V expands markedly and phase II disappears but the phase transition between phases IIIA and V is observed at $T \sim 1.3$K at $H = 0$.

Figure 1.29 shows the x dependence of the phase transition temperatures of $Ce_xNd_{1-x}B_6$ [41]. With decreasing x down to ~ 0.88, T_Q is suppressed and T_N is enhanced. Just after T_Q coincides with T_N at $x \sim 0.88$, phase IIIA and V appear. The transition temperature from phase V to I, T_{V-I} shows a small increase down to $x \sim 0.5$ and links to the AF magnetic state of NdB_6.

The specific heat of $Ce_xNd_{1-x}B_6$ ($x = 0.03, 0.4, 0.5, 0.6$ and 0.8) is shown in the form of C/T in Fig. 1.30 [43]. C/T for $x = 0.03$ shows a sharp peak at $T_N = 7.5$ K. Its T dependence is similar to that of NdB_6. As observed on the CeB_6 side, the T dependence of C/T is similar to that of CeB_6 down to $x \sim 0.9$ but is markedly changed below $x \sim 0.8$. For $x \sim 0.8$ and 0.6, C/T shows a sharp peak at $T_{V-III} \sim 2.3$ K and a clear kink at $T_{V-I} \sim 3.1$ K. A drastic change takes place between $x = 0.5$ and 0.6. For $x = 0.5$, C/T is nearly

Fig. 1.29   Nd concentration dependence of the phase transition temperatures of $Ce_xNd_{1-x}B_6$ [41].

Fig. 1.28   Magnetic phase diagram of $Ce_xNd_{1-x}B_6$ (x = 0.9, 0.8, 0.5 and 0.4) for $H \parallel$ [001] [41].
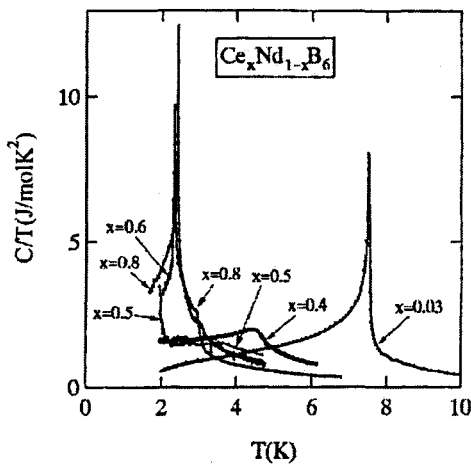
Fig. 1.30   Temperature dependence of the specific heat of $Ce_xNd_{1-x}B_6$ at $H = 0$ [43].
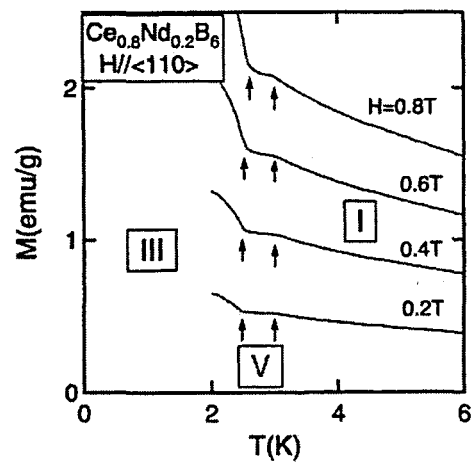
Fig. 1.31   Temperature dependence of the magnetization of $Ce_{0.8}Nd_{0.2}B_6$ for $H \parallel$ [110] [44].

constant below T_{V-I}, while a sharp peak is observed at $T_{V-III} \sim 2.0$ K. For $x = 0.4$, a broad peak is observed at T_{V-I} and C/T is nearly constant below ~ 3.0K, although a sharp peak is expected to appear at $T_{V-III} \sim 1.2$ K.

Figure 1.31 shows the T dependence of M of $Ce_{0.8}Nd_{0.2}B_6$ for $H \parallel$ [110] [44]. At $T_{V-I} = \sim 3.0$ K, a kink is observed and a T dependence is weak below T_{V-I} down to $T_{V-III} \sim 2.5$ K. The anisotropy of the magnetization is not recognized in the present sample. Below T_{V-III}, a large increase is observed already from the low magnetic fields, which suggests that the effectively weak ferromagnetic interaction exists even at low magnetic fields in phase IIIA.

1.4 Phase IV of $Ce_xLa_{1-x}B_6$

In 1995, the unusual phase diagram of $Ce_{0.5}La_{0.5}B_6$ reported by Nakamura *et al.*, where the ground state is a Kondo singlet. [49]. In 1996, Nakamura *et al.* and Sakakibara *et al.* independently discovered phase IV by the measurements of the elastic constant and the magnetization, respectively [52,53]. The existence of phase IV was confirmed by the detailed study of ρ performed by Hiroi *et al.* [54]. Figure 1.32 shows the phase diagrams of $Ce_xLa_{1-x}B_6(x = 1, 0.75, 0.7, 0.5)$ for $H \parallel [001]$ determined by the magnetization measurement [53]. By doping La in CeB_6, T_Q rapidly decreases but T_N shows a small decrease, and these two transition temperatures coincide with each other at $x = 0.8$, below which phase IV appears [51]. Figure 1.33 shows the x dependence of T_N and T_Q [50]. The T_N-x curve smoothly changes to the T_{IV-I}-x one. Here, T_{IV-I} denotes the transition temperature from phase IV to I. No anomaly is seen at $x \sim 0.8$ in the T_N-x curve or T_{IV-I}-x one. The magnetic phase diagram of $Ce_{0.5}La_{0.5}B_6$ reported by three groups is different from each other. Goto *et al.* insists that phase IV does not exist in this sample and its ground state is the Kondo singlet [49,52]. On the other hand, Sakakibara *et al.* and Sera *et al.* insist that phase IV exists in this sample [53,54].

1.4.1 Characteristics of phase IV

Since the discovery of phase IV of $Ce_xLa_{1-x}B_6$, the extensive studies have been performed by many groups. Here, we summarize the experimental results of phase IV.

Specific heat

Figure 1.34 and 1.35 show the T dependence of C of $Ce_xLa_{1-x}B_6(x=0.75, 0.7, 0.5)$ at zero magnetic field. For $x=0.75$ and 0.7, a sharp peak is observed at $T \sim 1.4K$, which originates from the IV-I transition. This sharp peak suggests that the IV-I transition is that of the second order and the magnetic entropy is mostly released due to the phase IV-I transition. For $x=0.5$, this peak becomes very broad but the maximum is still recognized at $T \sim 0.8K$. On the other hand, compared with this peak, the peak at the IV-III transition temperature in $Ce_{0.75}La_{0.25}B_6$ is very small. This indicates that the difference of the free energy between phase III and IV is extremely small.
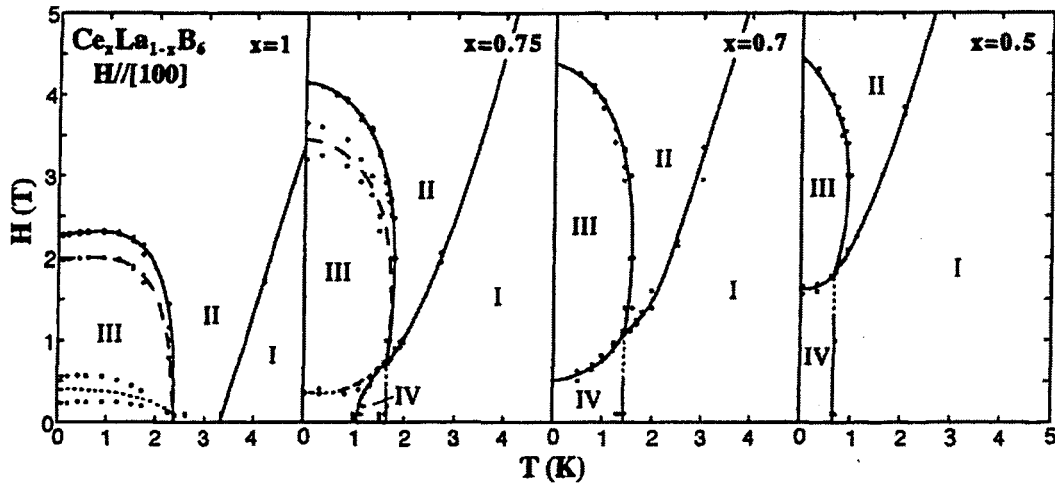
Fig. 1.32 Phase diagrams of $Ce_xLa_{1-x}B_6(x = 1, 0.75, 0.7, 0.5)$ for $H \parallel [001]$ [53].
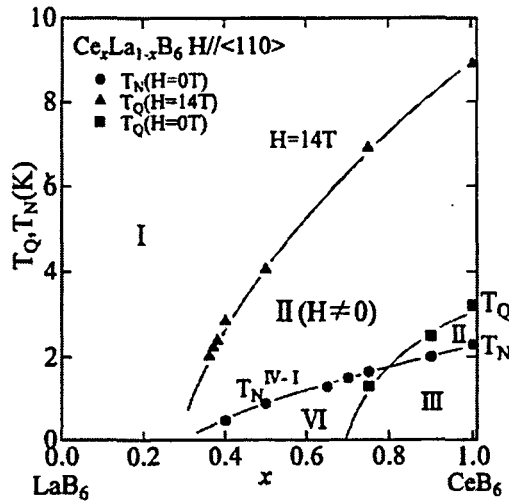
Fig. 1.33 x dependence of T_N and T_Q [50].
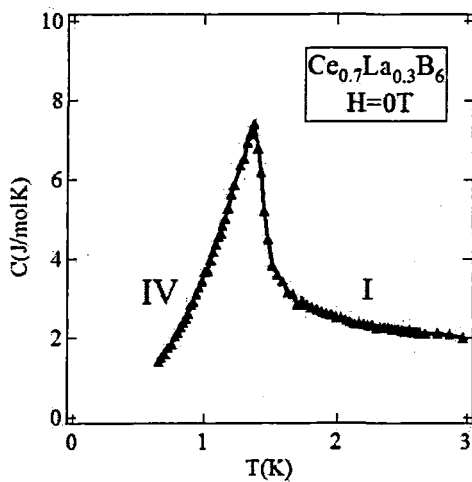
Fig. 1.34   Temperature dependence of specific heat of $Ce_{0.7}La_{0.3}B_6$ at zero field.
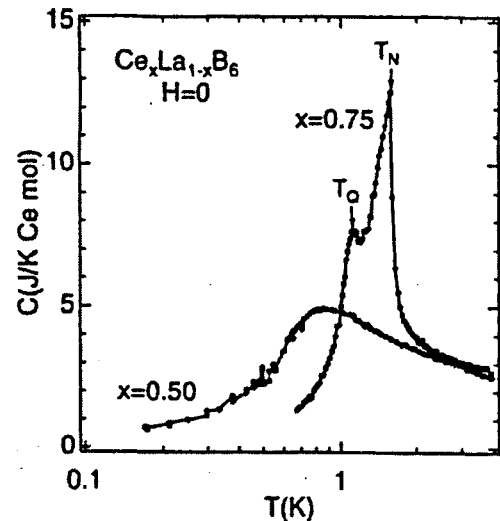
Fig. 1.35   Temperature dependence of specific heat of $Ce_x La_{1-x} B_6$ ($x=0.75$, 0.5) at zero field [52].

Magnetic susceptibility

Figure 1.36 shows the T dependence of the magnetic susceptibility of $Ce_x La_{1-x} B_6$ ($x=1.0$, 0.75, 0.7, 0.5) [53]. The magnetic susceptibility shows the broad peak at T_{IV-I}. Since the hysteresis could not be observed, the phase transition from IV to III is that of the second order. This result is consistent with that of the specific heat. It is noted that the magnetic susceptibility in phase IV is different from that in the usual AF magnetic phase. Namely, the cusp at T_{IV-I} is observed independent of the magnetic field direction, and no appreciable anisotropy is found below T_{IV-I}. Entering into phase III from phase IV with decreasing temperature, the magnetic susceptibility shows a large increase with decreasing temperature. This originates from the FM component easily induced by the magnetic field in phase III. The IV-III phase transition is that of the first order.

The magnetization measurements of $Ce_{0.75}La_{0.25}B_6$ under uniaxial pressures were performed by Sakakibara et al.. The results show that there exists the anisotropy of M in phase IV under the uniaxial pressures as shown
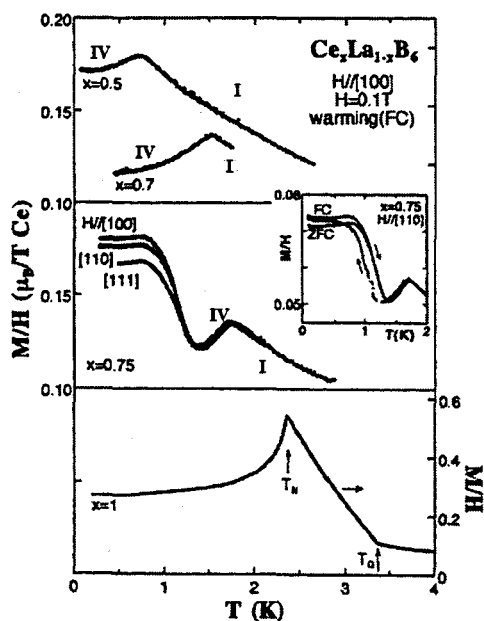
Fig. 1.36   Temperature dependence of the magnetic susceptibility of $Ce_xLa_{1-x}B_6$ (x=1.0, 0.75, 0.7, 0.5) [53].
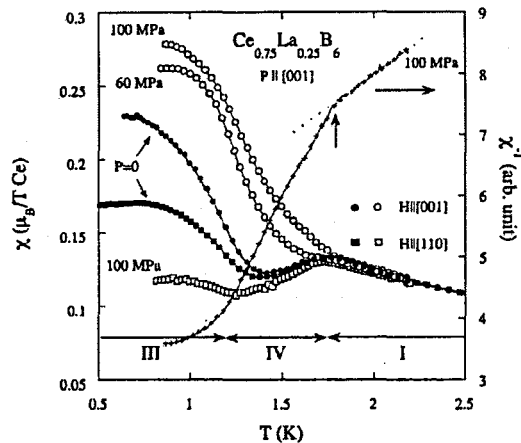
Fig. 1.37   Temperature dependence of the magnetic susceptibility of $Ce_{0.75}La_{0.25}B_6$ for $P \parallel [001]$ [56].
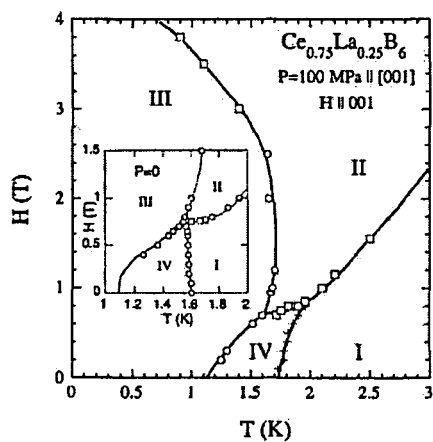
Fig. 1.38   Magnetic phase diagram of $Ce_{0.75}La_{0.25}B_6$ for $P \parallel [001]$ and $H \parallel [001]$ [56].
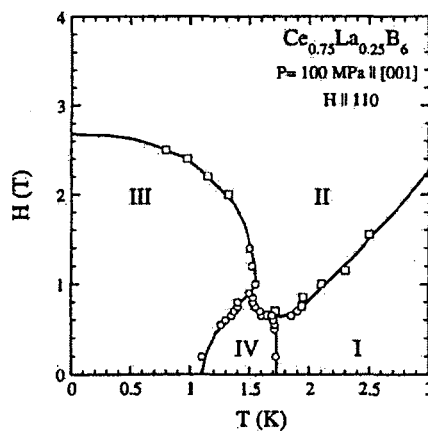
Fig. 1.39   Magnetic phase diagram of $Ce_{0.75}La_{0.25}B_6$ for $P \parallel [001]$ and $H \parallel [110]$ [56].

in Fig.1.37 [56].

Magnetoresistance

Figure 1.40 shows the magnetic field dependence of ρ of $Ce_{0.7}La_{0.3}B_6$ for $H \parallel [001]$ [55]. ρ exhibits the small magnetic field dependence in phase IV. The small magnetoresistance is observed also in phase IV of $Ce_{0.75}La_{0.25}B_6$ and $Ce_{0.65}La_{0.35}B_6$. This small magnetoresistance is common to phase IV [54], and means the small magnetic field dependence of the energy levels in phase IV.
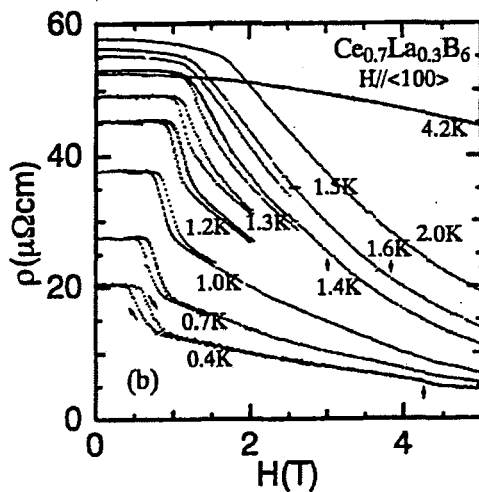
Fig. 1.40 Magnetic fi eld dependence of the electrical resistivity, ρ of $Ce_{0.7}La_{0.3}B_6$ for $H \parallel$ [001] [55].
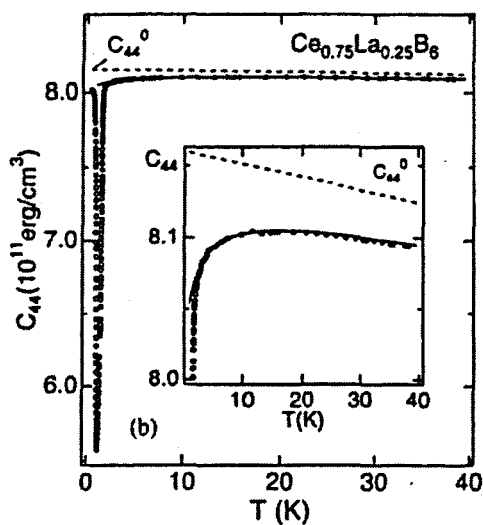
Fig. 1.41 Temperature dependence of the elastic constant, C_{44} mode of $Ce_{0.75}La_{0.25}B_6$ [52]
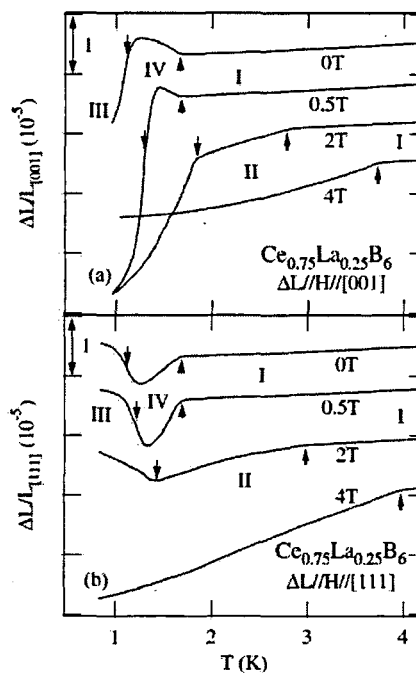
Fig. 1.42 Thermal expansion along the [001] and [111] direction of $Ce_{0.75}La_{0.25}B_6$ [57].

Elastic constant

Figure 1.41 shows the T dependence of the elastic constant, C_{44} mode of $Ce_{0.75}La_{0.25}B_6$ [52]. The elastic constant of C_{44} mode exhibits the anomalous large softening in phase IV. In the case of ferro-quadrupole (FQ) ordered state, the observation of the large softening towards the transition temperature. However, in the present case, the remarkable softening is observed below T_{IV-I}.

Thermal expansion

Figure 1.42 shows the thermal expansion along the [001] and [111] direction of $Ce_{0.75}La_{0.25}B_6$ [57]. In phase IV, the lattice expands along the [001] axis, while shrinks along the [111] axis. From these results, Akatsu et al. concluded that the trigonal lattice distortion takes place in phase IV and discussed the possibility of the $O_{xy} + O_{yz} + O_{zx}$ order in phase IV. However, they did not take the domain distribution into account. In the microscopic measurement, it is difficult to know how the crystal structure is changed in the ordered state. In order to determine the crystal structure, it is necessary to measure the transverse and longitudinal length changes under the condition that the single domain state is verified to be realized.

Neutron diffraction • NMR • μSR

Since the discovery of phase IV of $Ce_{0.75}La_{0.25}B_6$, large efforts have been paid to find the magnetic peak. However, no magnetic reflection was observed in phase IV [58]. On the other hand, a trace of a broken time-reversal symmetry was observed in NMR and μSR experiments [59,60].

Soon after the discovery of the LRO with Q=(1/2 1/2 1/2) by the resonant X-ray scattering measurement (described later), Kuwahara et al. performed the neutron scattering experiment of $Ce_{0.7}La_{0.3}B_6$ and observed weak but distinct superlattice reflection at the scattering vector $k = (h/2, h/2, l/2)$ (h, l = odd number) [61]. Figure 1.43 shows the magnetic form factor at the superlattice spots along the [1,1,1] and [1,1,$\bar{1}$] directions obtained by using the integrated intensity of the observed superlattice reflections and by making the corrections. The magnetic form factor is strong for high scattering vectors. This cannot be explained by the usual antiferromagnetic ordering even by considering any conceivable magnetic structure as well as any domain distribution because the data in Fig. 1.43 are the form factors at the superlattice spots along the same direction. Therefore, this unusual k dependence of the form factor directly evidences that the order parameter has a magnetization density different from ordinary dipole orderings. This result qualitatively agrees with the theoretical calculation considering an average of four domains of the order parameter T_β, as shown in Fig. 1.44 [62]. Furthermore, from the selection rule of the cross section based on the symmetry classification of octupolar scattering for the three possible octupoles T_{xyz}, T_α and T_β, this result can rule out the possibility of T_{xyz} with Γ_2 symmetry because the superlattice reflections along the [1,1,1] direction with threefold symmetry have been observed. T_α with Γ_4 symmetry is also unlikely to explain the observed k dependence because magnetic dipoles with the same Γ_4 symmetry as T_α are expected to be mixed. Therefore, this result strongly indicates that the order
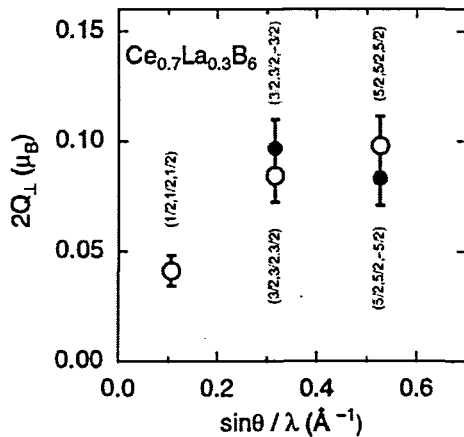
Fig. 1.43 Magnetic form factor at the superlattice spots along the [1,1,1] (open circles) and [1,1,$\bar{1}$] (filled circles) directions in phase IV of $Ce_{0.7}La_{0.3}B_6$ [61].
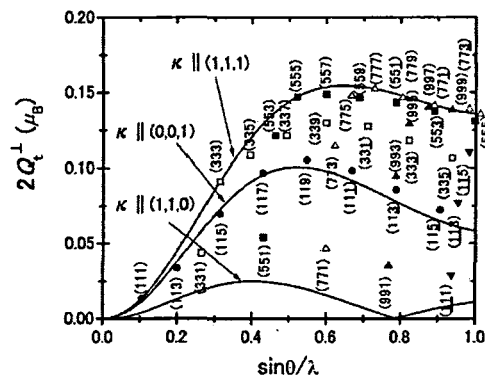
Fig. 1.44 Calculate result of the domain-averaged magnetic form factor as a function of the magnitude of the momentum transfer, $\sin\theta/\lambda$ under the assumption that the order parameter is $T_\beta = (T_x^\beta + T_y^\beta + T_z^\beta)/\sqrt{3}$ [62].
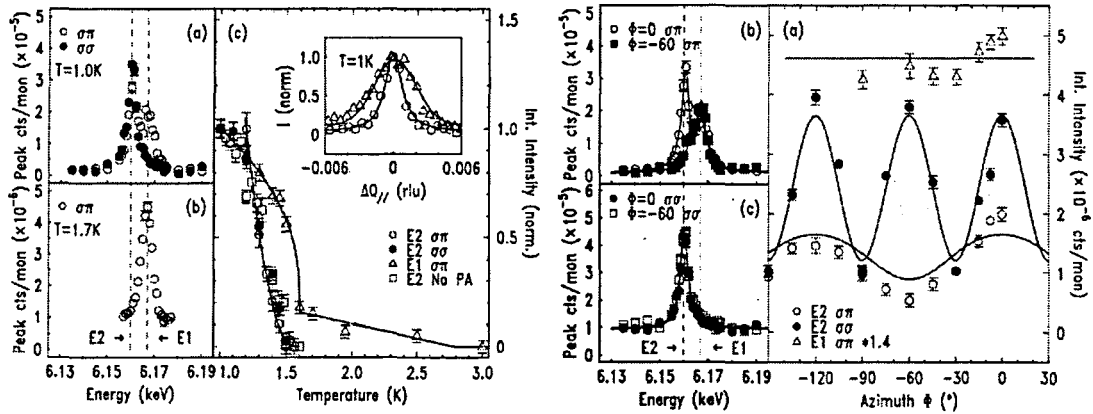
Fig. 1.45   Experimental results of RXS for $Ce_{0.7}La_{0.3}B_6$ at the Ce L_2 absorption edge. The scattering vector Q is (3/2 3/2 3/2) [63].

parameter of phase IV is the magnetic octupoles T_β with Γ_5 symmetry.

Resonant X-ray scattering

Recently, the resonant X-ray scattering (RXS) measurement of $Ce_{0.7}La_{0.3}B_6$ was performed by Mannix et al. [63]. The results show that a long-range order (LRO) with Q=(1/2 1/2 1/2) exists in phase IV. Figure 1.45 shows the experimental results of RXS for $Ce_{0.7}La_{0.3}B_6$ at the Ce L_2 absorption edge. The scattering vector Q is (3/2 3/2 3/2). For the σ-π' intensities, both E1 and E2 RXS peak is observed at T=1.0K. On the other hand, for the π-π' intensities, only the E2 RXS peak exists. At T=1.7K, only the E1 RXS peak is observed for the σ-π' intensities. These results indicate that the magnetic dipole moment is induced in 5d shell but the quadrupole moment is not. At the E2 resonance, rank-i (i=1, 2, 3, 4) tensors of the 4f orbital contribute to σ-π' and π-π' polarizations. However, the result of the E1 transition denies the existence of rank-2 and rank-4 tensors. Thus, the following two cases are considered as the order parameter corresponding to the E2 RXS peaks. One is both the magnetic dipole moment and the octupole moment, and the other is either one of the two.

Mannix et al. explained the azimuth angle dependence of integrated intensities by assuming that Γ_{4u}-AFO ordering is realized in phase IV as is shown in Fig.1.45. If the order parameter of phase IV is the Γ_{4u}-AFO, the Γ_{4u} magnetic dipole moment must be induced. This assumption contradicts the experimental results of the neutron diffraction.

1.4.2 Γ_{5u} Antiferro-octupole (T_β-AFO) ordering model

In 2001, Kusunose and Kuramoto discussed the possibility of the Γ_5-AFO ordering in phase IV in the course of the study of phase III' in CeB_6 for $H \parallel$ [111] [64]. Because the easy axis of Γ_{5u}-AFO ordered state is the [111] direction, the order parameter of phase IV is probably $T_\beta = (T_\beta^x + T_\beta^y + T_\beta^z)/\sqrt{3}$ with four equivalent domains. It is noted that T_β accompanies a ferro-quadrupolar moment of the $O_{xy}+O_{yz}+O_{zx}$. Thus, $O_{xy}+O_{yz}+O_{zx}$ is induced by T_β-AFO ordering and then the lattice deforms along the [111] axis.

In 2003, Kubo and Kuramoto performed the mean field analysis for phase IV in detail [65].

Figure 1.46 shows the level scheme of the Γ_8 quartet when the T_β-AFO interaction exists. The Γ_8 quartet splits into three levels and the ground state becomes a nonmagnetic singlet. Figure 1.47 shows the temperature dependence of the quadrupole susceptibility, χ_{Γ_5}. χ_{Γ_5} rapidly increases at the transition temperature. This means that the elastic constant C_{44} shows a remarkable softening at the transition temperature. Figure 1.48 shows the temperature dependence of the magnetization in the single domain in magnetic field $H = 0.2$ T
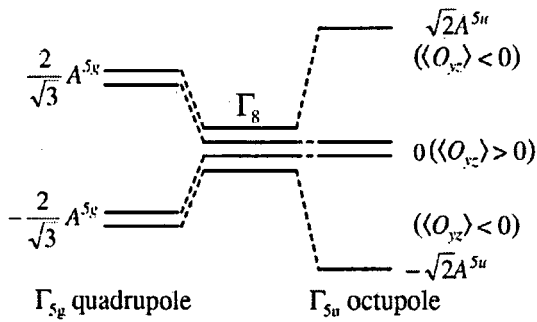
Fig. 1.46 The level scheme of the Γ_8 quartet in the T_β-AFO interaction (right) and in the O_{xy}-AFQ interaction [65].
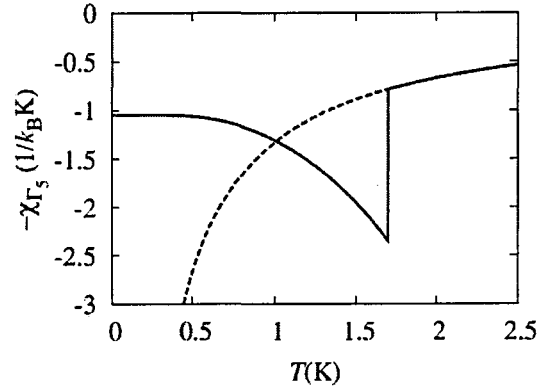
Fig. 1.47 Calculated results of the temperature dependence of the quadrupole susceptibility, χ_{Γ_5} [65].
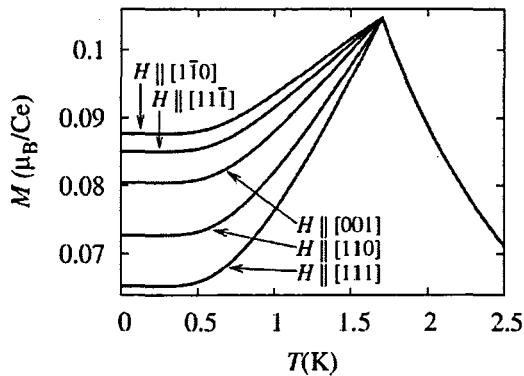
Fig. 1.48 Calculated results of the temperature dependence of the magnetization in the single domain in magnetic field $H = 0.2T$ along various directions [65].
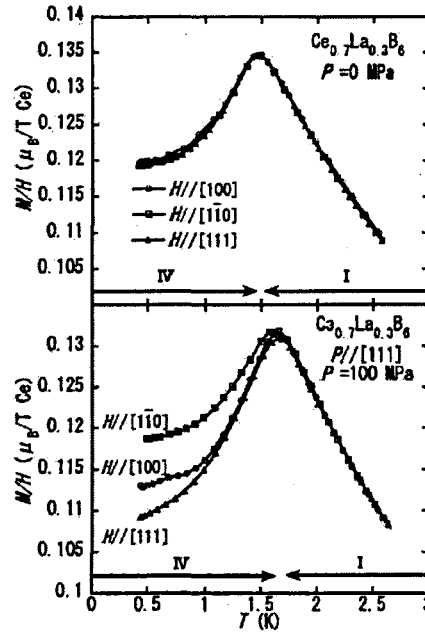
Fig. 1.49 Temperature dependence of the magnetization of $Ce_{0.7}La_{0.3}B_6$ under uniaxial pressures applied along the [111] direction in magnetic field $H = 0.5T$ along three directions [66].

along various directions. This results shows that the magnetization is anisotropic in T_β-AFO ordered state. This anisotropic behavior is confirmed by the the magnetization measurement of $Ce_{0.7}La_{0.3}B_6$ under uniaxial pressures applied along the [111] direction as in shown in Fig.1.49 [66].

Soon after the discovery of the LRO in phase IV by the resonant X-ray diffraction, Kusunose and Kuramoto analyzed the azimuth angle dependence of RXS performed by Mannix et al. [63] by assuming that T_β-AFO ordering is realized in phase IV as is shown in Fig.1.50 [67]. In the E2σ-σ' resonance, the scattering intensity exhibits sixfold oscillation, which indicates the occurrence of the order with sixfold symmetry along [111]. Among all the multipoles in the Γ_8 quartet, Γ_{2u}, Γ_{4u}, Γ_{5u} and Γ_{4g} type multipoles have sixfold symmetry. Table 1.2 shows the angle dependence of the RXS intensity for possible multipoles in threefold axis. The experimental results for the E2σ-σ' channel shows the maximum at $\Psi = 0$. This experimental results can be
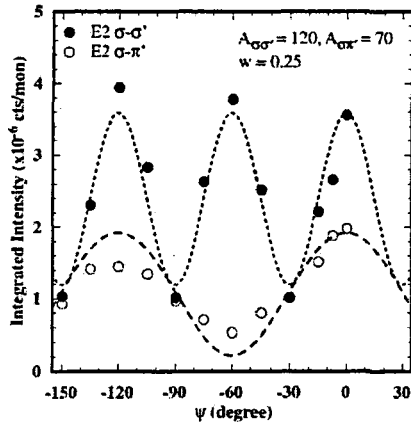
Fig. 1.50 The azimuthal angle dependence of $Ce_{0.7}La_{0.3}B_6$. The symbols are taken from Mannix *et al.*. The dotted and the dashed lines show the intensities from the Γ_{5u}-type octupole order [67].

$p-\Gamma_n$	E2 $\sigma-\sigma'$	E2 $\sigma-\pi'$
1-4u	0	$\frac{1}{40}\sin^2 3\theta$
2-5g	$\frac{1}{224}(3+\cos 2\theta)^2$	0
3-2u	$\frac{1}{36}\sin^2(2\theta)\sin^2(3\Psi)$	$\frac{1}{144}(3\cos 2\theta-1)^2\cos^2\theta$ $\times(\frac{1}{\sqrt{2}}\tan\theta-\cos 3\Psi)^2$
3-4u	$\frac{1}{36}\sin^2(2\theta)\sin^2(3\Psi)$	$\frac{1}{144}(3\cos 2\theta-1)^2\cos^2\theta$ $\times(\frac{1}{\sqrt{2}}\tan\theta+\cos 3\Psi)^2$
3-5u	$\frac{1}{16}\sin^2(2\theta)\cos^2(3\Psi)$	$\frac{1}{256}(\cos\theta+3\cos 3\theta)^2$ $\times\sin^2 3\Psi$
4-4g	0	$\frac{1}{16}\cos^6\theta\cos^2 3\Psi$
4-5g	$\frac{1}{1512}(5-3\cos 2\theta)^2$	$\frac{1}{1296}\cos^6\theta\cos^2 3\Psi$

Table. 1.2 The angle dependence of the RXS intensity for possible multipoles in threefold axis [67]..

explained by only the Γ_{5u}-type AF octupole ordering whose angle dependence is proportional to $\cos^2 3\Psi$.

On the other hand, the experimental results for the E2σ-π' channel exhibits threefold symmetry. The Γ_{5u}-type octupole, which is consistent with the observed oscillation for the E2σ-σ' channel, cannot explain this experimental results. This problem is solved by considering the existence of the four equivalent domains. In the E2σ-π' channel, the contribution from [111] domain parallel to Q=(3/2,3/2,3/2) is much larger than those from the other three domains. In contrast, the contributions from the other three domains are much larger than that from [111] domain in the E2σ-σ' channel. By considering the above situation, Kusunose and Kuramoto obtain the theoretical lines as shown in Fig.1.50, which could reproduce the experimental results very well.

As mentioned above, T_β-AFO ordering proposed by Kuramoto *et al.* could explain most of the characteristic properties in phase IV. Thus, the T_β-AFO ordering is said to be a strong candidate for the LRO in phase IV.

1.4.3 Problems in the T_β-AFO ordering model proposed by Kuramoto *et al.*

Although the T_β-AFO order is the most plausible candidate for the order in phase IV, there exists the following problems which seem to be difficult to be explained by the T_β-AFO ordering.

(1) The experimental results of the magnetization under uniaxial pressures $P \parallel [001]$

There exists four equivalent domains along [111] direction in phase IV. Then, this domain distribution is not affected by the uniaxial pressure for $P \parallel [001]$. However, the experimental results of the magnetization under uniaxial pressures $P \parallel [001]$ shows the large anisotropic behavior in magnetic field as shown in Fig.1.37. Thus, the T_β-AFO ordering is difficult to explain these experimental results.

(2) Ce concentration (x) dependence of T_N and T_{IV-I}

It is noted that T_N above x=0.8 is smoothly connected with T_{IV-I} below x=0.8 as shown in Fig.1.33. This continuity could be explained if the magnetic order is realized in phase IV. However, it seems to be difficult by assuming the T_β-AFO ordering.

(3) Competition between the induced O_{xy}-type FQ ordering accompanied with the T_β-AFO ordering and the O_{xy}-type AFQ interaction

The T_β-AFO ordering induces the O_{xy}-type FQ ordering which explains the lattice distortion along [111] di-

rection. On the other hand, there should exist the O_{xy}-AFQ interaction in $Ce_xLa_{1-x}B_6$ system. If the phase IV is the T_β-AFO ordering, the induced O_{xy}-type FQ ordering should compete with the O_{xy}-AFQ interaction. Kuramoto et al. did not take this competition into account because they considered only the T_β-AFO interaction. Thus, it is necessary to examine how the pure T_β-AFO ordering is affected by the other interactions such as O_{xy}-AFQ, T_{xyz}-AFO and AF exchange interactions and if the physical properties of $Ce_xLa_{1-x}B_6$ could be explained or not by taking these different types of the interaction into account.

(4) Temperature dependence of the E1 intensity

Kuramoto et al. assumes the T_β-AFO ordering in phase IV, and reproduces the experimental results of the RXS in $Ce_{0.7}La_{0.3}B_6$. However, Matsumura pointed out that as for the temperature dependence of the E1 intensity, there exists some unexplained problems. [68] As in shown in Fig. 1.45, the E1 intensity decreases only gradually with increasing temperature, with a discontinuity at T_{IV-I}, and continues up to $T \sim 3$ K, while the E2 intensity disappears at T_{IV-I}. Assuming the T_β-AFO ordering in phase IV, the E1 intensity seems to corresponds to the induced electrical dipole moment by the octupole ordering at T_{IV-I}. In contrast, the reason for the existence of the E1 intensity above T_{IV-I} and the sharp rising of this intensity just above T_{IV-I} is not known. Moreover, it is noted that the width of the longitudinal scans taken at E2 and E1 energy thresholds at $T=1.0$ K, given in inset of Fig. 1.45, are considerably different. The E2 is consistent with the LRO, while the E1 is broad, indicating that the correlation length is $200 \sim 300$Å.

In the manner now described, there exists several problems with the T_β-AFO ordering. Thus, the order parameter of phase IV is still controversial and further studies are necessary to clarify its nature.

Chapter 2

Purpose of the Present Study

Since the discovery of phase IV in $Ce_xLa_{1-x}B_6$, many physicists have tried to solve the mysterious order in phase IV. Recently, the T_β-AFO ordering proposed by Kuramoto *et al.* is said to be a strong candidate for LRO in phase IV. However, there exists several problems which seem to be difficult to be explained by their model. Thus, we consider that the order parameter in phase IV has not yet been clarified.

In $Ce_{0.7}La_{0.3}B_6$, whose ground state is phase IV, there exists at least three kinds of interactions, *i.e.*, the AF exchange, O_{xy}-AFQ and T_{xyz}-AFO interactions with nearly the same magnitude except the interaction forming phase IV. It is expected that the phase IV is affected if the unbalance in these interactions is introduced. It is possible to get the information on phase IV by introducing the unbalance.

Under these situations, we set up the following two purposes. One is the experimental study and another is the mean field calculation.

(1) The rare-earth (R) magnetic ion doping effect on phase IV.

In $Ce_xLa_{1-x}B_6$, the ratio of the magnitude of the different kinds of interactions is varied with x. Around $x = 0.75$ where phase IV just appears, the magnitude of the four kinds of the interactions are nearly the same. When the R ion is doped in this compound, the existence of the magnetic moment of R ion should affect the four kinds of the interactions. Then, we expect the appearance of the new kind of the phenomena, even the new kind of the ordered phase. In sample with a small x, say, $x \leq 0.5$, the balance of the interactions are broken already in $Ce_xLa_{1-x}B_6$. The interaction forming phase IV is the strongest at low magnetic field. In such a situation, the magnetic moment of R ion is easy to affect phase IV but difficult to affect phase III. Thus, The R ion doping effect is expected to be different depending on the x value. We have studied $Ce_xR_yLa_{1-x-y}B_6$ ($x = 0.7, 0.65, 0.6, 0.5$ and 0.4) with $R = $ Pr and Nd.

(2) Mean-field calculation for phase IV in the model where the O_{xy}-AFQ, T_{xyz}-AFO and AF exchange interactions in addition to the T_β-AFO interaction.

We note that the LRO was discovered in the resonant X-ray diffraction and Kuramoto *et al.* proposed the T_β-AFO ordering model when the author was a master course student. At that time, the author had been studied the R ion doping effect on phase IV without knowing the order parameter in phase IV. Although the T_β-AFO ordering model could explain many characteristic properties in phase IV, we found that in the Kuramoto's model, only the T_β-AFO interaction was taken into account. Then, we set up the above mentioned mean field calculation as the purpose of the study.

Chapter 3

Experimental

3.1 Preparation of the single crystals

In the present study, we made the following single crystals.

- $Ce_{0.7}Nd_yLa_{0.3-y}B_6$ (y =0.005, 0.01, 0.03, 0.05 and 0.1)
- $Ce_{0.65}Nd_yLa_{0.35-y}B_6$ (y = 0.02, 0.03 and 0.05)
- $Ce_{0.6}Nd_yLa_{0.4-y}B_6$ (y = 0.05, 0.06, 0.07, 0.08 and 0.1)
- $Ce_{0.5}Nd_{0.1}La_{0.4}B_6$
- $Ce_{0.5}Pr_{0.1}La_{0.4}B_6$
- $Ce_{0.4}Nd_{0.1}La_{0.5}B_6$

In the following sections, we describe the details of the sample preparation.

3.1.1 Preparation of the sintered sample

In order to make big and high quality single crystals, it is necessary to make homogeneous sintered samples with high density. The procedure to make a sintered sample is as follows.

1. Measure the appropriate weight of powder of B and rare earth oxide according to the formula described below. The formula indicates the reaction leading to RB_6 powdered sample. The powder of rare earth oxide used in the present study is shown in table 3.1. Take $Ce_{0.7}La_{0.29}Nd_{0.01}B_6$ for example, the the reaction equation is given by

   - $CeO_2 + 8B \longrightarrow CeB_6 + 2BO \uparrow$
   - $La_2O_3 + 15B \longrightarrow 2LaB_6 + 3BO \uparrow$
   - $Nd_2O_3 15B \longrightarrow 2NdB_6 + 3BO \uparrow$
   - $0.7\,CeB_6 + 0.29\,LaB_6 + 0.01\,NdB_6 \longrightarrow Ce_{0.7}La_{0.29}Nd_{0.01}B_6$.

   Before measuring the weight of La_2O_3 powder, it is heated for 15 $\sim$ 18h at 300 °C in order to remove moisture from La_2O_3 powder. The weight of these powder is arranged such that the total weight is $\sim$ 20 g.

2. Mix the different kinds of powder using an auto mixing machine for 30 minutes.

3. Put the mixed powder into the long and thin rubber tube and close both ends of the tube.

4. Press the powder using the Cold Isostatic Press (CIP) produced by the Nikkiso incorporated company, as shown in Fig. 3.1. Then a uniform pressure is added to the powder at 250 MPa for 1 minutes.

5. Sinter the pressed powder using the high frequency furnace, as shown in Fig.3.2. The temperature for a reaction is about 1800 °C and the time for the reaction is 1 hour.

material	purity(%)	manufacturer
CeO_2	99.99	Rare metallic Inc.
La_2O_3	99.99	Rare metallic Inc.
Nd_2O_3	99.99	Rare metallic Inc.
Pr_6O_{11}	99.99	Rare metallic Inc.
B	99	High purity science research institute Inc.

Table. 3.1   Rare earth oxide powder used in the present study.

3.1.2   Preparation of the single crystal : Floating Zone (FZ) method

$Ce_xR_yLa_{1-x-y}B_6$ single crystals used in the present study were prepared by the FZ method as follows.

1. Hang the sintered sample with a length of ~ 100 mm down and set short one with that of ~ 30 mm at the lower shaft.

2. Move an each edge of the two sintered samples to the focus point of furnace and then the both edge are

Fig. 3.1   CIP we used in the present work.
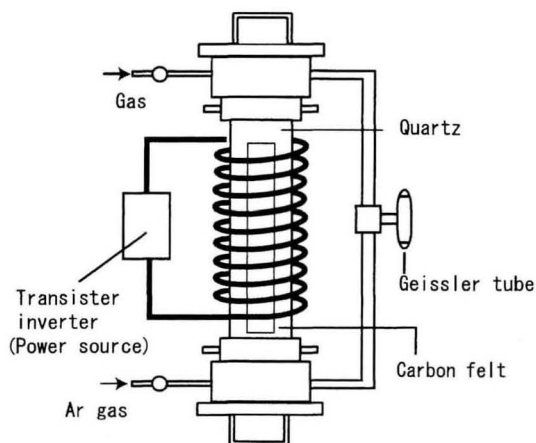
Fig. 3.2   Schematic picture of the High frequency furnace.
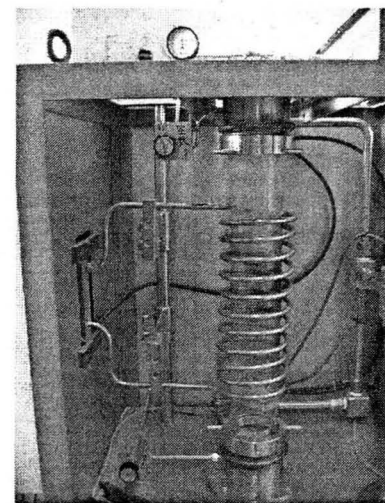
Fig. 3.3   High frequency furnace we used in the present work.
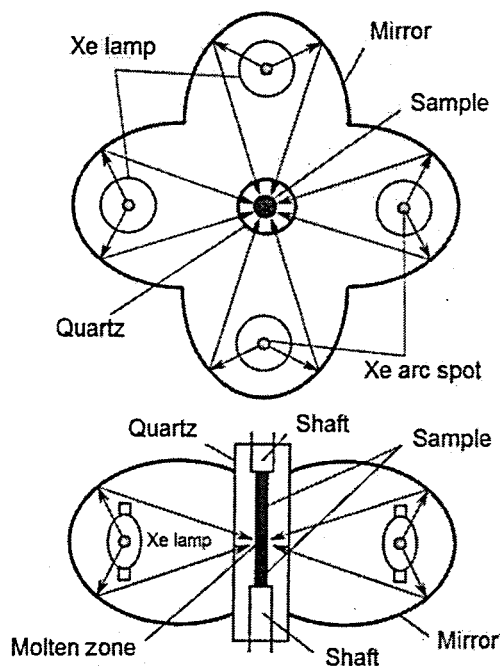
Fig. 3.4 Schematic picture of the four-mirror-type image furnace.
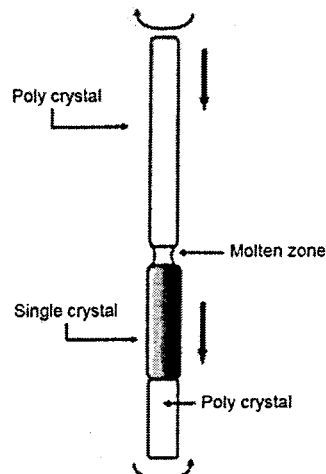
Fig. 3.5 Schematic picture of the Floating Zone method.

melted and a melting zone with a length of ~ 5 mm.

3. The single crystal is made by moving the melting zone with ~ 10 mm/h. Then the upper and lower sintered samples are rotated in a reversal direction.

When the sintered sample is entered into molten zone, the part of the sintered sample in a molten zone is melted. The melting zone is moved from the bottom to the top of the sintered sample slowly with ~ 10 mm/h. In a part of the melted part which is cooled down, a single crystal is produced along same crystal axis. This part of a single crystal is enlarged during the movement of the melting zone. In a FZ method, the sample does not touch with any other materials, which makes the sample quality very good. As mentioned feature above, the high purity and large single crystal can be produced by the FZ method. Figure 3.4 shows the schematic picture of the situation of the single crystal growth by the FZ method. In present study, image furnace with four xenon lamps produced by the Crystal Systems incorporated company was used as a single crystal growth furnace. The crystal growth was performed by Associate Prof. F. Iga.

3.1.3 Sample check by X-ray Laue method

1. Cut only homogeneous parts of the single crystal using a diamond cutter.
2. Fix the sample on the goniometer and the X-ray is exposed to the cut surface of a single crystal for a few minutes. Then, Laue picture is obtained.
3. Determinate the (001) and (110) surface using a Laue picture as reference.
4. Cut the sample using the electrical discharge machine so as to get the crystal surface we want.

3.2 ^{3}He cryostat

We used a ^{3}He cryostat made by A. Kondo for the electrical resistivity measurement below 1.4K. The ^{3}He cryostat is a devise by which the low temperature down to 0.4 K is obtained by pumping liquid ^{3}He [69]. ^{3}He is
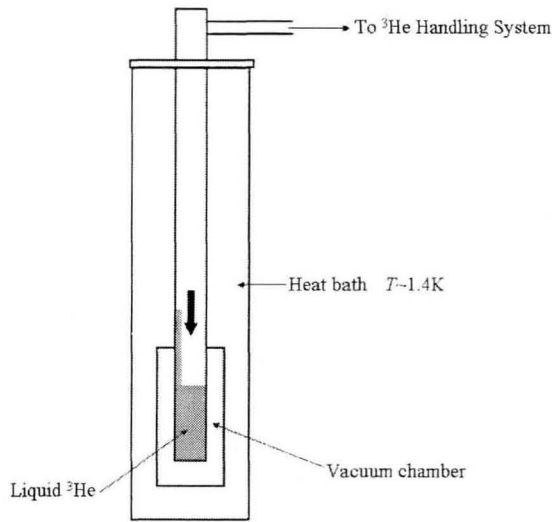
Fig. 3.6   Schematic picture of the ^{3}He insert dewier [69].
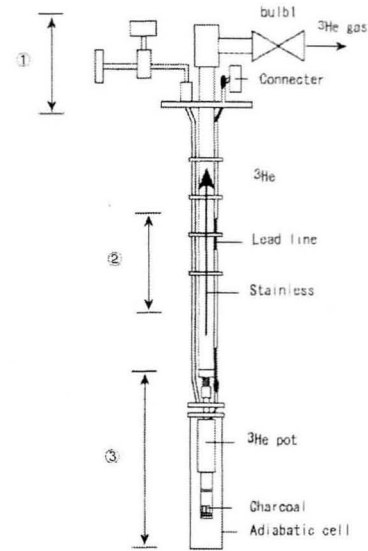
Fig. 3.7   Schematic picture of the ^{3}He cryostat using the electrical resistivity measurement.
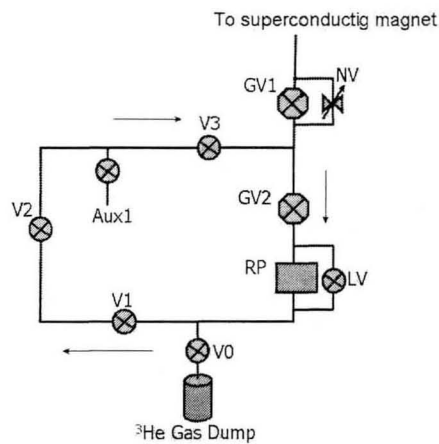
Fig. 3.8   Schematic picture of single shot type ^{3}He handling system. V, GV, NV and LV mean the valve, the gate valve, the needle valve and the leak valve, respectively.
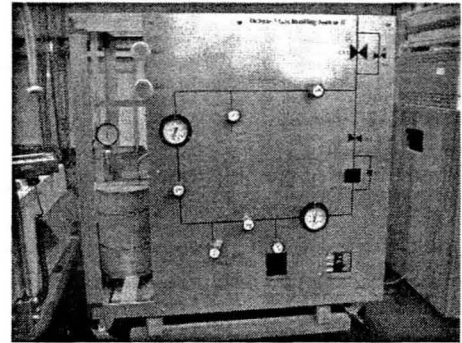
Fig. 3.9   Handmade ^{3}He handling system.

a Fermi particle composed of a neutron and two protons. Because ^{3}He has a 100 times saturated vapor pressure of ^{4}He, ^{3}He cryostat can produce lower temperature than ^{4}He one.

The principle to lower the temperature by using ^{3}He cryostat is as follows.

Figure 3.6 shows the schematic picture of the ^{3}He insert Dewar. First, the external world of the ^{3}He insert Dewar is cooled down to 1.4 K by pumping liquid ^{4}He. Next, ^{3}He gas is entered into ^{3}He pot, and then ^{3}He gas is liquefied by the thermal contact. In order to prevent the thermal contact from the external world, there exists the vacuum chamber around the ^{3}He pot. After ^{3}He becomes liquid, the liquid ^{3}He is pumped by the rotary vacuum pump, and then the temperature is cooled down to 0.4 K. The ^{3}He cryostat using the electrical resistivity measurement is schematically shown in Fig.3.7.

Figure 3.8 shows the schematic picture of single shot type ^{3}He handling system.

Here, the procedure of temperature reduction by using ^{3}He handling system is as follows.

1. Evacuate the ^{3}He gas line. (First, hitch the vacuum pump into Aux1 and open V2, V3 and GV1, and then vacuum the ^{3}He line.)

2. Open V0 and enter ^{3}He Gas into ^{3}He pot.

3. Prepare pumping the liquid ^{3}He using the rotary vacuum pump (RP). (Close V1, GV1 and NV, and open GV2.)

4. Pump the liquid ^{3}He and lower the temperature. (First, Open NV and next, GV1 gradually.)

5. After pumping the liquid ^{3}He, close GV2 and open V1, then ^{3}He gas is condensed again.

3.3 Electrical resistivity measurement

The electrical resistivity was measured by an usual four probe AC method. The four probe AC method is used widely for the electrical resistivity measurement because this method can remove the influence of thermo-electromotive force and error by the contact resistance between the sample and the terminal. Moreover this method is very accurate and easy to measure. The resistance bridge (LR700) produced by Linear Research incorporated company is used. The temperature is determined by measuring the electrical resistivity of the semiconducting Cernox1050 thermometer above 1.5 K and RuO_2 down to 0.4 K. The temperature is measured by the temperature controller (LTC-21) by Neocera incorporated company.

Figure 3.10 shows the situation of the sample setting for the electrical resistivity measurement. The samples are cut into a parallel piped shape and fixed by indium which is glued on the sapphire plate. This plate is glued on the large Copper heat bath. Thus, a good thermal contact is obtained. The voltage terminals are jointed to the gold wire by indium as shown in Fig.3.10. The magnetic field is produced by the superconducting electro-magnet, and is controlled by IPS$^{120-10}$ produced by the OXFORD incorporated company. The temperature is controlled by LTC^{503} produced by the OXFORD incorporated company. The electrical resistivity was measured in a temperature region between 0.4 K and 13 K in magnetic fields up to 14.5 T. The ^{3}He refrigerator used in the present study was made by A. Kondo.
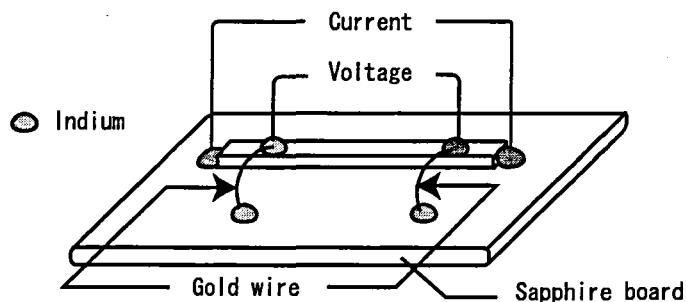
Fig. 3.10 Setting of the sample for the electrical resistivity measurement.

3.4 Magnetization measurements

3.4.1 Faraday method

Magnetization measurements in the temperature range of 0.4 to 3 K were performed using a capacitive Faraday magnetometer [70] at Sakakibara Laboratory, ISSP, Univ. Tokyo. It is known that one of the most popular method for the magnetization measurement is the subtraction method using the Superconducting Quantum Interference Device (SQUID). In this method, the sample moves inside a pick up coil to drive a time-varying magnetic flux. Then, the movement of this sample produces heat and warms up to the sample. On the other hand, in the Faraday method, as described later, the heat-up does not occur because the sample is moved only
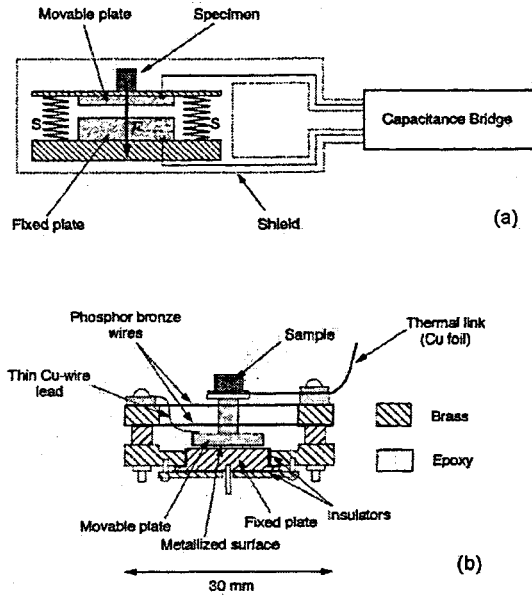
Fig. 3.11 (a) Schematic picture of the principle of the measurement. (b) Cross-sectional view of the load-sensing device [70].
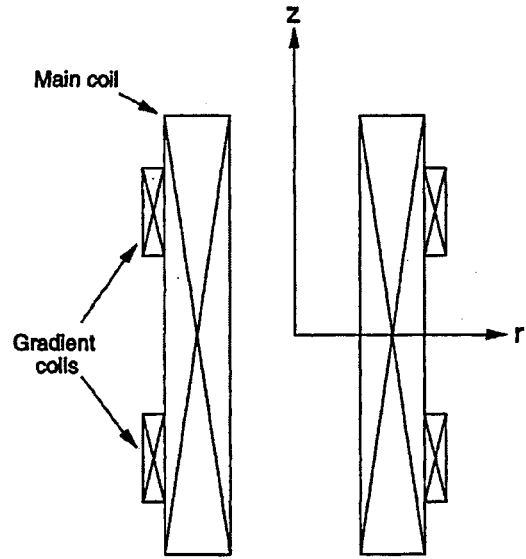
Fig. 3.12 Schematic diagram of a superconducting magnet for a Faraday balance experiment [70].

a little in the course of the measuring process. In this method, the variation of capacitance induced by the magnetic field gradient is measured and it is calibrated to the absolute value of the magnetization.

The principle of the measurement by the Faraday method is as follows.

Figure 3.11(a) shows the schematic picture of the principle of the measurement. A sample with the magnetization M is mounted on a small load-sensing device (load sell) made of a parallel-plate variable capacitor, whose movable plate is suspended by elastic springs as is shown in Fig.3.11(b). When the magnetic field gradient is applied to the magnetic sample, this sample will experience a force $F = -M\frac{dH}{dz}$. Here, we chose the direction of the field gradient as z direction. Suppose that F is directed perpendicular to the plates. The movable plate will then be pushed until the restoring force of the springs balances with F. Within an elastic deformation of the springs, the displacement of the plate is proportional to F. F is given by

$$F = -\kappa \Delta l, \tag{3.1}$$

where κ and l denote the constant of spring and the length between the plates, respectively. And then, the displacement of the plate, Δl can be detected as capacitance change, ΔC:

$$\Delta l = \epsilon_0 \Delta C. \tag{3.2}$$

Here, ϵ_0 and S denote the permittivity of vacuum and the dimensions of the plates, respectively. The capacitance change ΔC is given by $(1/C - 1/C_0)$. C is the capacitance where the field gradient is applied and C_0 denotes the unloaded capacitance. From (3.1) and (3.1), the magnitude of M is determined.

The superconducting magnet, produced by the OXFORD incorporated company, used in the present study is schematically shown in Fig.3.12. The main coil produces magnetic fields up to 9 T. The gradient coils are wound outside the main coil, and are capable of providing a vertical field gradient up to 10 T/m.

3.4.2 Extraction method by electromagnetic induction

In the extraction method, the magnetization is obtained by measuring the induced electromotive force. The schematic picture of the measurement system is shown in Fig.3.13.

In the initial condition, the magnetic sample is in a lower position out side the pick-up coil. By applying the magnetic field, the sample is magnetized. The sample is pulled up to a higher position outside the pick-up coil through the pick-up coil. As the position of the sample is changed in a pick-up coil with time, the induced electromotive force is

$$V = -S\frac{\partial \vec{B}_s \cdot \vec{n}}{\partial t}. \tag{3.3}$$

Here, $\vec{n}$ denotes a unit normal vector of the coil section, and S denotes the cross section of the coil. Output voltage is amplified by the Micro-volt meter (the Okura Denki incorporated company) and is shown as a function of time on a display, as shown in Fig.3.14. The magnetization is obtained by integrating the out put voltage as follows.

$$\mu M = -\frac{1}{S}\int_0^t V dt. \tag{3.4}$$

The integrated value is proportional to the area below or above zero line in Fig. 3.14. The temperature of the
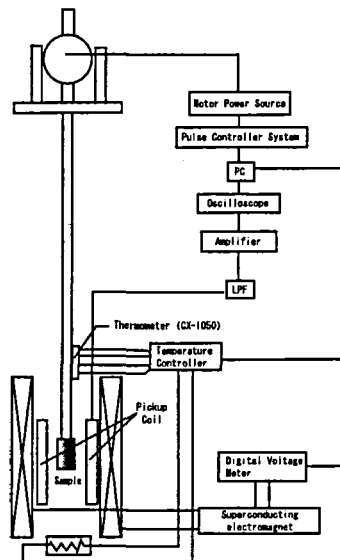
Fig. 3.13 Measurement system for magnetization by the electromagnetic induction method.
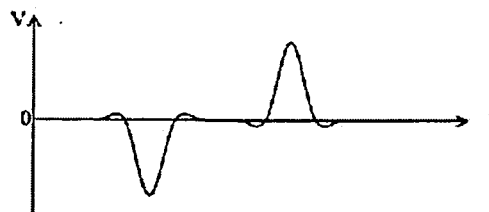
Fig. 3.14

sample is estimated by averaging that before and after the measurement process.

The microvoltagemeter (the Okura Denki incorporated company) is used for the measurement of the out put voltage. The temperature is determined by measuring the electrical resistivity of Cernox1050 produced by the Lakeshore incorporated company. The electrical resistivity of Cernox1050 is measured by using LTC21 produced by the Neocera incorporated company. The temperature is controlled by the LTC^{503} produced by the OXFORD corporation. The magnetic field is produced by the superconducting magnet and controlled by the IPS$^{120-10}$ produced by the OXFORD corporation. The region of temperature is between 1.5 and 12.0 K. The region of magnetic fields is up to 14.5 T.

Chapter 4

Mean Field Calculation for the Two-sublattice Model

Here, we show the results of mean field calculations for the two-sublattice model in which the O_{xy}-AFQ, T_{xyz}-AFO, T_β-AFO, and AF exchange interactions are taken into account and discuss the effect of the above three interactions on the T_β AFO order.

4.1 Introduction

In $Ce_xLa_{1-x}B_6$, T_Q and T_N are reduced with a decrease of x, and at $x \sim 0.8$, T_Q coincides with T_N due to their different suppression rates by La - doping. Phase IV appears at $x \sim 0.8$. [50,51] This indicates that the O_{xy}-AFQ and AF exchange interactions have almost the same magnitude as that of the interaction that forms phase IV at $x \sim 0.8$. As for the T_{xyz}-AFO interaction, its magnitude is expected to decrease in the same way as the O_{xy}-AFQ one, judging from the x dependence of the magnetic phase diagram. In such a situation, the magnitudes of the O_{xy}-AFQ, T_{xyz}-AFO, and AF exchange interactions, and the interaction that forms forming phase IV should be of the same order at least around $x \sim 0.75$. Thus, all the above interactions should be taken into account when we discuss the physical properties at $x \sim 0.75$.

As mentioned in the Introduction, the order in phase IV is said to be the T_β-AFO order. The wave vector Q=(1/2 1/2 1/2) of the O_{xy}-AFQ and T_{xyz}-AFO ordering in phase II is the same that in phase IV discovered in the resonant X-ray diffraction. This makes the two-sublattice model calculation in which the O_{xy}-AFQ, T_{xyz}-AFO and T_β-AFO ordering are taken into account meaning. As for the order parameter of the T_β-AFO order, we take the linear combination of T_β^x, T_β^y, and T_β^z, $(T_\beta^x+T_\beta^y+T_\beta^z)/\sqrt{3}$ as in the model proposed by Kubo and Kuramoto. [65]In their model, there exist four equivalent domains along the three-fold axis at H=0. For $H \parallel [001]$, these domains are equivalent. But they are not equivalent for $H \parallel [110]$, and [111]. In the present calculation, the single domain with the easy axis along the [111] direction is assumed. In this case, the results for $H \parallel [111]$ and [110] are different from those for $H \parallel [11\bar{1}]$ and $[1\bar{1}0]$, respectively, and this difference reflects the the difference of domain distribution depending on the applied field direction. Although the anisotropic behaviors are obtained below the AFO ordering temperature T_{oct}^β, the main conclusion in the present paper is not changed. The Hamiltonian used in the present calculation is as follows.

$$\mathcal{H} = \mathcal{H}_{\text{oct}(T_\beta)} + \mathcal{H}_{\text{Q}} + \mathcal{H}_{\text{oct}(T_{xyz})} + \mathcal{H}_{\text{ex}} + \mathcal{H}_{\text{Zeeman}} \qquad (4.1\text{a})$$

$$\mathcal{H}_{\text{oct}(T_\beta)} = -K_\beta \sum_{ij} T_\beta(i) \cdot T_\beta(j), \qquad (4.1\text{b})$$

$$\mathcal{H}_{\text{Q}} = -K_{\text{Q}} \sum_{ij} \left[O_{xy}(i) \cdot O_{xy}(j) + O_{yz}(i) \cdot O_{yz}(j) + O_{zx}(i) \cdot O_{zx}(j) \right], \qquad (4.1\text{c})$$

$$\mathcal{H}_{\text{oct}(T_{xyz})} = -K_{xyz} \sum_{ij} T_{xyz}(i) \cdot T_{xyz}(j), \qquad (4.1\text{d})$$

$$\mathcal{H}_{\text{ex}} = -J_{\text{ex}} \sum_{ij} J(i) \cdot J(j). \qquad (4.1\text{e})$$

In the present calculation, we chose the magnitude of the interactions as follows. As for K_β, we chose it so as to reproduce $T_{\text{oct}}^\beta=1.7$ K, which is the transition temperature from phase IV to I, $T^{\text{IV}-\text{I}}$, of $Ce_{0.75}La_{0.25}B_6$. The magnitudes of the transition temperatures such as $T_{\text{Q}}=0.5$ K, $T_{\text{oct}}^{xyz}=1$ K, and $T_{\text{N}}=1$ K shown in the present paper represent those of the O_{xy}-AFQ, T_{xyz}-AFO, and J_{ex} interactions when they exhibit the LRO independently, respectively. The ratio $\alpha = T_{\text{Q}}/T_{\text{oct}}^{xyz}=1.2$ is fixed in all the cases where the O_{xy}-AFQ and T_{xyz}-AFO interactions coexist.

4.2   Magnetic phase diagrams $(T_\beta + T_{\text{Q}} + T_{xyz})$

First, we show the magnetic phase diagrams obtained for the cases in which several multipole interactions coexist. Figure 4.1 shows the calculated results of the magnetic phase diagram. Hereafter, we refer to the O_{xy}-AFQ and paramagnetic phases as phase II and I, respectively. In the case (i) where $T_{\text{Q}}=0$ K, the pure T_β-AFO order takes place at $T_{\text{oct}}^\beta=1.7$ K. In the case (ii) where $T_{\text{Q}}=0.5$ K, the T_β-AFO order takes place and the critical field from the T_β-AFO phase to the paramagnetic phase is slightly enhanced. In the case (iii) where $T_{\text{Q}}=1.2$ K, phase II appears in the finite magnetic fields, while the ground state is the T_β-AFO ordered phase. This magnetic phase diagram is similar to that of $Ce_{0.7}La_{0.3}B_6$. The transition between the T_β-AFO and II phases is that of the first order, and the magnetization M exhibits a discontinuous jump. In the case (iv) where $T_{\text{Q}}=1.5$
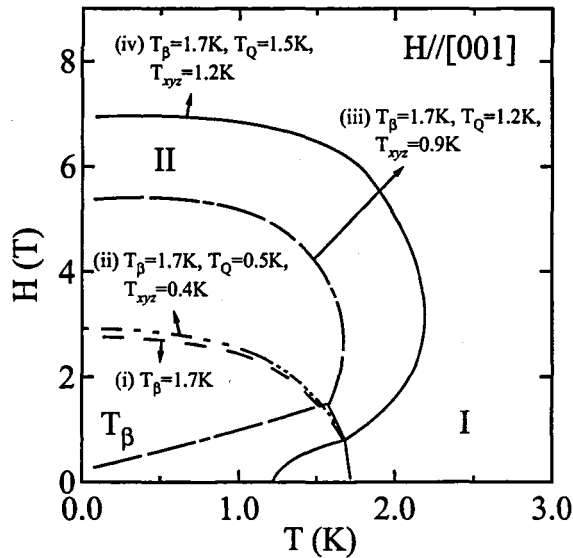
Fig. 4.1   Magnetic phase diagram obtained by mean field calculation for (i) $T_{\text{oct}}^\beta=1.7$ K, (ii) $T_{\text{oct}}^\beta=1.7$ K, $T_{\text{Q}}=0.5$ K, $\alpha=1.2$, (iii) $T_{\text{oct}}^\beta=1.7$ K, $T_{\text{Q}}=1.2$, $\alpha=1.2$, and (iv) $T_{\text{oct}}^\beta=1.7$ K, $T_{\text{Q}}=1.5$ K, $\alpha=1.2$. Here, $\alpha = T_{\text{Q}}/T_{\text{oct}}^{xyz}$.
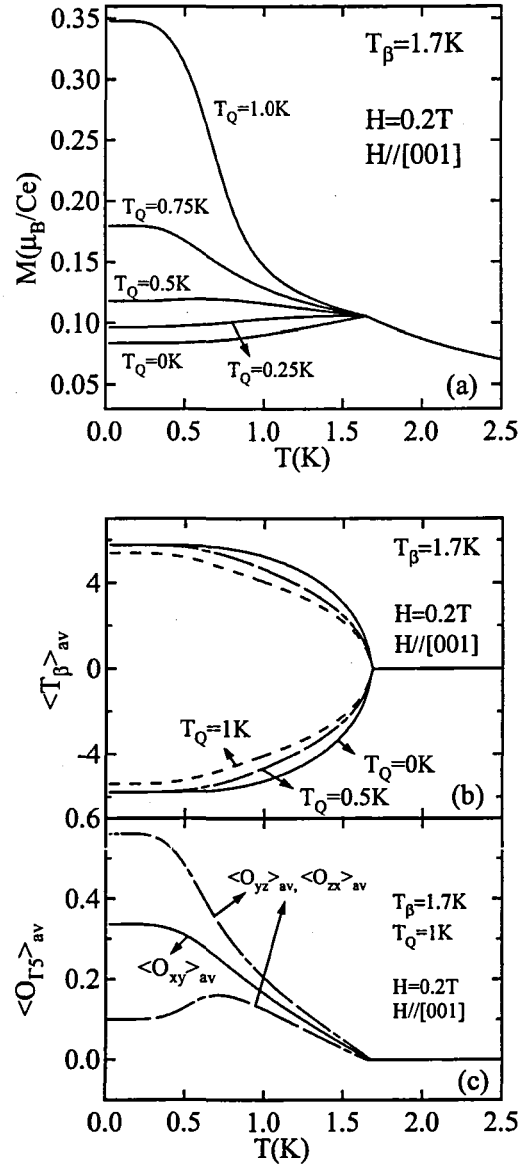
Fig. 4.2 Calculated results of the temperature dependence of (a) magnetization, M, (b) $\langle T_\beta \rangle_{av}$, and (c) $\langle O_{xy} \rangle_{av}$, $\langle O_{yz} \rangle_{av}(\langle O_{zx} \rangle_{av})$ at H=0.2 T along the [001] direction. In Fig.2 (c), the result of $\langle O_{xy} \rangle_{av}$ is shown by the thin solid line.

K, the T_β-AFO phase is reduced and the phase II region expands markedly. This magnetic phase diagram is similar to that of $Ce_{0.75}La_{0.25}B_6$ expect for the existence of AF magnetic phase III in the latter. The ground state is the O_{xy}-AFQ order, and T_Q increases with increasing magnetic field up to 3 T due to the coexistence of the O_{xy}-AFQ order and the T_{xyz}-AFO interaction. The T_β-AFO phase exists in a narrow temperature region between 1.2 K and 1.7 K and below 0.6 T. By applying the magnetic field, the effective ferromagnetic interaction caused by the coexistence of the O_{xy}-AFQ and T_{xyz}-AFO interactions overcomes the T_β-AFO phase with a small magnetization. The similarity of the magnetic phase diagrams between calculated cases ((iii), (iv)) and $Ce_xLa_{1-x}B_6$(x=0.7, 0.75), may provide some clues to understanding the physics of $Ce_xLa_{1-x}B_6$, although in the present calculation, the AF magnetic phase is not considered. Thus, as far as the magnetic phase diagram is concerned, the calculation seems to reproduce the real magnetic phase diagram of $Ce_xLa_{1-x}B_6$. However, as it

will be shown below, there exists a large difficultly to reproduce the magnetic properties in phase IV.
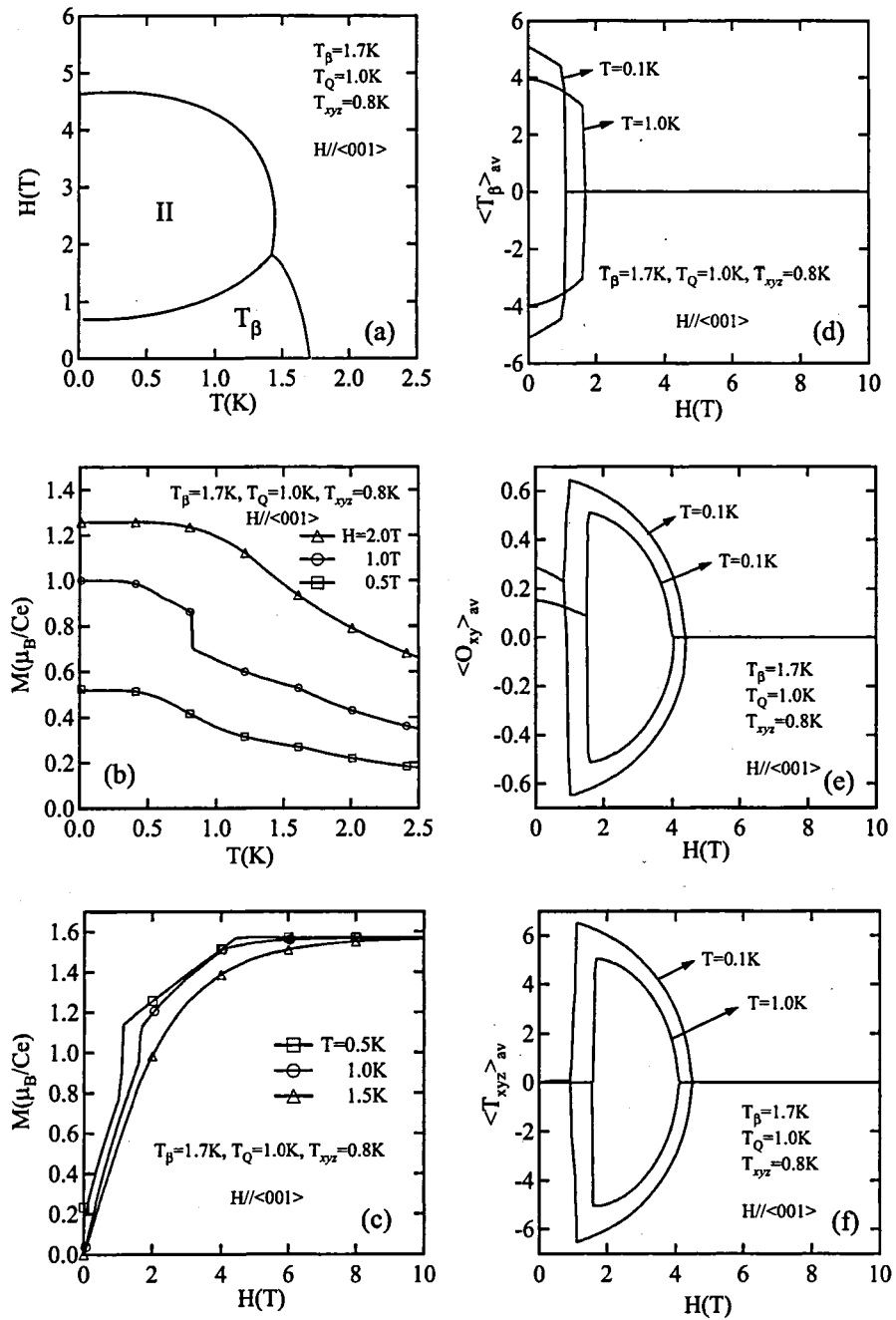
Fig. 4.3   Calculated results of (a) magnetic phase diagram, (b) temperature dependence of M at H=0.5T, 1T and 2T, (c) $M - H$ curve at T=0.5K, 1K and 1.5K, the H dependence of (d) $\langle T_\beta \rangle_{av}$, (e) $\langle O_{xy} \rangle_{av}$ and (f) $\langle T_{xyz} \rangle_{av}$. T^β_{oct}=1.7K, T_Q=1K, α=1.2 and $H \parallel$ [001]. Here, $\alpha = T_Q/T^{xyz}_{oct}$.
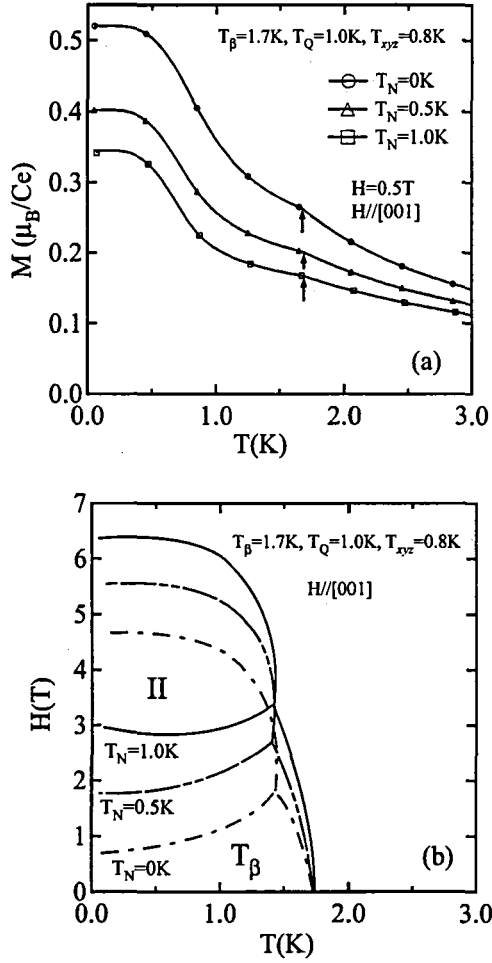
Fig. 4.4   Calculated results of (a) temperature dependence of M at H=0.5 T and (b) magnetic phase diagram for T_N=0 K, 0.5 K, and 1.0 K. T^β_{oct}=1.7 K, T_Q=1.0 K, and $\alpha = 1.2$.
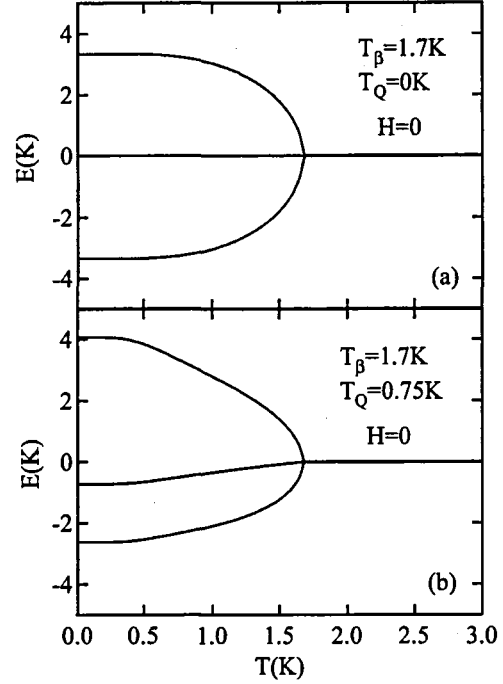
Fig. 4.5   Temperature dependence of the calculated energy levels at H=0. (a) T_β=1.7 K, and T_Q=0 K, and (b) T_β=1.7 K, and T_Q=0.75 K. The results correspond to those in Fig.2 (a).

4.3   Effect of the O_{xy}-AFQ interaction on the T_β-AFO order

Here, we show the effect of the O_{xy}-AFQ interaction on the T_β-AFO order. Figure 4.2 (a) shows the calculated results of the T dependence of M at H=0.2 T along the $\langle 001 \rangle$ direction. Figures 2(b) and 2(c) show the T dependence of $\langle T_\beta \rangle_{av}$ for T_Q=1 K, 0.5 K, and 0 K and $\langle O_{xy} \rangle_{av}(\langle O_{yz} \rangle_{av}, \langle O_{zx} \rangle_{av})$ for T_Q=1 K in H=0.2 T, respectively. As is shown in Fig. 4.2 (a), the peak of M at T^β_{oct}=1.7 K rapidly disappears when the O_{xy}-AFQ interaction is introduced and increases with decreasing temperature for $T_Q \geq 0.5$ K. However, in all the cases for $T_Q \leq 1$ K, the ground state is the T_β-AFO phase in H=0 as is shown in Fig. 4.2 (b). The magnitude of $\langle T_\beta \rangle_{av}$ is reduced from that without the O_{xy}-AFQ interaction as is shown in Fig. 4.2 (b). On the other hand, as for the quadrupole moments, the O_{xy} moment exhibits the FQ order but the AFQ component is induced for the O_{yz} and O_{zx} moments as is shown in Fig. 4.2 (c). We note that when the magnetic field is applied along the general direction against the crystal axis, the AFQ components of all the O_{xy}, O_{yz}, and O_{zx} operators are induced.

4.4   Case of T_β=1.7K T_Q=1K and T_{oct}^{xyz}=0.8K for $H \parallel$ [001]

Next, we show the T and H dependence of the multipole moments for T_Q=1K and T_{oct}^{xyz}=0.8K for $H \parallel \langle 001 \rangle$. Figure 4.3(a) shows the magnetic phase diagram. Figures 4.3(b) and (c) show the T or H dependence of M, respectively. Figures 4.3(d),(e),(f) show the H dependence of $\langle T_\beta \rangle_{av}$, $\langle T_{xyz} \rangle_{av}$ and $\langle O_{xy} \rangle_{av}$, respectively. The ground state is the T_β-AFO ordered phase and phase II exists at finite magnetic fields. At H=1T, a large discontinuous jump appears at the transition temperature, $T^{\beta-II}$, while a monotonous increase is obtained below T_{oct}^{β} at H=0.5T. The $M - H$ curve shows a discontinuous jump at the critical field from T_β to II phase, $H^{\beta-II}$. $\langle T_\beta \rangle_{av}$ has a finite magnitude in the T_β-AFO phase but is zero in phase II. In place, $\langle T_{xyz} \rangle_{av}$ and $\langle O_{xy} \rangle_{av}$ have finite values in phase II. In the T_β-AFO phase, $\langle T_{xyz} \rangle_{av}$=0 but $\langle O_{xy} \rangle_{av}$ has finite values of the FQ moment as is seen in Fig.4.3 (e).

4.5   Effect of the AF exchange interaction on the T_β-AFO phase

Next, we show the effect of the AF exchange interaction on the T_β-AFO phase. Figure 4.4 (a) shows the T dependence of M at H=0.5 T along the [001] direction for T_N=0, 0.5 K, and 1 K. Here, T_{oct}^{β}=1.7 K, T_Q=1 K, and T_{oct}^{xyz}=0.8 K. M is reduced in all the phases of T_β-AFO phase, phase II, and phase I, by introducing the AF exchange interaction. However, the increase in M below T_{oct}^{β} remains, and the peak of M at T_{oct}^{β} does not appear. Figure 4.4 (b) shows the magnetic phase diagram for the above three cases of T_N=0 K, 0.5 K, and 1 K. The critical fields $H^{\beta-II}$ and H^{II-I} are enhanced by introducing the AF exchange interaction, while T_{oct}^{β}=1.7 K at H=0 is not changed.

We examined the effect of the O_{xy}-AFQ and T_{xyz}-AFO interactions on the magnetic anisotropy in the T_β-AFO phase. The calculation was performed in the single domain with the easy axis along the [111] direction. The applied magnetic field is along the [001], [110], [111], [1$\bar{1}$0], and [11$\bar{1}$] directions. An increase in χ below T_{oct}^{β} is observed in all the cases, and the magnetic anisotropy as in the case of the pure T^β-AFO phase continues to exist. This may originate from the fact that the effective ferromagnetic interaction caused by the coexistence of the O_{xy}-AFQ and T_{xyz}-AFO interactions is nearly isotropic.

4.6   Reason for disappearance of the peak

The reason why the peak disappears when the O_{xy}-AFQ interaction is introduced is explained as follows. M in the T_β-AFO phase without any other interaction exhibits a peak at T_{oct}^{β}=1.7 K. However, this peak disappears easily when the O_{xy}-AFQ interaction is introduced, and with increasing the strength of the O_{xy}-AFQ interaction, M becomes to show the increase with decreasing temperature, which is pronounced when the O_{xy}-AFQ interaction is large.

The increase in M with decreasing temperature in the T_β-AFO phase is explained as follows. In the pure T_β-AFO phase, the ground state is a nonmagnetic singlet but has an O_{xy}-FQ moment. In such a situation, the O_{xy}-AFQ interaction should compete with the O_{xy}-FQ moment. Figures 4.5 (a) and 4.5 (b) show the calculated results of the temperature dependence of the energy levels for (a) T_β=1.7 K and T_Q=0 K, and (b) T_β=1.7 K and T_Q=0.75 K at H=0, respectively. By introducing the O_{xy}-AFQ interaction, the temperature dependence of the energy levels becomes asymmetric, and the energy difference between the ground state and the doubly degenerate magnetic first excited states is reduced. This reduction of the energy level splitting enhances the Van-Vleck-type paramagnetism below T^{IV-I}.

As described above, it is revealed that it is difficult to explain the overall features of $Ce_xLa_{1-x}B_6$ by introducing the other interactions which is not taken into account in the T_β-AFO model.

Chapter 5

Experimental Results

5.1 $Ce_{0.7}Nd_yLa_{0.3-y}B_6$ ($x = 0.7$)

Before performing the experiments, we considered the following two possible behaviors of χ for the rare-earth magnetic ion doped $Ce_{0.7}La_{0.3}B_6$.

(i) AF magnetic phase is realized in phase IV.

The magnetic impurity may contribute to the long range magnetic ordering. The temperature dependence of χ originating from the $\chi_\perp$ and $\chi_\parallel$ may be observed.

(ii) T_β-AFO ordered phase is realized in phase IV.

The Curie like magnetic susceptibility may be observed at low temperatures well below T_{IV-I} because the magnetic impurity does not couple with a singlet ground state of the T_β-AFO ordering.

5.1.1 $Ce_{0.7}Nd_{0.005}La_{0.295}B_6$

Figure 5.2 shows the temperature (T) dependence of M of $Ce_{0.7}Nd_{0.005}La_{0.295}B_6$ for $H \parallel [001]$. At $H = 0.1$ T, after showing a peak at $T \sim 1.4$ K, M shows a monotonous decrease with decreasing temperature. The T dependence of M around at $T \sim 1.4$ K is similar to that around at T_{IV-I} of $Ce_{0.7}La_{0.3}B_6$ [53]. This indicates that phase IV is realized below 1.4 K also in the present sample. However, at least down to 0.5 K below 1.4 K, we could not observe the Curie-like behavior in the $M - T$ curve. This peak of M due to the I-IV transition shifts slightly toward lower temperature with increasing magnetic field up to $H \sim 1$ T. At $H = 0.5$ T, the increase of M is observed below $T \sim 0.65$ K. This is considered to be the IV-III transition. This increase of M is clearly observed at $H = 0.7$ T below $T \sim 0.95$ K. At $H = 1.5$ T, we could not observe a peak at T_{IV-I}, but a kink due to the I-II transition at $T \sim 1.9$ K.

Fig. 5.1 Expected behavior of the magnetic susceptibility. (a) In the case of where AF magnetic phase is realized in phase IV. (b) In the case of where T_β-AFO ordered phase is realized in phase IV.

Figure 5.3 shows the magnetization curve of $Ce_{0.7}Nd_{0.005}La_{0.295}B_6$ for $H \parallel [001]$. At $T = 0.5$ K, M increases linearly with increasing magnetic field up to $H \sim 0.4$ T, which also indicates that the low magnetic field region below $H \sim 0.4$ T is phase IV. With further increase of magnetic field, M shows a discontinuous increase at $H \sim 0.4$ T accompanied with
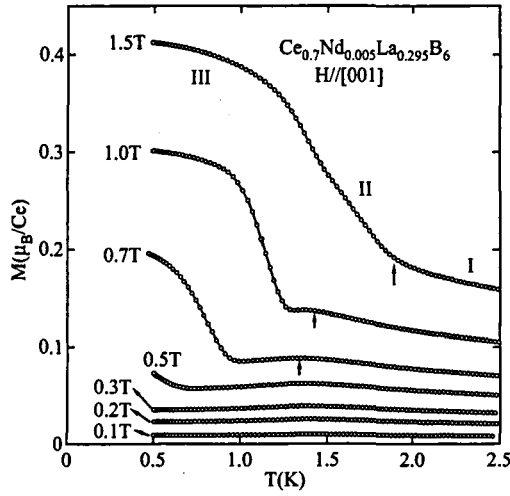
Fig. 5.2 Temperature dependence of the magnetization of $Ce_{0.7}Nd_{0.005}La_{0.295}B_6$ for $H \parallel [001]$.
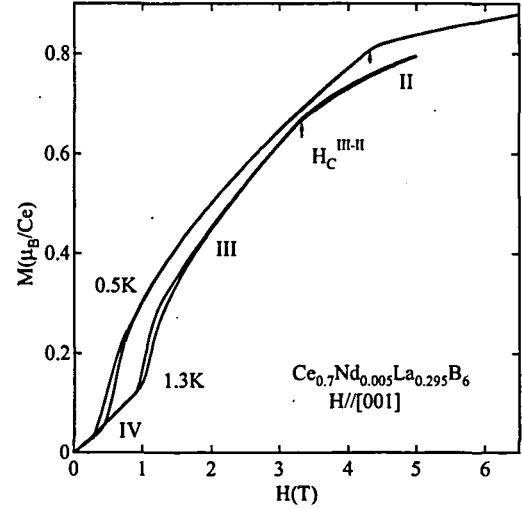
Fig. 5.3 Magnetization curve of $Ce_{0.7}Nd_{0.005}La_{0.295}B_6$ for $H \parallel [001]$.
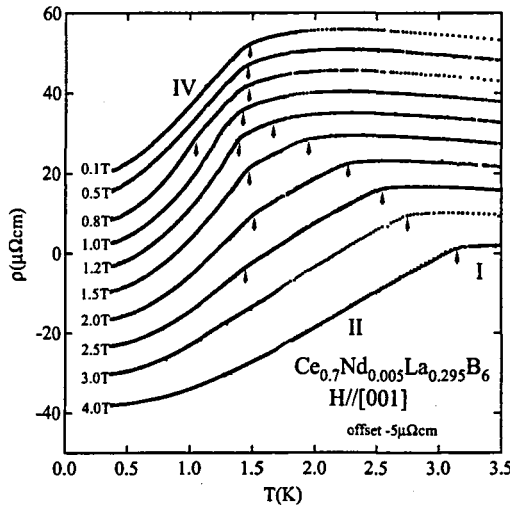
Fig. 5.4 Temperature dependence of the electrical resistivity of $Ce_{0.7}Nd_{0.005}La_{0.295}B_6$ for $H \parallel [001]$.
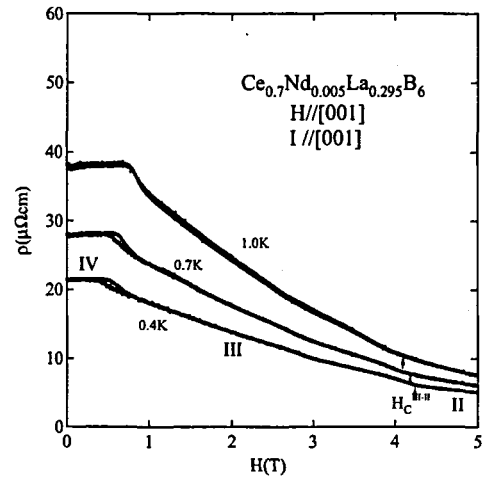
Fig. 5.5 Magnetic field dependence of the electrical resistivity of $Ce_{0.7}Nd_{0.005}La_{0.295}B_6$ for $H \parallel [001]$.

a hysteresis, which corresponds to the III-IV transition. This discontinuous increase is considerably smaller than the large jump observed in $Ce_{0.7}La_{0.3}B_6$ [53]. That is, the ferromagnetic (FM) component induced by a magnetic field in phase III is largely reduced by the Nd doping, although the FM component exists. At $H \sim 4.3$ T, a kink is recognized, which corresponds to the III-II transition. M shows a gradual increase in phase II. At $T \sim 1.3$ K, M increases linearly with increasing magnetic field up to $H \sim 1.0$ T and then shows a jump which originates from the IV-III transition. At $H \sim 3.3$ T, we observe a kink in the $M - H$ curve which corresponds to the III-II transition.

Figure 5.4 shows the temperature dependence of ρ of $Ce_{0.7}Nd_{0.005}La_{0.295}B_6$ for $H \parallel [001]$. The electrical current flows along the [001] direction. The origin of the vertical axis of ρ is shifted by $5\mu\Omega$cm in each curve. For $0 < H < 0.5$ T, ρ exhibits a rapid decrease at $T \sim 1.4$ K, which indicates the I-IV transition. At $H = 0.8$ T, the other anomaly appears at $T \sim 1.0$ K. This anomaly originates from the IV-III transition, T_N^{IV-III}. With increasing magnetic field, while T_{IV-I} slightly decreases, T_N^{IV-III} increase and coincides with T_{IV-I} at $H \sim 1.1$ T and $T \sim 1.3$ K. At $H = 1.2$ T, we observe two anomalies. The higher transition temperature rapidly shifts

to higher temperatures with increasing magnetic field, which corresponds to the I-II transition. On the other hand, the lower transition temperature corresponds to T_N^{II-III}. T_N^{II-III} does not change so much with increasing magnetic field. In the present experiment, T_N^{II-III} is recognized up to $H \sim 2.5$ T.

Figure 5.5 shows the H dependence of ρ of Ce$_{0.7}$Nd$_{0.005}$La$_{0.295}$B$_6$ for $H \parallel [001]$. A small H dependence of ρ is observed at lower magnetic fields. At $T \sim 0.4$ K, the steep decrease accompanying with a small hysteresis is observed at $H \sim 0.4$ T, which corresponds to the critical field from phase IV to III, H_c^{IV-III}. With increasing temperature, H_c^{IV-III} shifts slightly to higher magnetic fields. In addition, a kink is recognized at $H \sim 4.2$ T and $T = 0.4$ K, which indicates the critical field from phase III to II, H_c^{III-II}. H_c^{III-II} is also observed at $T \sim 0.7$ K and 1.0 K, and shifts to lower magnetic fields.

5.1.2 Ce$_{0.7}$Nd$_{0.01}$La$_{0.29}$B$_6$

Figure 5.6 shows the temperature dependence of the specific heat of Ce$_{0.7}$Nd$_{0.01}$La$_{0.29}$B$_6$ at zero magnetic field. The result of Ce$_{0.7}$La$_{0.3}$B$_6$ is also shown. A sharp peak is observed at $T \sim 1.4$ K, which is quite similar to that of Ce$_{0.7}$La$_{0.3}$B$_6$. This result indicates that phase IV is realized below 1.4 K in the present sample. In addition, a broad shoulder is confirmed at $T \sim 1.0$ K. As will be mentioned below, this shoulder corresponds to the IV-III transition.

Figure 5.7 shows the temperature dependence of M of Ce$_{0.7}$Nd$_{0.01}$La$_{0.29}$B$_6$ in the form of M/H for $H \parallel [001]$. M shows a peak at 1.4 K and an increase below 0.8 K at $H = 0.1$ T. This result is very similar to that of Ce$_{0.75}$La$_{0.25}$B$_6$ [53], and we conclude that in the present sample, three phases, i.e., I, IV, and III, exist at low magnetic fields. The present results indicate that the ground state is easily changed from phase IV to III by a small amount of Nd doping. Here, we explain the results at $H = 0.1$ T in detail. For $H = 0.1$ T, two $M/H-T$ curves are drawn. One is obtained by decreasing the temperature at $H = 0.1$ T. The other is obtained by increasing the temperature after a magnetic field of up to 1 T is applied and cooled down to $H = 0.1$ T at $T = 0.5$ K. Although M shows a peak at 1.4 K in both cases, different behaviors are observed below 0.8 K, depending on the above mentioned different measuring processes. In the latter process, M takes a large value below 0.8 K, while in the former, it is small. A large value of M below 0.8 K implies that the FM component is induced by the magnetic field in phase III. Although a similar behavior is also observed for $H = 0.2$ T and 0.3 T, the difference between the above two measuring processes becomes smaller with increasing magnetic
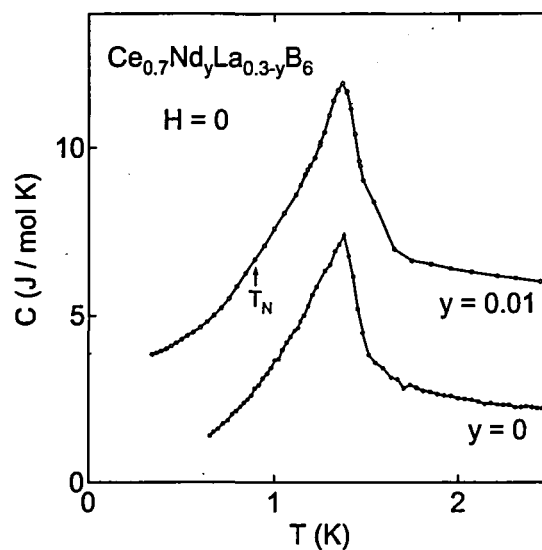
Fig. 5.6   Temperature dependence of the specific heat of Ce$_{0.7}$Nd$_{0.01}$La$_{0.29}$B$_6$ and Ce$_{0.7}$La$_{0.3}$B$_6$ at zero magnetic field.
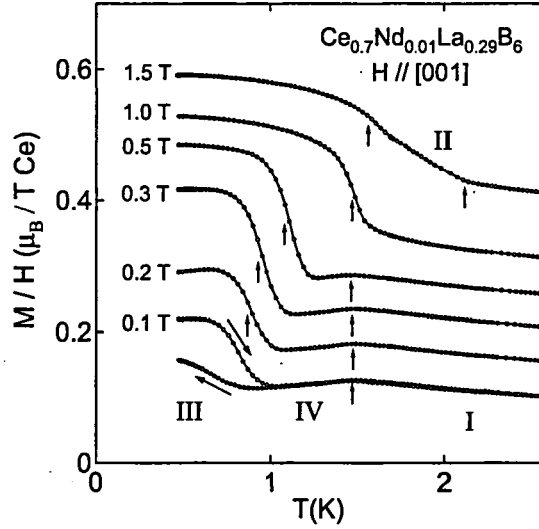
Fig. 5.7 Temperature dependence of the magnetization of $Ce_{0.7}Nd_{0.01}La_{0.29}B_6$ for $H \parallel [001]$. The origin of the vertical axis of each curves is shifted so as to see it easily. Two curves are drawn for $H = 0$. One is obtained by increasing the temperature and the other by decreasing the temperature. Refer to the text for details.

field, which indicates the existence of a large hysteresis in the magnetization curve at low magnetic fields. At $H = 1.0$ T, a cusp could not be observed but a rapid increase of M is observed at $T \sim 1.5$ K, indicating the phase transition from phase III. At $H = 1.5$ T, two anomalies are observed at $T \sim 2.1$ K and $T \sim 1.6$ K, which correspond to T_Q and T_N, respectively.

Figure 5.8 shows the temperature dependence of ρ of $Ce_{0.7}Nd_{0.01}La_{0.29}B_6$ for $H \parallel [111]$. Figure 5.9 shows the magnetoresistance. Below $H = 0.8$ T, the $\rho-T$ curves show a clear kink at $T_{IV-I} \sim 1.4$ K, as observed in $Ce_{0.7}La_{0.3}B_6$. [55] For $H = 0$, two $\rho-T$ curves are drawn. One is obtained by decreasing the temperature at $H = 0$. The other is obtained by increasing the temperature after a magnetic field of up to 1 T is applied and cooled down to $H = 0$. Although ρ shows a clear anomaly at 0.8 K in the latter, the anomaly is very small in the former. The origin of the difference between the above two results is the same as that of the $M-T$ curves at $H = 0.1$ T, as mentioned above. That is, a large hysteresis exists at low magnetic fields, as shown in Fig. 5.9. In the initial run after zero field cooling, phase IV with a large value of ρ appears to coexist with phase III. Hereafter, we refer to the phase where phases III and IV coexist as phase (III + IV). Nearly half of the sample belongs to phase III and the other half to phase IV. This indicates that phases III and IV are not compatible with each other and suggests that phase IV is not the magnetic dipole ordered phase. The other $\rho-T$ curves are obtained by the measurement with decreasing temperature at $H = 0.1$ T and 0.5 T. The decrease below 0.8 K for $H = 0.5$ T is very large. This implies that at $H = 0.5$ T, phase III and not phase (III + IV) is realized below 0.8 K. In Fig. 5.8 , two anomalies are recognized above 1.2 T. The anomaly at higher temperatures corresponds to the I-II transition, and that at lower temperatures to the II-III transition. The II-III transition could be observed at $H = 2.0$ T.

5.1.3 $Ce_{0.7}Nd_{0.03}La_{0.27}B_6$

Figure 5.10 shows the temperature dependence of the specific heat of $Ce_{0.7}Nd_{0.03}La_{0.27}B_6$. The result of $Ce_{0.7}La_{0.3}B_6$ is also shown. Compared with the results of $Ce_{0.7}La_{0.3}B_6$ and $Ce_{0.7}Nd_{0.01}La_{0.29}B_6$, the present sample shows a enormously large and sharp peak at $T \sim 1.4$ K. This indicates that the energy splitting below the transition temperature is much larger than that of $Ce_{0.7}La_{0.3}B_6$ and $Ce_{0.7}Nd_{0.01}La_{0.29}B_6$. Thus, the large peak in the present sample is probably not due to the I-IV transition, but the I-III transition.
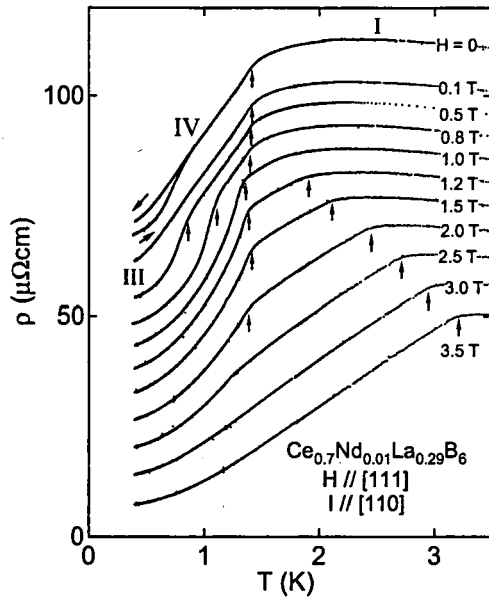
Fig. 5.8 Temperature dependence of the electrical resistivity of Ce$_{0.7}$Nd$_{0.01}$La$_{0.29}$B$_6$ for $H \parallel [111]$. Two curves are drawn for $H = 0$. Refer to the text for details.
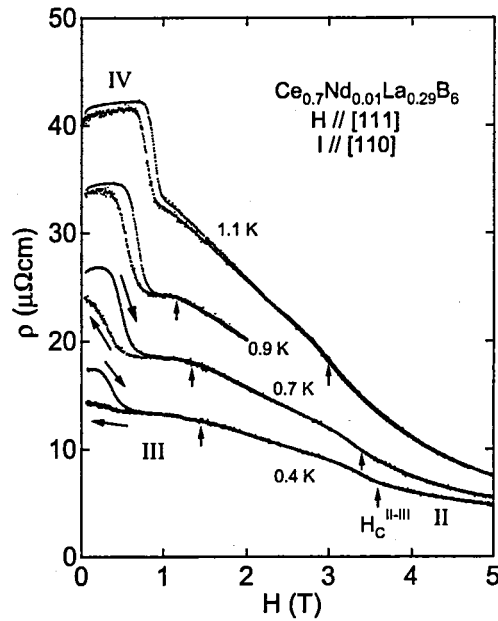
Fig. 5.9 Magnetic fi eld dependence of the electrical resistivity of Ce$_{0.7}$Nd$_{0.01}$La$_{0.29}$B$_6$ for $H \parallel [111]$.

Figure 5.11 shows the temperature dependence of ρ of Ce$_{0.7}$Nd$_{0.03}$La$_{0.27}$B$_6$ for $H \parallel [001]$. The electrical current flows along the [110] direction. The origin of the vertical axis of ρ is shifted by $5\mu\Omega$cm in each curves. At $H = 0$, ρ shows a rapid decrease at $T \sim 1.4$ K. The rapid decrease of ρ is recognized up to 0.7 T and shifts slightly to lower temperature with increasing magnetic field. The decreasing rate of ρ of the present sample is larger than that for Ce$_{0.7}$Nd$_y$La$_{0.3}$B$_6$ ($y = 0$, 0.005 and 0.01) at $T_{\mathrm{IV-I}}$. This indicates that the rapid decrease of ρ originates from the I-III transition. This result is consistent with that of the specific measurement as shown in Fig. 5.10. At $H = 1.1$ T, T_{Q} and $T_{\mathrm{N}}^{\mathrm{II-III}}$ are recognized. With increasing magnetic field up to 2.5T, $T_{\mathrm{N}}^{\mathrm{II-III}}$
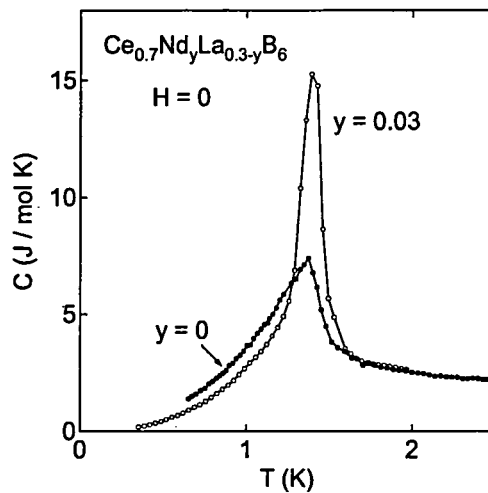
Fig. 5.10 Temperature dependence of the specifi c heat of Ce$_{0.7}$Nd$_{0.03}$La$_{0.27}$B$_6$. The result of Ce$_{0.7}$La$_{0.3}$B$_6$ is also shown.
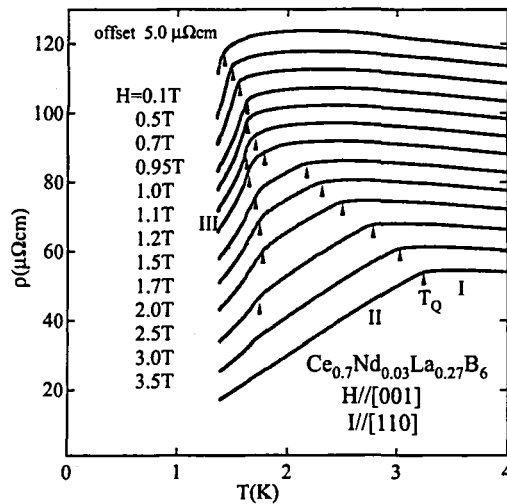
Fig. 5.11 Temperature dependence of the electrical resistivity of $Ce_{0.7}Nd_{0.03}La_{0.27}B_6$ for $H \parallel [001]$.
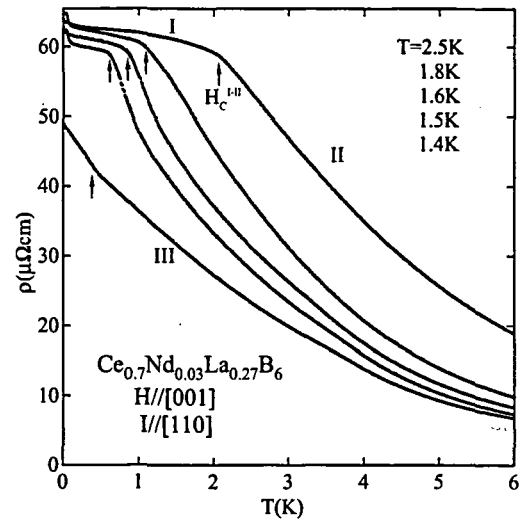
Fig. 5.12 Magnetic field dependence of the electrical resistivity of $Ce_{0.7}Nd_{0.03}La_{0.27}B_6$ for $H \parallel [001]$.

shifts to higher temperatures.

Figure 5.12 shows the H dependence of ρ of $Ce_{0.7}Nd_{0.03}La_{0.27}B_6$ for $H \parallel [001]$. A kink is observed at $T = 2.5$ K and $H \sim 2.1$ T. This anomaly is also observed at $T \sim 1.8$ K. Considering the result of CeB_6, we concluded that these anomalies originate from the I-II transition. On the other hand, at $T = 1.5$ K and 1.6 K, two anomalies are observed. The decreasing rate of ρ just above the critical field of these transitions is larger than that of the I-II transition at $T = 2.5$ K and 1.8 K. This indicates that these anomalies probably originate from the I-III transition. At $T = 1.4$ K, the value of ρ at zero field becomes smaller than that at $T = 1.5$ K. This means that the zero magnetic field region at $T = 1.4$ K is phase III. An anomaly, which is observed at $T = 1.4$ K and $H \sim 0.45$ T, may be originate from the change of the domain distribution.
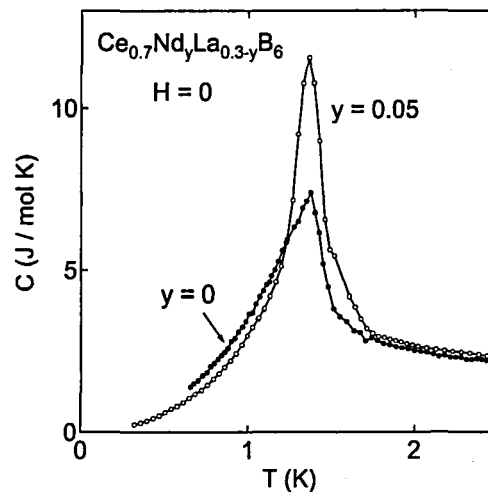
Fig. 5.13 Temperature dependence of the specific heat of $Ce_{0.7}Nd_{0.05}La_{0.25}B_6$. The result of $Ce_{0.7}La_{0.3}B_6$ is also shown.
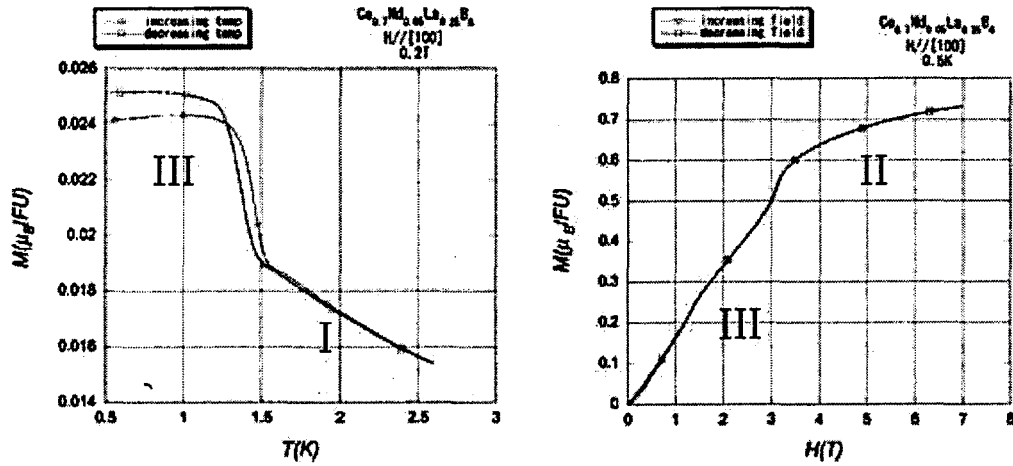
Fig. 5.14 Right side : Temperature dependence of the magnetization of Ce$_{0.7}$Nd$_{0.05}$La$_{0.25}$B$_6$. Left side : Magnetization curve of Ce$_{0.7}$Nd$_{0.05}$La$_{0.25}$B$_6$.
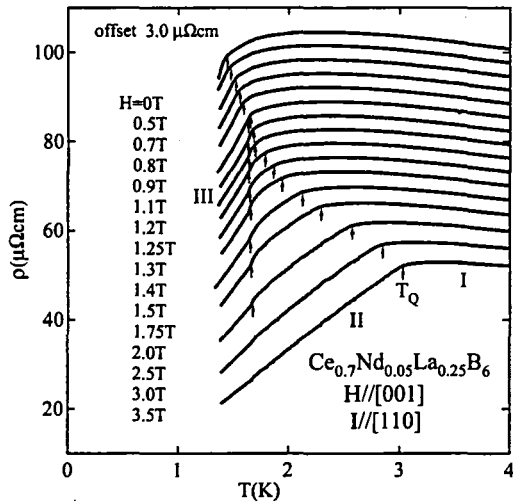
Fig. 5.15 Temperature dependence of the electrical resistivity of Ce$_{0.7}$Nd$_{0.05}$La$_{0.25}$B$_6$ for $H \parallel$ [001].
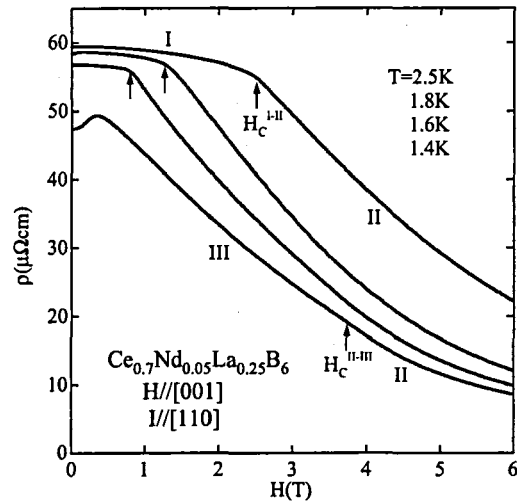
Fig. 5.16 Magnetic fi eld dependence of the electrical resistivity of Ce$_{0.7}$Nd$_{0.05}$La$_{0.25}$B$_6$ for $H \parallel$ [001].

5.1.4 Ce$_{0.7}$Nd$_{0.05}$La$_{0.25}$B$_6$

Figure 5.13 shows the temperature dependence of the specific heat of Ce$_{0.7}$Nd$_{0.05}$La$_{0.25}$B$_6$. The result of Ce$_{0.7}$La$_{0.3}$B$_6$ is also shown for comparison. A large and sharp peak is observed at $T \sim$ 1.4 K, which is quite similar to that of Ce$_{0.7}$Nd$_{0.03}$La$_{0.27}$B$_6$. Thus, the ground state of this compound is considered to be phase III.

Figure 5.14 shows the temperature dependence of the magnetization at H = 0.2 T and the magnetic field dependence of the magnetization at T = 0.5 K of Ce$_{0.7}$Nd$_{0.05}$La$_{0.25}$B$_6$, respectively. With decreasing temperature, the M-T curve exhibits a large increase below $T \sim$1.5K. On the other hand, in the M-H curve, M shows a linear increase with increasing H up to $H \sim$ 3 T, which implies that the lower magnetic field region below $H \sim$ 3 T is the AF magnetic phase. These results strongly suggest that O_{xy}-AFQ ordering and T_{xyz}-AFO ordering coexist in phase III.

Figure 5.15 shows the temperature dependence of ρ of Ce$_{0.7}$Nd$_{0.05}$La$_{0.25}$B$_6$ for $H \parallel$ [001]. The electrical current flows along the [110] direction. The origin of the vertical axis of ρ is shifted by 5$\mu\Omega$cm in each curves. At
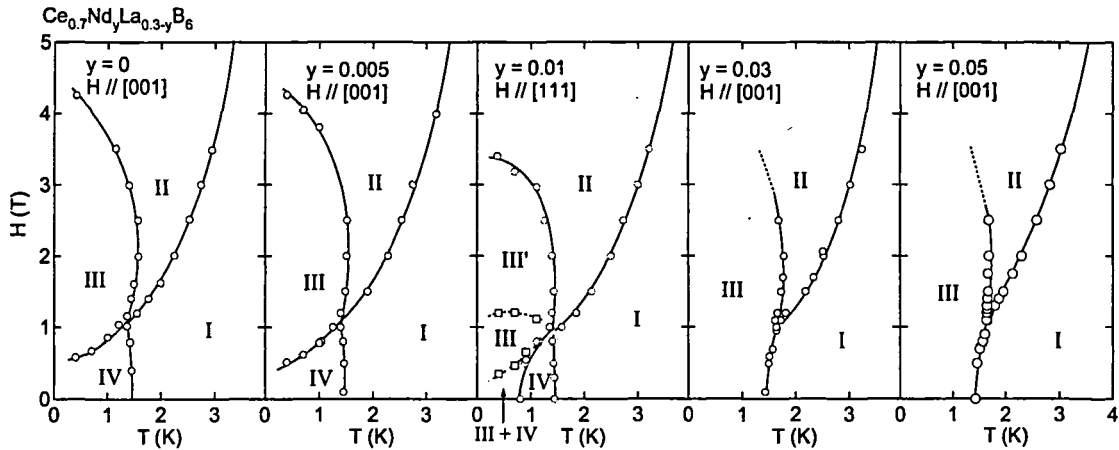
$Ce_{0.7}Nd_yLa_{0.3-y}B_6$

Fig. 5.17 Magnetic phase diagram of $Ce_{0.7}Nd_yLa_{0.3-y}B_6$ ($y = 0, 0.005, 0.01, 0.03$ and 0.05).

the zero magnetic field, a rapid decrease of ρ is recognized at $T \sim 1.4K$ as well as that of $Ce_{0.7}Nd_{0.03}La_{0.27}B_6$, indicating the the I-III transition. With increasing magnetic field, T_N^{I-III} shifts to higher temperatures. With further increase of magnetic field up to $H \sim 1.1T$, two anomalies are observed. These two anomalies corresponds to T_Q and T_N^{II-III}, respectively. In this compound, ρ shows a small jump at T_N^{II-III} around the tri-critical point. This behavior is not observed in $Ce_{0.7}Nd_{0.03}La_{0.27}B_6$.

Figure 5.16 shows the H dependence of ρ of $e_{0.7}Nd_{0.05}La_{0.25}B_6$ for $H \parallel [001]$. A kink is observed at $T = 2.5$ K, $1.8K$ and $1.6K$ in the low magnetic fields, which corresponds to the I-II transition. At $T = 1.4K$, there exists two anomalies at $H \sim 0.35$ T and 3.75 T. The anomaly at $H \sim 3.75$ T should be originate from the II-III transition, while the other anomaly at $H \sim 0.35$ T should be ascribed to the change of the domain distribution.

5.1.5 Magnetic phase diagram of $Ce_{0.7}Nd_yLa_{0.3-y}B_6$

Figure 5.17 shows the magnetic phase diagrams of $Ce_{0.7}Nd_yLa_{0.3-y}B_6$ ($y = 0, 0.005, 0.01, 0.03$ and 0.05). The phase diagram for $y = 0.005$ is similar to that of $Ce_{0.7}La_{0.3}B_6$ [55] apart from a slightly smaller value of H_c^{IV-III}. This indicates that the effect of the Nd doping on phase IV is very small and the AFM interaction in phase III is slightly enhanced. Only a slight increase in the Nd doping from $y = 0.005$ to 0.01 changes the magnetic phase diagram from $Ce_{0.7}La_{0.3}B_6$-type to $Ce_{0.75}La_{0.25}B_6$-type. [53] However, being different from that of $Ce_{0.75}La_{0.25}B_6$, phase (III + IV) in $Ce_{0.7}Nd_{0.01}La_{0.29}B_6$ exists at low magnetic fields. For $y = 0.03$, only phase III exists below 1.4 K. Here, it should be noted that the first order phase transition directly from III to I, which does not exist in $Ce_xLa_{1-x}B_6$, exists at $T_N = 1.4$ K for $y = 0.03$. A similar magnetic phase diagram is obtained for $y = 0.05$, where T_N is also 1.4 K at $H = 0$. Thus, the Nd doping rapidly suppresses phase IV and stabilizes phase III. The other phase boundaries, namely, III-II and II-I, are not affected as much by the Nd doping.

5.2 $Ce_{0.65}Nd_yLa_{0.35-y}B_6$ ($x = 0.65$)

5.2.1 $Ce_{0.65}Nd_{0.02}La_{0.33}B_6$

Figure 5.18 and 5.19 show the T and H dependence of ρ of $Ce_{0.65}Nd_{0.02}La_{0.33}B_6$ for $H \parallel [001]$, respectively. The origin of the vertical axis of the $\rho - T$ curves is shifted by $5\mu\Omega cm$ in each curve. At zero magnetic field, the
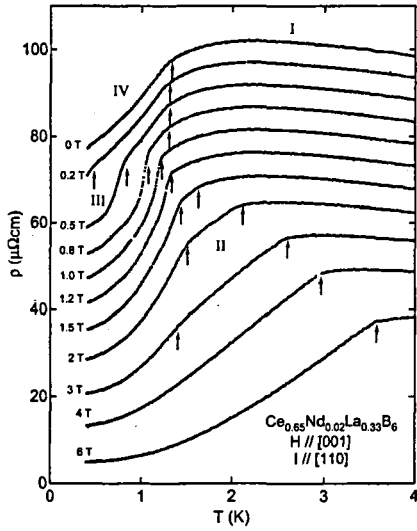
Fig. 5.18 Temperature dependence of the electrical resistivity of $Ce_{0.65}Nd_{0.02}La_{0.33}B_6$ for $H \parallel [001]$.
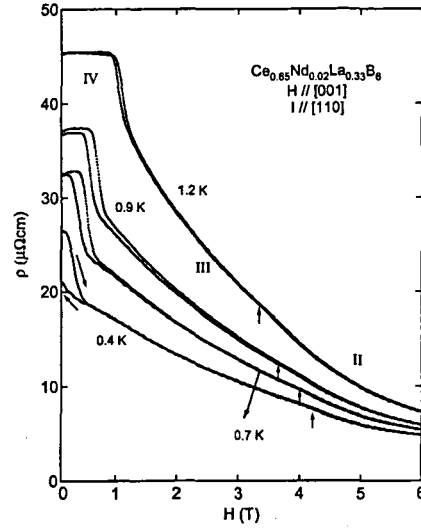
Fig. 5.19 Magnetic field dependence of the electrical resistivity of $Ce_{0.65}Nd_{0.02}La_{0.33}B_6$ for $H \parallel [001]$.

$\rho - T$ curve shows a kink at $T \sim 1.3$ K, which corresponds to the IV-I transition. At $H = 0.2$ T, after showing the kink at $T_{IV-I} \sim 1.3$ K, the $\rho - T$ curve exhibits a small decrease at $T \sim 0.45$ K, which originates from the IV-III transition. This IV-III transition is clearly observed at $H = 0.5$ T and 0.8 T. In the $\rho - H$ curve, a large hysteresis exists at low magnetic fields at $T = 0.4$ K. This indicates that the ground state of the present sample is the coexistent phases with phase IV and III, as is observed in $Ce_{0.7}Nd_{0.01}La_{0.29}B_6$. Below $H = 1.2$ K, the $\rho - H$ curves show a small H dependence at low magnetic fields, which provides the evidence that phase IV exists in the present sample. In the $\rho - T$ curve at $H = 1.5$ T, two anomalies are observed at $T \sim 1.6$ K and 1.4 K, which correspond to T_Q and T_N, respectively.
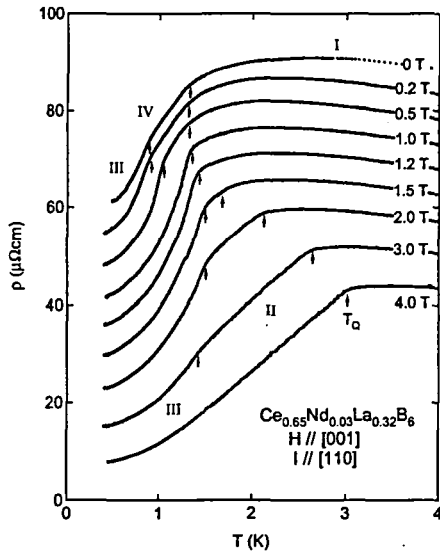
Fig. 5.20 Temperature dependence of the electrical resistivity of $Ce_{0.65}Nd_{0.03}La_{0.32}B_6$ for $H \parallel [001]$.
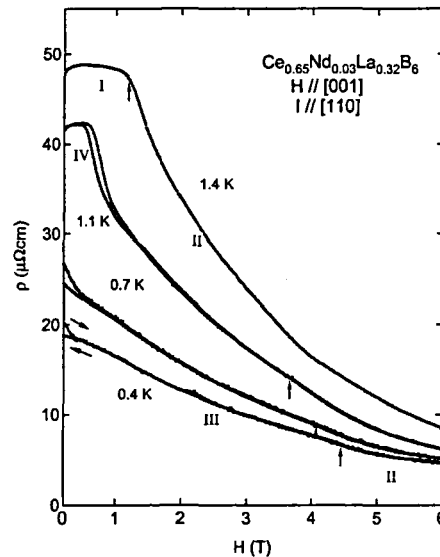
Fig. 5.21 Magnetic field dependence of the electrical resistivity of $Ce_{0.65}Nd_{0.03}La_{0.32}B_6$ for $H \parallel [001]$.
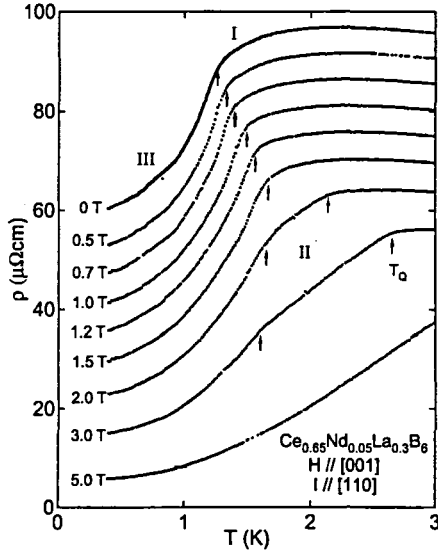
Fig. 5.22   Temperature dependence of the electrical resistivity of $Ce_{0.65}Nd_{0.05}La_{0.3}B_6$ for $H \parallel [001]$.
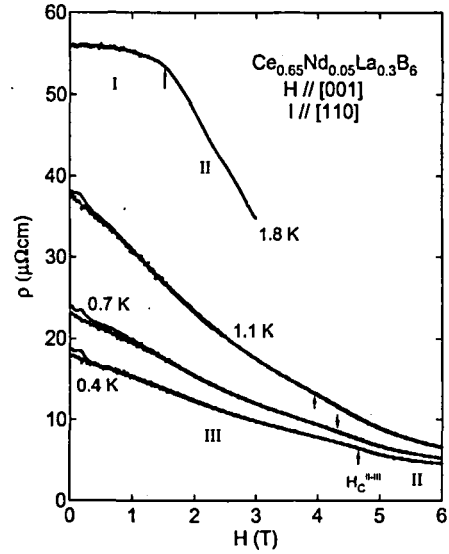
Fig. 5.23   Magnetic field dependence of the electrical resistivity of $Ce_{0.65}Nd_{0.05}La_{0.3}B_6$ for $H \parallel [001]$.

5.2.2 $Ce_{0.65}Nd_{0.03}La_{0.32}B_6$

Figure 5.20 shows the T dependence of ρ of $Ce_{0.65}Nd_{0.03}La_{0.32}B_6$ for $H \parallel [001]$. The origin of the vertical axis of ρ is shifted by $5\mu\Omega$cm in each curve. At zero magnetic field, two anomalies are observed at $T \sim 1.35$ K and $T \sim 0.9$ K. With increasing magnetic fields, the anomaly at $T \sim 1.35$ K slightly shifts to lower temperature, and the anomaly at $T \sim 0.9$ K shifts to higher temperature. This T dependence of ρ is similar to that of $Ce_{0.75}La_{0.25}B_6$ at low magnetic fields [30], and thus the anomalies at $T \sim 1.35$ K and $T \sim 0.9$ K correspond to the I-IV and the IV-III transition, respectively. At $H = 1.5$ T, T_Q and T_N are recognized at $T \sim 1.65$ K and $T \sim 1.5$ K, respectively. The anomaly of T_N could be observed up to $H = 3.0$ T.

Figure 5.21 shows the H dependence of ρ of $Ce_{0.65}Nd_{0.03}La_{0.32}B_6$ for $H \parallel [001]$. Below $T = 0.7$ K, a hysteresis also exists at low magnetic fields. However, The hysteresis in the present sample is much smaller than that in $Ce_{0.7}Nd_{0.01}La_{0.29}B_6$ and $Ce_{0.65}Nd_{0.02}La_{0.33}B_6$ originating from the coexistence with phase IV and phase III. Thus, these behaviors of ρ at low magnetic fields are probably ascribed to the change of the domain distribution. At $T = 1.1$ K, a small H dependence is observed below $H \sim 0.6$ T, which indicates the existence of phase IV. At $T = 1.4$ K, ρ also shows a small H dependence at low magnetic fields and a steep decrease at $H \sim 1.2$ T, which corresponds to the I-II transition. Below $T = 1.1$ K, a small anomaly originating from H_c^{III-II} is barely recognized at high magnetic fields.

5.2.3 $Ce_{0.65}Nd_{0.05}La_{0.3}B_6$

Figure 5.22 shows the $\rho - T$ curves of $Ce_{0.65}Nd_{0.05}La_{0.3}B_6$ for $H \parallel [001]$. The origin of the vertical axis of ρ is shifted by $5\mu\Omega$cm in each curve. At zero magnetic field, ρ shows a rapid decrease at $T \sim 1.35$ K with decreasing temperature. The rapid decrease of ρ was also found in $Ce_{0.7}Nd_{0.03}La_{0.27}B_6$ and thus this anomaly is ascribed to the I-III transition. The I-III transition shifts to higher temperatures with increasing H up to $H = 1.5$ T. For $H = 2.0$ T, two kinks are recognized, which corresponds to T_Q and T_N, respectively.

Figure 5.22 shows the $\rho - H$ curves of $Ce_{0.65}Nd_{0.05}La_{0.3}B_6$ for $H \parallel [001]$. Below $T = 1.1$ K, ρ decreases with increasing H, which indicates that phase IV disappears and only phase III exists at low magnetic fields. The small anomalies below $H \sim 0.3$ T may originate from the change of the domain distribution. At high

Ce$_{0.65}$Nd$_y$La$_{0.35-y}$B$_6$ H // [001]
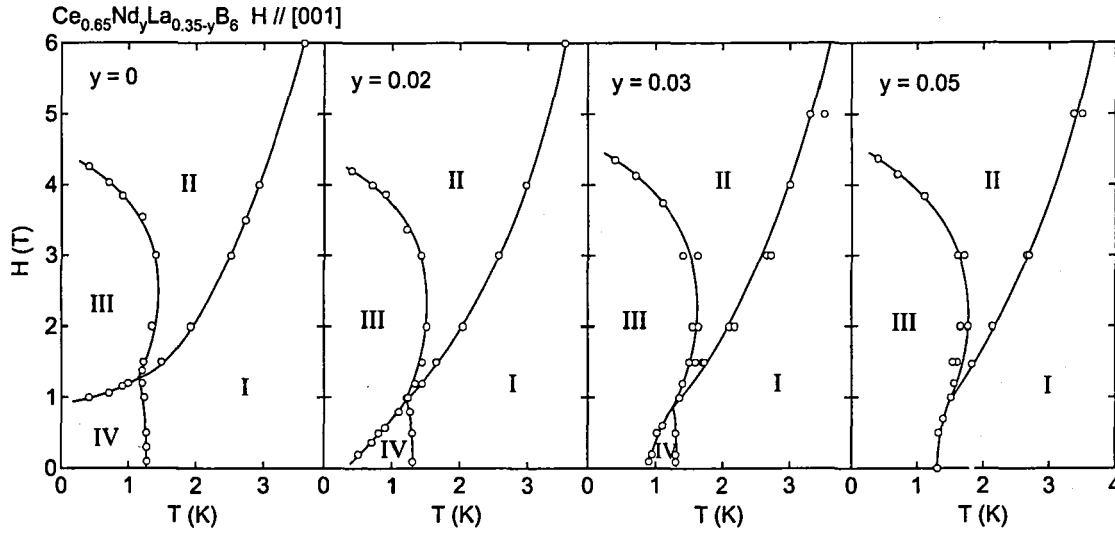
Fig. 5.24 Magnetic phase diagram of Ce$_{0.65}$Nd$_y$La$_{0.35-y}$B$_6$ ($y = 0, 0.02, 0.03$ and 0.05).

magnetic fields, H_c^{III-II} is barely recognized. At $T = 1.8$ K, ρ exhibits a small H dependence below $H \sim 1.5$ T and a steep decrease at $H \sim 1.5$ T, which corresponds to the I-II transition.

5.2.4 Magnetic phase diagram of Ce$_{0.65}$Nd$_y$La$_{0.35-y}$B$_6$

Figure 5.24 shows the magnetic phase diagrams of Ce$_{0.65}$Nd$_y$La$_{0.35-y}$B$_6$ ($y = 0, 0.02, 0.03$, and 0.05) for $H \parallel [001]$ obtained from the electrical resistivity measurement. The overall features are similar to those of Ce$_{0.7}$Nd$_y$La$_{0.3-y}$B$_6$. That is, phase IV is rapidly suppressed and phase III is stabilized by a small amount of Nd doping. For $y = 0.02$, the ground state becomes phase (IV+III) as observed in Ce$_{0.7}$Nd$_{0.01}$La$_{0.29}$B$_6$. For $y = 0.03$, phase III becomes the ground state and phase IV exists in a narrow region between 0.9 K and 1.35 K at the zero magnetic field. It should be noted that the transition temperature from phase II and III, T_N^{II-III} is almost the same temperature as T_{I-IV}. With increasing the Nd concentration from $y = 0.03$ to $y = 0.05$, phase IV disappears and only phase III exists at lower temperatures. At $T_N = 1.35$ K, the I-III boundary is observed as well as in Ce$_{0.7}$Nd$_{0.03}$La$_{0.27}$B$_6$.

5.3 Ce$_{0.6}$Nd$_y$La$_{0.4-y}$B$_6$ ($x = 0.6$)

5.3.1 The ground state of Ce$_{0.6}$Nd$_y$La$_{0.4-y}$B$_6$

Figure 5.25 (a) shows the T dependence of C of Ce$_{0.6}$Nd$_y$La$_{0.4-y}$B$_6$ ($y = 0, 0.05, 0.06$ and 0.08) at zero magnetic field. For $y = 0$, a peak corresponding to the phase transition from I to IV is observed at $T \sim 0.9$ K. C of $y = 0.05$ also shows the peak at $T \sim 1.1$ K, which is probably due to the I-IV transition. For $y = 0.06$, two sharp peaks are observed at $T \sim 1.4$ K and $T \sim 0.85$ K, respectively. By analogy with the Nd doping effect for $x = 0.7$, one might consider that these peaks originate from the I-IV and IV-III transition, respectively. However, the anomaly attributed to the IV-III transition is very small as shown in Fig. 5.6, in contrast to the sharp peak of $y = 0.06$ at $T \sim 0.85$ K. This indicates that the peak of the lower temperatures for $y = 0.06$ originates not from the IV-III transition but the other phase transition.

Figure 5.25 (b) shows the T dependence of M of Ce$_{0.6}$Nd$_{0.06}$La$_{0.34}$B$_6$ in the form M/H at $H = 0.1$ T for $H \parallel [001]$. As mentioned before, M of Ce$_x$La$_{1-x}$B$_6$ shows a cusp at T_{IV-I}. In the present sample, however, the
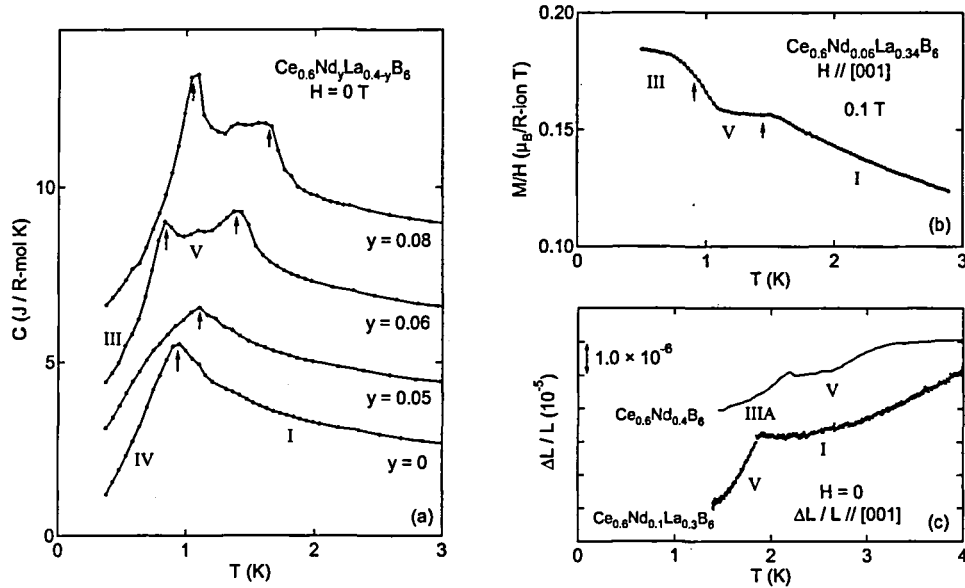
Fig. 5.25 (a) Temperature dependence of the specific heat of $Ce_{0.6}Nd_yLa_{0.4-y}B_6$ ($y = 0, 0.05, 0.06$ and 0.08) at zero magnetic field. The origin of the vertical axis of C is shifted by 2 J/R-mol K in each curve. (b) Temperature dependence of the magnetization of $Ce_{0.6}Nd_{0.06}La_{0.34}B_6$ for $H \parallel [001]$ at $H = 0.1$ T. (c) Thermal expansion of $Ce_{0.6}Nd_{0.1}La_{0.3}B_6$ along the [001] direction at $H = 0$. The result of $Ce_{0.6}Nd_{0.4}B_6$ is also shown.

cusp could not be observed but a temperature dependence becomes weak below $T \sim 1.5$ K down to $T \sim 1.1$ K. These results strongly suggest that there is no phase IV in $Ce_{0.6}Nd_{0.06}La_{0.34}B_6$. Here, we note that the behavior of M of $Ce_{0.6}Nd_{0.06}La_{0.34}B_6$ is quite similar to that of $Ce_xNd_{1-x}B_6$ ($0.7 \leq x \leq 0.8$) in phase V. Here, phase V is the incommensurate AF order. Since the peak of C of $Ce_xNd_{1-x}B_6$ originating from the V-III transition is very sharp, the results of C of $Ce_{0.6}Nd_{0.06}La_{0.34}B_6$ are consistent with the presumption that the sharp peak at $T \sim 0.85$ K is due to the V-III transition.

In Fig. 5.25 (c), we show the thermal expansion of $Ce_{0.6}Nd_{0.1}La_{0.3}B_6$ along the [001] direction at $H = 0$. A shrinkage of the [001] direction is observed below $T \sim 2.0$ K, which is similar to that of $Ce_{0.6}Nd_{0.4}B_6$ below the I-V transition temperature, as shown in Fig. 5.25 (c). This result of $\Delta l/l$ contradicts the result of $Ce_{0.7}La_{0.3}B_6$ where the elongation of the [001] direction is observed below T_{IV-I} [57].

Thus, we conclude that phase IV suddenly disappears and phase V appears by Nd 6% doping.

5.3.2 $Ce_{0.6}Nd_{0.05}La_{0.35}B_6$

Figure 5.26 shows the T dependence of C of $Ce_{0.6}Nd_{0.05}La_{0.35}B_6$ under various magnetic fields for $H \parallel [001]$. As shown in Fig. 5.25, C at $H = 0$ shows a peak at $T \sim 1.1$ K, which corresponds to the I-IV transition. The peak temperature of C is slightly higher than $T_{IV-I} \sim 0.9$ K of $Ce_{0.6}La_{0.4}B_6$. This peak is also observed up to $H = 0.8$ T. At $H = 1.2$ T, two peaks are observed at $T \sim 1.1$ K and ~ 0.8 K, which correspond to the I-IV and IV-III transition, respectively. In magnetic fields between $H = 1.5$ T and 2.0 T, C shows a sharp peak originating from the phase transition to phase III. With increasing H up to $H = 3.5$ T, T_Q and T_N are recognized at $T \sim 2.0$ K and ~ 1.05 K, respectively. At $H = 6.0$ T, a large peak is observed at $T \sim 2.9$ K, which corresponds to the I-II transition.

Figures 5.27 and 5.28 show the T and H dependence of ρ of $Ce_{0.6}Nd_{0.05}La_{0.35}B_6$ for $H \parallel [001]$, respectively. The overall features of $\rho-T$ curve below $H \sim 1.0$ T are similar to those of $Ce_{0.6}La_{0.4}B_6$. [50]Since it is difficult to find the I-IV transition from the $\rho-T$ curve, we determine the transition temperatures at low magnetic fields

by using the result of C. In the low magnetic fields, the $\rho-H$ curve shows the H independent and has a large hysteresis below $T = 1.0$ K, which indicates the existence of phase IV at low magnetic fields. Above $T = 1.3$ K, the $\rho-H$ curve also shows the small H independence at low magnetic fields and a steep decrease around 2.0 T, although a hysteresis could not be observed in the $\rho-H$ curve. This result indicates that the steep decrease of ρ above $T = 1.3$ K originates from the I-II transition.
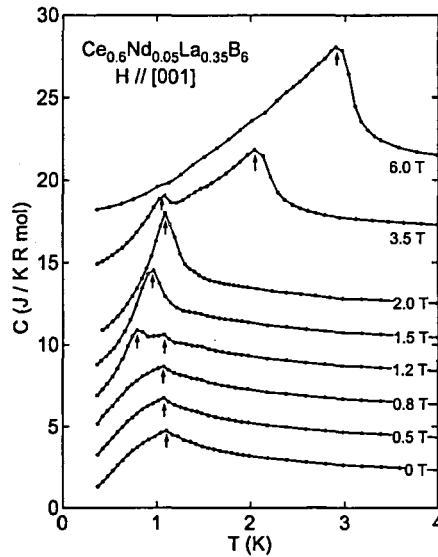
Fig. 5.26   Temperature dependence of the specific heat of $Ce_{0.6}Nd_{0.05}La_{0.35}B_6$ under various magnetic fields for $H \parallel$ [001]. The origin of the vertical axis of each curve in magnetic fields is shifted so as to see it easily.
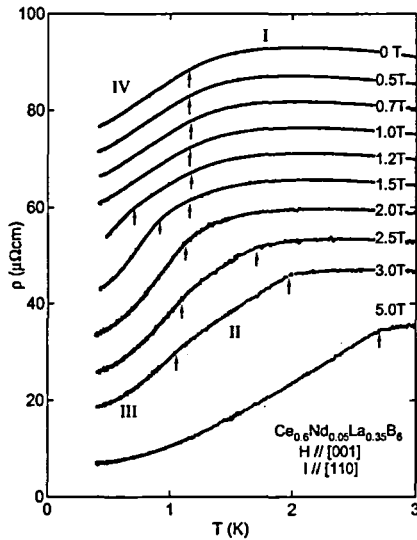
Fig. 5.27   Temperature dependence of the electrical resistivity of $Ce_{0.6}Nd_{0.05}La_{0.35}B_6$ for $H \parallel$ [001].
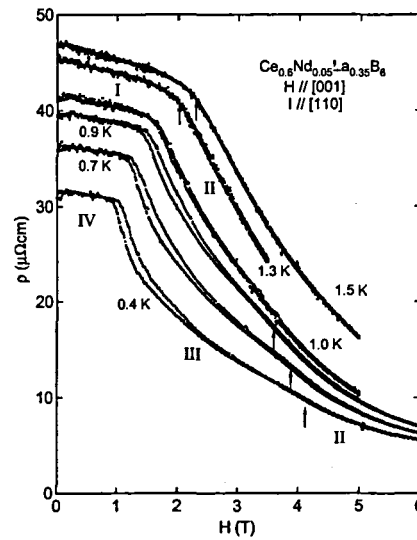
Fig. 5.28   Magnetic field dependence of the electrical resistivity of $Ce_{0.6}Nd_{0.05}La_{0.35}B_6$ for $H \parallel$ [001].
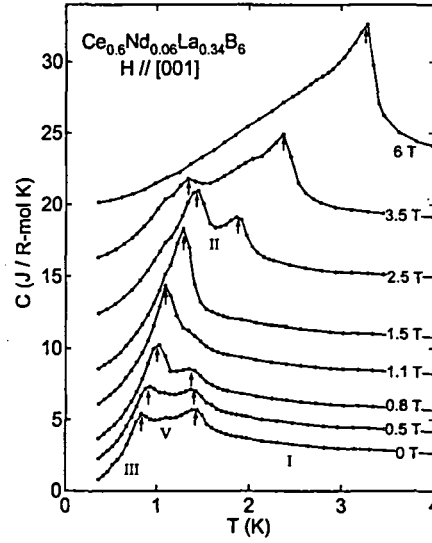
Fig. 5.29   Temperature dependence of the specific heat of $Ce_{0.6}Nd_{0.06}La_{0.34}B_6$ under various magnetic fields for $H \parallel$ [001]. The origin of the vertical axis of each curve in magnetic fields is shifted so as to see it easily.
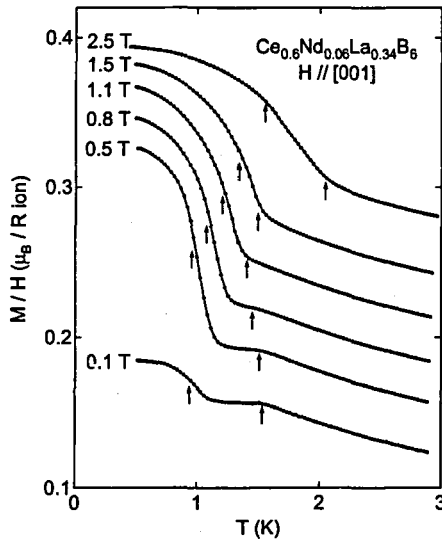
Fig. 5.30   Temperature dependence of the magnetization of $Ce_{0.6}Nd_{0.06}La_{0.34}B_6$ in the form of M/H for $H \parallel$ [001]. The origin of the vertical axis of each curve in magnetic fields is shifted so as to see it easily.
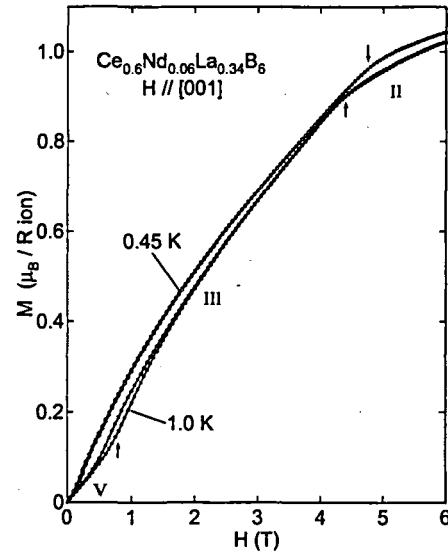
Fig. 5.31   Magnetization curve of $Ce_{0.6}Nd_{0.06}La_{0.34}B_6$ for $H \parallel$ [001].

5.3.3 $Ce_{0.6}Nd_{0.06}La_{0.34}B_6$

Figure 5.29 shows the T dependence of C of $Ce_{0.6}Nd_{0.06}La_{0.34}B_6$ under various magnetic fields for $H \parallel$ [001]. At $H = 0$, two peaks are observed at $T \sim 1.4$ K and ~ 0.8 K as shown in Fig. 5.25 (a) . These peaks are correspond to the I-V and the V-III transition, respectively. With increasing H up to 0.8 T, the peak at T_{V-III} shifts to higher temperatures and becomes sharper while the peak at T_{V-I} slightly shifts to lower temperatures.
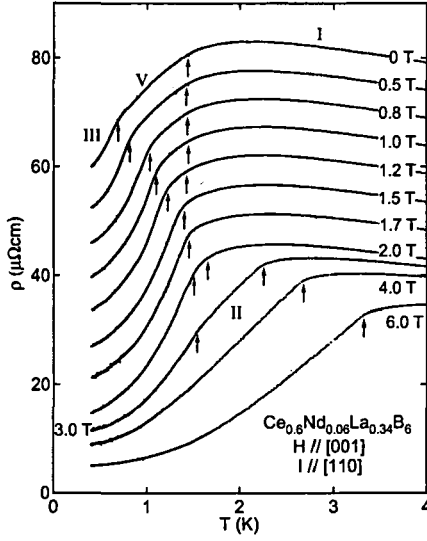
Fig. 5.32 Temperature dependence of the electrical resistivity of $Ce_{0.6}Nd_{0.06}La_{0.34}B_6$ for $H \parallel [001]$.
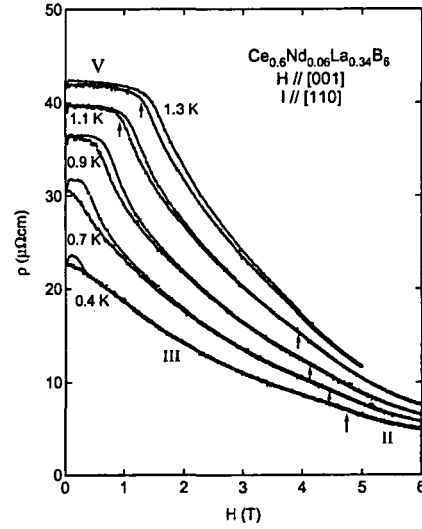
Fig. 5.33 Magnetic fi eld dependence of the electrical resistivity of $Ce_{0.6}Nd_{0.06}La_{0.34}B_6$ for $H \parallel [001]$.

In magnetic fields between $H = 1.1$ T and 1.5 T, C shows a sharp and large peak, which originates from the phase transition to phase III. With further increasing H, C exhibits two peaks at $H = 2.5$ T and 3.5 T, which correspond to T_Q and T_N, respectively. T_Q is also observed at $H = 6.0$ T and $T \sim 3.3$ K. This peak temperature is slightly higher than that for $y = 0.05$ at $H = 6.0$ T.

Figure 5.30 shows the T dependence of M of $Ce_{0.6}Nd_{0.06}La_{0.34}B_6$ in the form of M/H for $H \parallel [001]$. At $H = 0.1$ T, a small H dependence is observed between $T \sim 1.4$ K and ~ 1.0 K, which originates form the V-III transition as shown in Fig. 5.25 (b). This small H dependence of M is barely recognized up to $H \sim 0.8$ T. At $H = 1.1$ T, M shows a rapid increase at $T \sim 1.35$ K with decreasing T, which means that the system enters into phase III below $T \sim 1.35$ K. Above $H = 1.5$ T, T_Q and T_N are recognized .

Figure 5.31 shows the $M-H$ curve of $Ce_{0.6}Nd_{0.06}La_{0.34}B_6$ for $H \parallel [001]$. At $T = 0.45$ K, a convex curvature is observed in phase III and the III-II transition is recognized at $H_c^{III-II} \sim 4.75$ T. At $T = 1.0$ K, M shows a increase linear to H below $H \sim 0.55$ T and a rapid increase with a small hysteresis above $H \sim 0.55$ T. This anomaly of M is due to the V-III transition. With increasing H, M at $T = 1.0$ K shows a convex curvature and a kink at $H_c^{III-II} \sim 4.4$ T.

Figure 5.32 shows the T dependence of ρ of $Ce_{0.6}Nd_{0.06}La_{0.34}B_6$ for $H \parallel [001]$. At $H = 0$, ρ shows a linear decrease with decreasing T below $T_{V-I} \sim 1.4$ K and a rapid decrease at $T_{V-III} \sim 0.75$ K. With increasing H, the anomaly at T_{V-I} slightly shifts to lower temperatures and that at T_{V-III} shifts to higher temperatures. At $H = 1.5$ T, these anomalies appear to coincide with each other at $T \sim 1.4$ K where ρ exhibits a steep decrease. With further increase of H, the anomalies at T_Q and T_N are recognized at $H = 2.0$ T and 3.0 T. Above $H = 4.0$ T, the anomaly at T_N is difficult to see but that at T_Q is clearly observed.

Figure 5.33 shows the H dependence of ρ of $Ce_{0.6}Nd_{0.06}La_{0.34}B_6$ for $H \parallel [001]$. Above $T = 0.9$ K, a small H dependence is observed at low magnetic fields. Although these behaviors of ρ are associated with the existence of phase IV, the $\rho-H$ curve in phase V of $Ce_xNd_{1-x}B_6$ also shows a small H dependence [43]. Thus, we consider that the small H dependence in the present sample originates from the existence of phase V at low magnetic fields. With increasing H, after showing the small H dependence, ρ shows a steep decrease accompanied with a large hysteresis, which originates from the V-III transition. At $T = 0.4$ K, there exists the anomaly at low magnetic fields, which is probably due to the domain redistribution. Below $T = 1.1$ K, H_c^{III-II} is barely recognized.
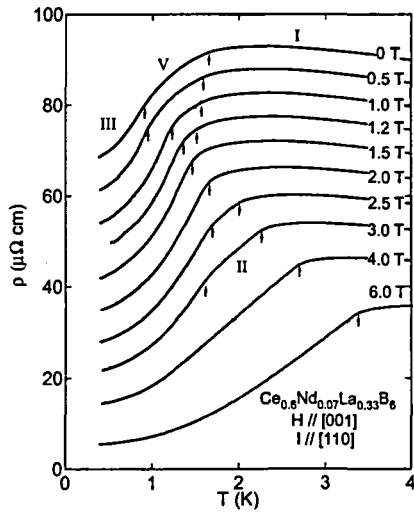
Fig. 5.34 Temperature dependence of the electrical resistivity of $Ce_{0.6}Nd_{0.07}La_{0.33}B_6$ for $H \parallel [001]$.
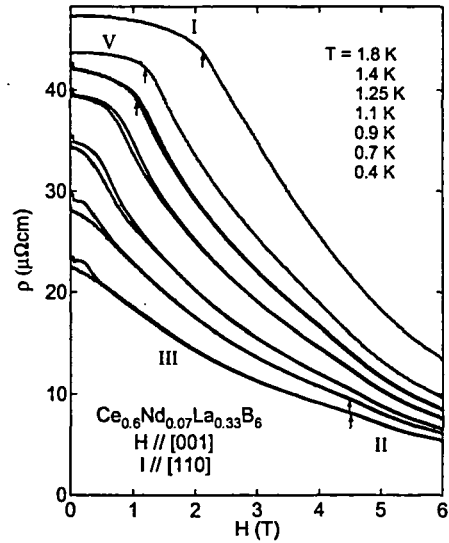
Fig. 5.35 Magnetic field dependence of the electrical resistivity of $Ce_{0.6}Nd_{0.07}La_{0.33}B_6$ for $H \parallel [001]$.
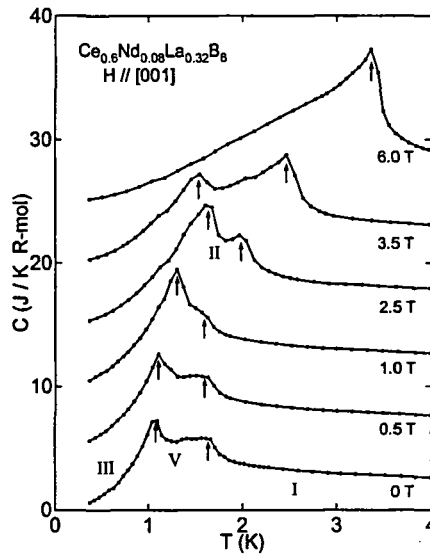
Fig. 5.36 Temperature dependence of the specific heat of $Ce_{0.6}Nd_{0.08}La_{0.32}B_6$ under various magnetic fields for $H \parallel [001]$. The origin of the vertical axis of each curve in magnetic fields is shifted so as to see it easily.

5.3.4 $Ce_{0.6}Nd_{0.07}La_{0.33}B_6$

Figures 5.34 and 5.35 show the T and H dependence of ρ of $Ce_{0.6}Nd_{0.07}La_{0.33}B_6$ for $H \parallel [001]$, respectively. The overall features of the $\rho-T$ and $\rho-H$ curve are quite similar to those for $y = 0.06$. Below $H = 1.2$ T, two anomalies are observed in the $\rho-T$ curve, which correspond to T_{V-I} and T_{V-III}, respectively. These two transition temperatures are higher than those for $y = 0.06$. In the $\rho-H$ curve, a small H dependence is observed at low magnetic fields between $T = 1.1$ K and 1.4 K. The decreasing rate of ρ in phase V is higher than that for $y = 0.06$. At $T = 0.4$ K, H_c^{III-II} is barely recognized at $H \sim 4.5$ T.
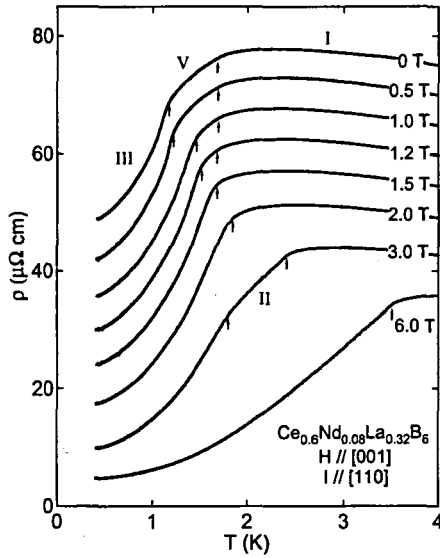
Fig. 5.37 Temperature dependence of the electrical resistivity of Ce$_{0.6}$Nd$_{0.08}$La$_{0.32}$B$_6$ for $H \parallel [001]$.
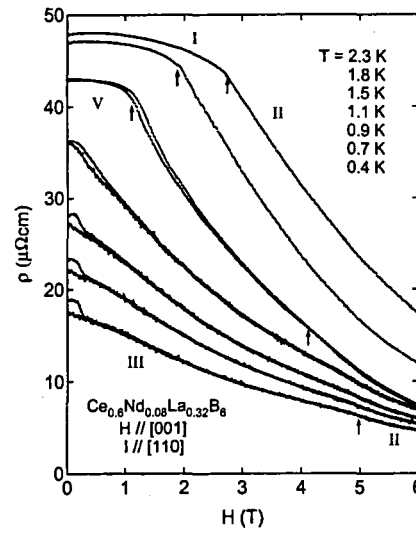
Fig. 5.38 Magnetic field dependence of the electrical resistivity of Ce$_{0.6}$Nd$_{0.08}$La$_{0.32}$B$_6$ for $H \parallel [001]$.

5.3.5 Ce$_{0.6}$Nd$_{0.08}$La$_{0.32}$B$_6$

Figure 5.36 shows the T dependence of C of Ce$_{0.6}$Nd$_{0.08}$La$_{0.32}$B$_6$ under various magnetic fields for $H \parallel [001]$. At $H = 0$, two peaks are observed at $T_{V-I} \sim 1.65$ K and $T_{V-III} \sim 1.0$ K. With increasing H up to $H = 1.0$ T, while the peak at T_{V-I} slightly shifts to lower temperatures, the peak at T_{V-III} shifts to higher temperatures and becomes sharper as well as the result of C for $y = 0.06$. At $H = 2.5$ T, C shows two peaks at $T_Q \sim 2.0$ K and $T_N \sim 1.6$ K. These transition temperatures are also recognized at $H = 3.5$ T. At $H = 6.0$ T, a peak is observed at $T_Q \sim 3.35$ K, which is slightly higher than that for $y = 0.06$.

Figure 5.37 and 5.38 show the T and H dependence of ρ of Ce$_{0.6}$Nd$_{0.08}$La$_{0.32}$B$_6$ for $H \parallel [001]$. At $H = 0$, the $\rho-T$ curve shows a kink at $T_{V-I} \sim 1.65$ K and a rapid decrease at $T_{V-III} \sim 1.1$ K. These anomalies are also observed up to $H = 1.2$ T. In the $\rho-H$ curve, ρ shows a decrease with increasing H below $T = 1.1$ K and $T = 1.5$ K, ρ shows a small H dependence below $H_c^{V-III} \sim 1.2$ K.

5.3.6 Ce$_{0.6}$Nd$_{0.1}$La$_{0.3}$B$_6$

Figure 5.39 shows the T dependence of M of Ce$_{0.6}$Nd$_{0.1}$La$_{0.3}$B$_6$ in the form of M/H for $H \parallel [001]$. At $H = 0.1$ T, M is independent of temperature below $T_{V-I} \sim 2.0$ K, which is also observed for $y = 0.06$. At $H = 0.5$ T, after showing a small temperature independence, M shows an increase below $T \sim 1.5$ K with decreasing temperature, which indicates the sign of the entrance into phase III. This increase of M is clearly observed at $H = 1.0$ T. With increasing H up to 1.5 T, the kink originating from the I-V transition disappears and a steep increase is observed at $T \sim 1.5$ K. At $H = 4.0$ T, M shows a kink at $T_Q \sim 2.8$ K. The kink at T_Q is also observed at $H = 6.0$ T. On the other hand, it is difficult to see the II-III transition above $H = 4.0$ T.

Figure 5.40 shows the $M-H$ curve of Ce$_{0.6}$Nd$_{0.1}$La$_{0.3}$B$_6$ for $H \parallel [001]$. At $T = 1.4$ K, two anomalies are observed at $H_c^{V-III} \sim 0.75$ T and $H_c^{III-II} \sim 4.7$ T. The $M-H$ curve at $T = 1.7$ K also shows an anomaly at $H \sim 1.8$ T. With increasing temperature up to $T = 2.2$ K, the I-II transition is recognized at $H_c^{I-II} \sim 2.7$ T.

Figure 5.41 and 5.42 show the T and H dependence of ρ of Ce$_{0.6}$Nd$_{0.1}$La$_{0.3}$B$_6$ for $H \parallel [001]$. At $H = 0$, the $\rho-T$ curve shows a kink at $T_{V-I} \sim 2.0$ K. With increasing H up to 1.5 T, the kink at T_{V-I} slightly shifts to higher temperatures. At $H = 1.0$ T, the $\rho-T$ curve exhibits a rapid decrease at $T_{V-III} \sim 1.5$ K. This rapid
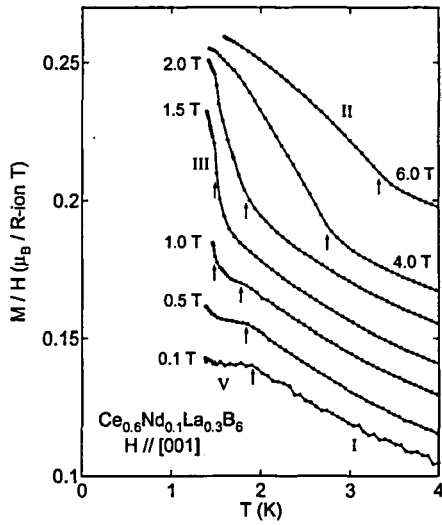
Fig. 5.39 Temperature dependence of the magnetization of $Ce_{0.6}Nd_{0.1}La_{0.3}B_6$ in the form of M/H for $H \parallel$ [001]. The origin of the vertical axis of each curve in magnetic fields is shifted so as to see it easily.
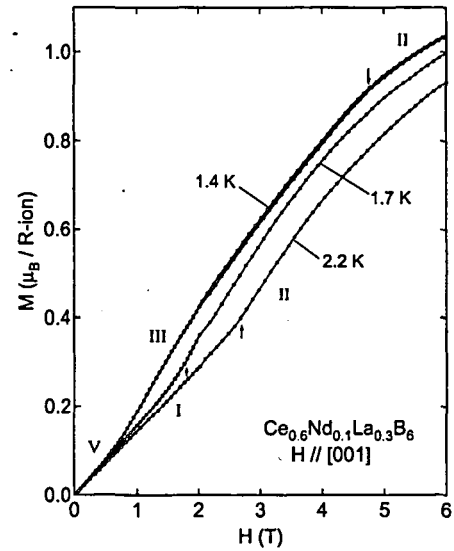
Fig. 5.40 Magnetization curve of $Ce_{0.6}Nd_{0.1}La_{0.3}B_6$ for $H \parallel$ [001].
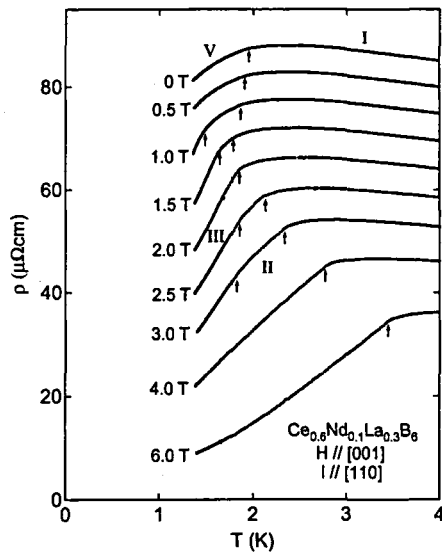
Fig. 5.41 Temperature dependence of the electrical resistivity of $Ce_{0.6}Nd_{0.1}La_{0.3}B_6$ for $H \parallel$ [001].
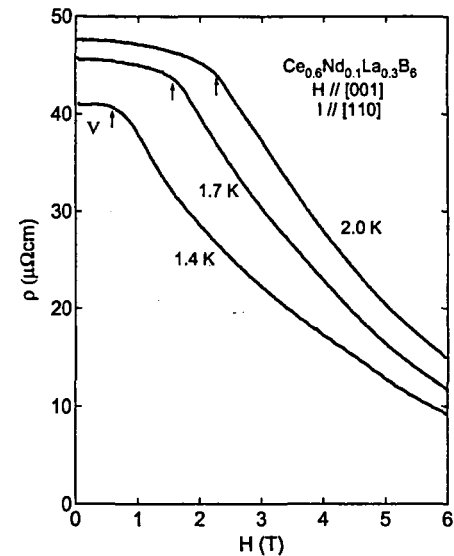
Fig. 5.42 Magnetic fi eld dependence of the electrical resistivity of $Ce_{0.6}Nd_{0.1}La_{0.3}B_6$ for $H \parallel$ [001].

decrease at T_{V-III} is also observed at $H = 1.5$ T. In magnetic fields between 2.5 T and 3.0 T, two anomalies are observed in the $\rho-T$ curve at T_Q and T_N. The anomaly at T_Q is also recognized at $H = 4.0$ T and 6.0 T. In all the $\rho-H$ curves, a small H dependence is observed at low magnetic fields. The anomaly at H_c^{III-II} could not be recognized in the present experiment.

5.3.7 Magnetic phase diagram of Ce$_{0.6}$Nd$_y$La$_{0.4-y}$B$_6$

Figure 5.43 shows the magnetic phase diagrams of Ce$_{0.6}$Nd$_y$La$_{0.4-y}$B$_6$ ($y = 0$, 0.05, 0.06, 0.07, 0.08 and 0.1) for $H \parallel [001]$ obtained from the present results. For $y = 0.05$, although the magnetic phase diagram is similar to that for $y = 0$, there are some difference between $y = 0$ and $y = 0.05$. The region of phase III expands, while that of phase IV is narrows and slightly shifts to higher temperatures. On the other hand, T_Q at finite magnetic fields is not varied so much by Nd doping. With increasing the Nd concentration from $y = 0.05$ to $y = 0.06$, a remarkable change appears in the low magnetic region. Phase IV suddenly disappears and phase V newly appears at low temperatures and low magnetic fields between phase I and III. Phase III further expands in comparison with that of $y = 0.05$. T_Q at finite magnetic fields is slightly enhanced by Nd 6% doping. With further increase of y up to 0.1, phase III is further stabilized and the region of phase V slightly shifts to higher temperatures.
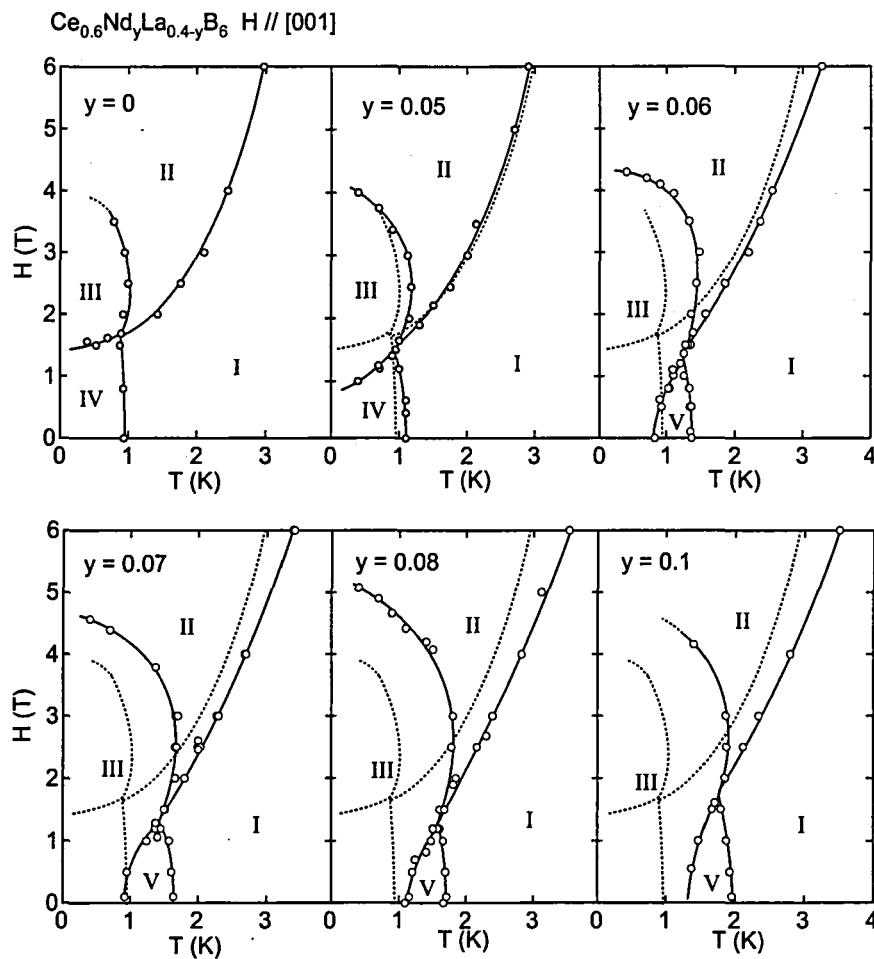
Fig. 5.43 Magnetic phase diagram of Ce$_{0.6}$Nd$_y$La$_{0.4-y}$B$_6$ ($y = 0$, 0.05, 0.06, 0.07, 0.08 and 0.1) for $H \parallel [001]$. The phase boundaries of $y = 0$ are also shown by the dashed lines.

5.4 $Ce_{0.5}R_yLa_{0.5-y}B_6$ $(x = 0.5)$

5.4.1 $Ce_{0.5}Nd_{0.1}La_{0.4}B_6$

Figure 5.44 shows the T dependence of C of $Ce_{0.5}Nd_{0.1}La_{0.4}B_6$ in magnetic fields along the [001] direction. The result of $Ce_{0.5}La_{0.5}B_6$ at $H = 0$ is also shown. A broad peak is seen at $T \sim 0.8$ K in $Ce_{0.5}La_{0.5}B_6$, which clearly indicates the existence of the LRO below $T \sim 0.8$ K. The present result of a rapid decrease of C below ~ 0.8 K is very different from the result of $Ce_{0.25}La_{0.75}B_6$. In $Ce_{0.25}La_{0.75}B_6$, C shows very broad maximum at ~ 1 K [73] but does not show a rapid decrease as is observed in $Ce_{0.5}La_{0.5}B_6$. In this compound, a peak of χ is seen at $T \sim 0.7$ K [74], not a small softening of C_{44} below $T \sim 1.0$ K [75] which has never observed in $Ce_{0.25}La_{0.75}B_6$ and a small magnetoresistance below $T \sim 0.8$ K. From these results, we conclude that phase IV is realized below $T_{IV-I} \sim 0.8$ K in $Ce_{0.5}La_{0.5}B_6$. In $Ce_{0.5}Nd_{0.1}La_{0.4}B_6$, a very sharp peak is seen at $T \sim 1.2$ K in place of a broad maximum in $Ce_{0.5}La_{0.5}B_6$. The origin of the maximum or peak of C in these two samples is considered to be the same by considering that the peak temperature increases continuously with increasing R-doping in $Ce_{0.4}(Nd_yLa_{1-y})_{0.6}B_6$ and $Ce_{0.5}(Pr_yLa_{1-y})_{0.5}B_6$ which will be shown later. Furthermore, the results of the magnetization and magnetoresistance which will be shown below also exhibit the characteristic properties in phase IV. Thus, we conclude that also in $Ce_{0.5}Nd_{0.1}La_{0.4}B_6$ phase IV is realized below $T_{IV-I} \sim 1.2$ K. $T_{IV-I} \sim 1.2$K is higher than $T_{IV-I} \sim 0.9$ K for $x = 0.6$ and nearly the same as $T_{IV-I} \sim 1.3$ K for $x = 0.65$. The fact that a peak at T_{IV-I} is sharp indicates that phase IV is well defined in the present sample. With increasing magnetic field up to 2 T, a sharp peak of C at $H = 0$ becomes broad and the peak temperature is reduced and above $H = 3.5$ T a peak of C is replaced by a sharp and large peak at T_Q. In magnetic fields between 2 T and 3.5 T, the III-II phase transition is recognized.

Figure 5.45 shows the T dependence of M of $Ce_{0.5}Nd_{0.1}La_{0.4}B_6$ in the form of M/H for $H \parallel [001]$. M/H at $H = 0.1$ T shows a peak at $T_{IV-I} \sim 1.3$ K. The peak temperature of the magnetic susceptibility in $Ce_{0.5}La_{0.5}B_6$ is ~ 0.7 K. With increasing magnetic field up to 2 T, a kink becomes broad and the kink temperature shifts to lower temperature down to $T \sim 1.1$ K and the anomaly at $T \sim 1.1$ K is sharper than that
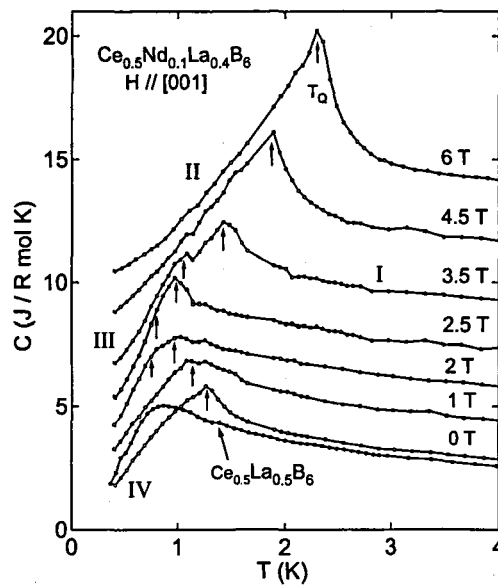
Fig. 5.44 Temperature dependence of the specific heat of $Ce_{0.5}Nd_{0.1}La_{0.4}B_6$ under various magnetic fields for $H \parallel [001]$. The origin of the vertical axis of each curve in magnetic fields is shifted so as to see it easily. The result of $Ce_{0.5}La_{0.5}B_6$ at $H = 0$ is also shown.
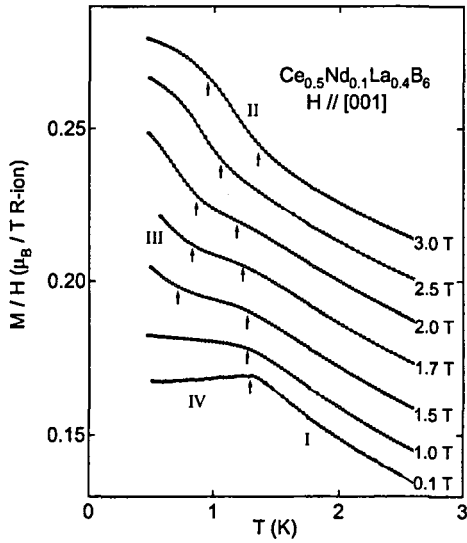
Fig. 5.45 Temperature dependence of the magnetization of $Ce_{0.5}Nd_{0.1}La_{0.4}B_6$ in the form of M/H for $H \parallel$ [001]. The origin of the vertical axis of each curve in magnetic fields is shifted so as to see it easily.
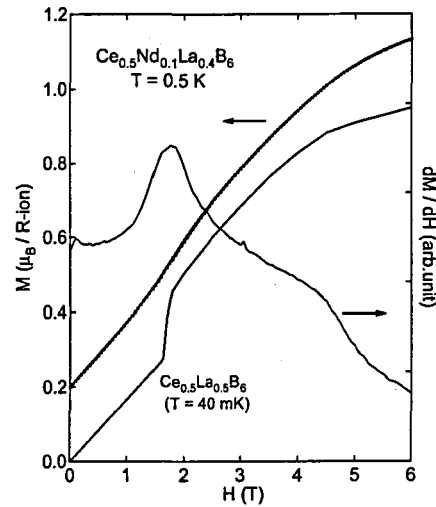
Fig. 5.46 Magnetization curve of $Ce_{0.5}Nd_{0.1}La_{0.4}B_6$ for $H \parallel$ [001]. $dM/dH - H$ of $Ce_{0.5}Nd_{0.1}La_{0.4}B_6$ and the magnetization curve of $Ce_{0.5}La_{0.5}B_6$ at $T = 40$ mK are also shown. The latter is cited from ref. O.
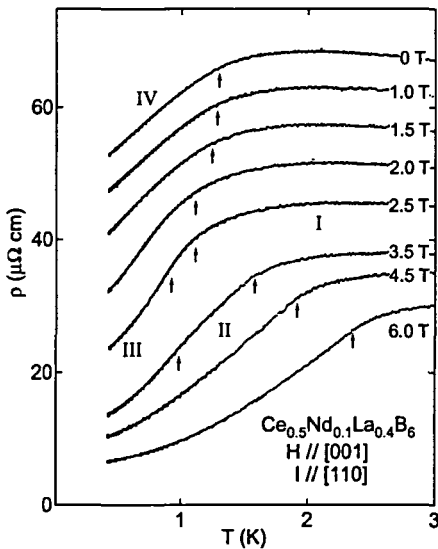
Fig. 5.47 Temperature dependence of the electrical resistivity of $Ce_{0.5}Nd_{0.1}La_{0.4}B_6$ for $H \parallel$ [001]. The origin of the vertical axis of the curves below $H = 2.5$ T is shifted so as to see it easily.
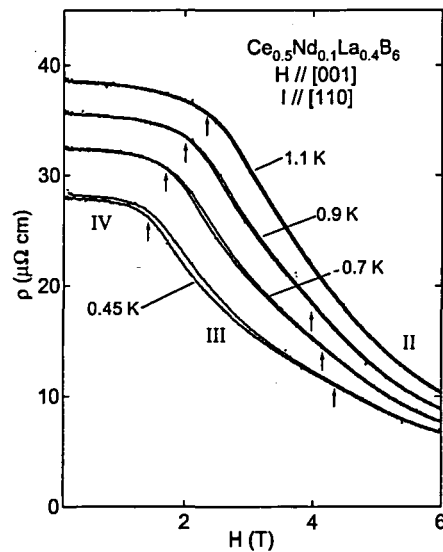
Fig. 5.48 Magnetic field dependence of the electrical resistivity of $Ce_{0.5}Nd_{0.1}La_{0.4}B_6$ for $H \parallel$ [001].

at T_{IV-I} in $Ce_{0.5}La_{0.5}B_6$ [53]. These observations are consistent with the results of C. Between $H = 1.5$ T and 2 T, two anomalies are seen in the $M/H - T$ curve. The anomaly at higher temperature corresponds to T_{IV-I} and that at lower temperature to the III-IV phase boundary. At $H = 2.5$ T, one anomaly is observed at $T = 1$ K and at $H = 3$ T, $T_N \sim 1$ K and $T_Q \sim 1.4$ K are recognized.

Figure 5.46 shows the $M - H$ and $dM/dT - H$ curves of $Ce_{0.5}Nd_{0.1}La_{0.4}B_6$ for $H \parallel$ [001]. That of $Ce_{0.5}La_{0.5}B_6$ at $T = 40$ mK is also shown [53]. The $M - H$ curve of $Ce_{0.5}Nd_{0.1}La_{0.4}B_6$ shows two anomalies
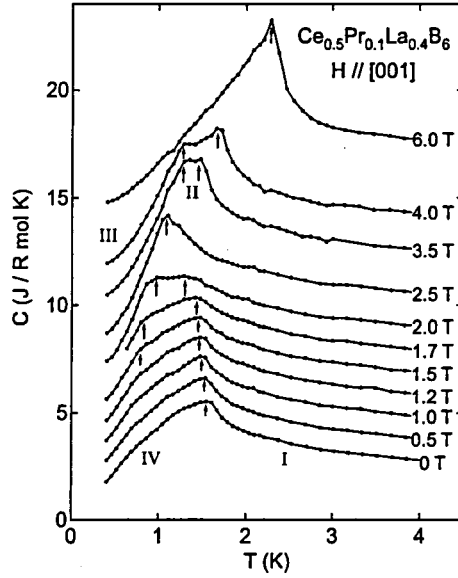
Fig. 5.49 Temperature dependence of the specific heat of $Ce_{0.5}Pr_{0.1}La_{0.4}B_6$ under various magnetic fields for $H \parallel [001]$. The origin of the vertical axis of each curve in magnetic fields is shifted so as to see it easily.
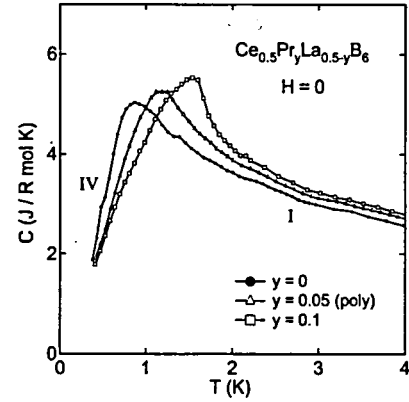
Fig. 5.50 Temperature dependence of the specific heat of $Ce_{0.5}Pr_{0.1}La_{0.4}B_6$ single crystal and $Ce_{0.5}Pr_{0.05}La_{0.45}B_6$ poly crystal at $H = 0$. The result of $Ce_{0.5}La_{0.5}B_6$ single crystal is also shown.

at $H_c^{IV-III} \sim 1.5$ T and $H_c^{III-II} \sim 4.5$ T , which are clearly seen in the $dM/dH - H$ curve. These behaviors are similar to those of $Ce_{0.5}La_{0.5}B_6$, although the anomalies at H_c^{IV-III} and H_c^{III-II} are much less clear.

Figures 5.47 and 5.48 show the T and H dependence of the electrical resistivity, ρ of $Ce_{0.5}Nd_{0.1}La_{0.4}B_6$ for $H \parallel [001]$, respectively. The arrows drawn in Fig. 5.47 indicate the transition temperatures obtained by the results of C and M. While T_Q is clearly recognized also in the $\rho - T$ curve, T_{IV-I} and T_N are difficult to recognize. In a low magnetic field region, ρ shows a small H-dependence, which is a characteristic property in phase IV. Below 0.9 K, H_c^{IV-III} and H_c^{III-II} are recognized in the magnetoresistance in Fig. 5.48.

5.4.2 $Ce_{0.5}Pr_{0.1}La_{0.4}B_6$

Figure 5.49 shows the T dependence of C of $Ce_{0.5}Pr_{0.1}La_{0.4}B_6$ under various magnetic fields for $H \parallel [001]$. The results at $H = 0$ of $Ce_{0.5}Pr_yLa_{0.5-y}B_6$ (y=0, 0.05, 0.1) is also shown in Fig. 5.50. In Fig. 5.50, it is clearly seen that the peak temperature continuously increases and a peak becomes sharper with increasing Pr doping as in the case of Nd doping. This means that phase IV is stabilized also by Pr doping. We note that T_{IV-I} of $Ce_{0.5}Pr_{0.1}La_{0.4}B_6$ is as high as ~ 1.6 K, which is about twice of $T_{IV-I} \sim 0.8$ K of $Ce_{0.5}La_{0.5}B_6$ and is much higher than $T_{IV-I} \sim 1.2$ K of $Ce_{0.5}Nd_{0.1}La_{0.4}B_6$. With increasing H up to 2.0 T, T_{IV-I} slightly shifts to lower temperatures, as shown in Fig. 5.49. In magnetic field between 1.7 T and 2.0 T, the kink of C originating from the IV-III transition is recognized at low temperatures. With further increase of H, the anomalies at T_Q and T_N are observed at $H = 3.5$ T and 4.0 T. At $H = 6.0$ T, a large peak is observed at $T_Q \sim 2.3$ K.

5.4.3 Magnetic phase diagram of $Ce_{0.5}R_{0.1}La_{0.4}B_6$

Figures 5.51 and 5.52 show the magnetic phase diagrams of $Ce_{0.5}R_{0.1}La_{0.4}B_6$ (R = Pr, Nd) for $H \parallel [001]$ obtained by the present results, respectively. The overall features of the magnetic phase diagrams are in principle the same as that of $Ce_{0.5}La_{0.5}B_6$. Judging from the similarity of the magnetic phase diagrams of the Nd doped and undoped samples, the order parameters in the LRO phases are the same in both systems even though 10% Nd ions are doped, which is different from the cases of $Ce_{0.7}Nd_yLa_{0.3-y}B_6$ and $Ce_{0.6}Nd_yLa_{0.4-y}B_6$ where the
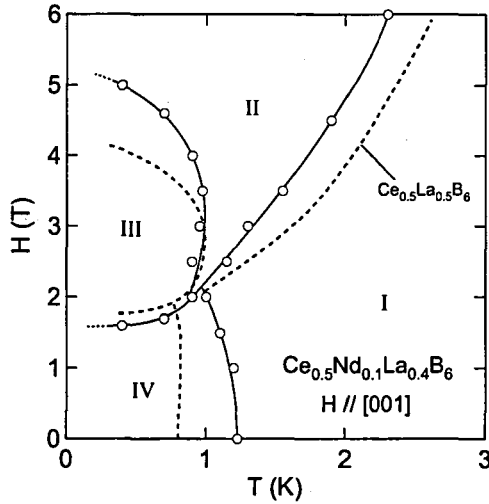
Fig. 5.51   Magnetic phase diagrams of $Ce_{0.5}Nd_{0.1}La_{0.4}B_6$ for $H \parallel [001]$. That for $Ce_{0.5}La_{0.5}B_6$ is also shown by the dashed lines.
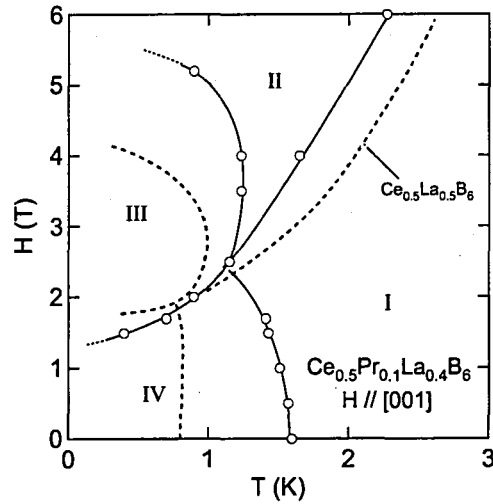
Fig. 5.52   Magnetic phase diagrams of $Ce_{0.5}Pr_{0.1}La_{0.4}B_6$ for $H \parallel [001]$. That for $Ce_{0.5}La_{0.5}B_6$ is also shown by the dashed lines.

ground state is changed from phase IV to III or to the other magnetic phase V by few percent of Nd ion doping. In both cases of Nd and Pr doping in $Ce_{0.5}La_{0.5}B_6$, both of T_{IV-I} and T_N are enhanced and T_Q at high magnetic fields is suppressed. The enhancement of T_{IV-I} and T_N is much larger in the Pr doping case than in the Nd doping one. The suppression of T_Q shows a similar tendency in both cases. The enhancement of T_{IV-I} seems to be correlated with that of T_N in both cases. The region of phase III in $Ce_{0.5}La_{0.5}B_6$ is expanded by both Pr and Nd doping. In $Ce_{0.4}La_{0.6}B_6$, T_{IV-I} is largely enhanced but T_Q at high magnetic fields is suppressed by Nd doping.

5.5 $Ce_{0.4}Nd_yLa_{0.6-y}B_6$ ($x = 0.4$)

5.5.1 $Ce_{0.4}Nd_{0.1}La_{0.5}B_6$

Figure 5.53 shows the T dependence of C of $Ce_{0.4}Nd_{0.1}La_{0.5}B_6$ in magnetic fields along the [001] direction. The results of $Ce_{0.4}La_{0.6}B_6$ single crystal and $Ce_{0.4}Nd_{0.05}La_{0.55}B_6$ polycrystal at $H = 0$ are also shown in Fig. 5.54. The T dependence of C of $Ce_{0.4}La_{0.4}B_6$ is similar to that of $Ce_{0.5}La_{0.5}B_6$ and a maximum temperature is $\sim$ 0.7 K. A kink is reported at $T \sim$ 0.5 K in the magnetic susceptibility of $Ce_{0.4}La_{0.6}B_6$ [74]. Thus, the ground state of $Ce_{0.4}La_{0.6}B_6$ is considered to be phase IV. The existence of phase III in finite magnetic fields is not recognized in the present specific heat measurement in $Ce_{0.4}La_{0.6}B_6$. With increasing Nd doping concentration, T_{IV-I} shifts to higher temperature and in $Ce_{0.4}Nd_{0.1}La_{0.5}B_6$, T_{IV-I} becomes as high as $\sim$ 1.1 K and a broad maximum of C in $Ce_{0.4}La_{0.6}B_6$ is replaced by a clear peak as in the case of Nd doping in $Ce_{0.5}La_{0.5}B_6$. As in the case of $Ce_{0.5}Nd_{0.1}La_{0.4}B_6$, with increasing magnetic field up to 3 T, T_{IV-I} shifts to lower temperature and a peak is changed to a broad maximum with increasing magnetic field up to 3 T. Above 4 T, a clear peak is observed at T_Q. In the present experiments, the existence of phase III was not recognized also in $Ce_{0.4}Nd_{0.1}La_{0.5}B_6$.

Figure 5.55 shows the T dependence of M of $Ce_{0.4}Nd_{0.1}La_{0.5}B_6$ in the form of M/H for $H \parallel [001]$. M/H at $H = 0.1$ T is independent of temperature below $T_{IV-I} \sim$ 1.2 K, which is also observed in phase IV of $Ce_{0.4}La_{0.6}B_6$ [74]. This temperature dependence of M becomes weak with increasing magnetic field up to 2.0 T. At $H = 3.0$ T, M exhibits a linear increase with decreasing T down to 0.5 K. Above $H = 4.0$ T, a kink at T_Q is barely recognized.
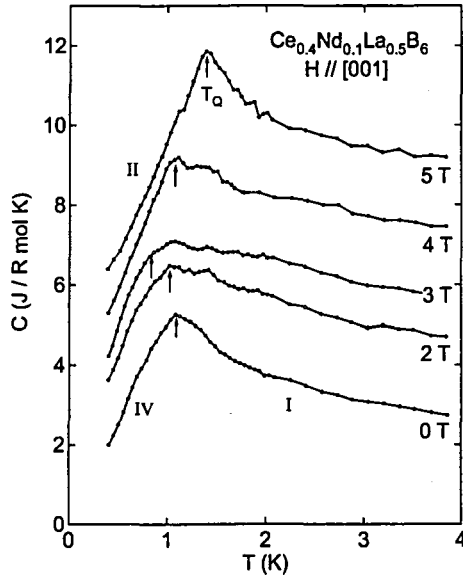
Fig. 5.53 Temperature dependence of the specific heat of $Ce_{0.4}Nd_{0.1}La_{0.5}B_6$ under various magnetic fields for $H \parallel [001]$. The origin of the vertical axis of each curve in magnetic fields is shifted so as to see it easily.

Fig. 5.54 Temperature dependence of the specific heat of $Ce_{0.4}Nd_{0.1}La_{0.5}B_6$ single crystal and $Ce_{0.4}Nd_{0.05}La_{0.55}B_6$ poly crystal at $H = 0$. The result of $Ce_{0.4}La_{0.6}B_6$ single crystal is also shown.

Fig. 5.55 Temperature dependence of the magnetization of $Ce_{0.4}Nd_{0.1}La_{0.5}B_6$ in the form of M/H for $H \parallel [001]$. The origin of the vertical axis of each curve in magnetic fields is shifted so as to see it easily.
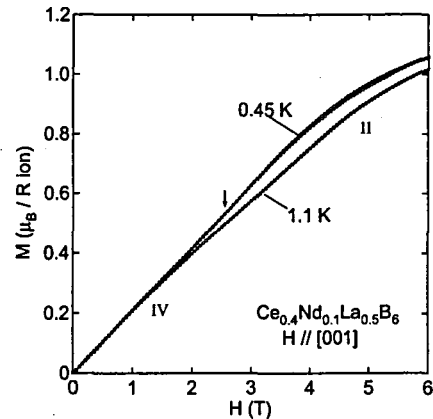
Fig. 5.56 Magnetization curve of $Ce_{0.4}Nd_{0.1}La_{0.4}B_6$ for $H \parallel [001]$.

Figure 5.56 shows the $M-H$ curve of $Ce_{0.4}Nd_{0.1}La_{0.5}B_6$ for $H \parallel [001]$. M at $T = 0.45$ K increases linearly with increasing H and shows a small kink at $H \sim 2.5$ T. This behavior of M is similar to that around the critical magnetic field from phase IV to II, H_c^{IV-II} of $Ce_{0.75}La_{0.25}B_6$ under the uniaxial pressure along the [001] direction, apart from the magnitude of the kink at H_c^{IV-II} [56]. Thus, the small kink at ~ 2.5 T should originate from the IV-II transition and phase III does not exist at the finite magnetic fields in the present sample.
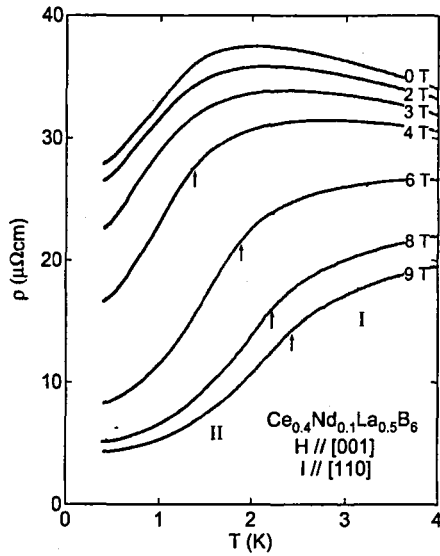
Fig. 5.57 Temperature dependence of the electrical resistivity of $Ce_{0.4}Nd_{0.1}La_{0.5}B_6$ for $H \parallel [001]$. The origin of the vertical axis of each curve in magnetic fi elds is shifted so as to see it easily.
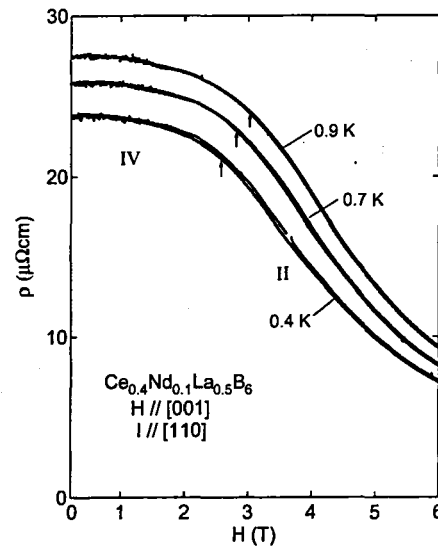
Fig. 5.58 Magnetic fi eld dependence of the electrical resistivity of $Ce_{0.4}Nd_{0.1}La_{0.5}B_6$ for $H \parallel [001]$.
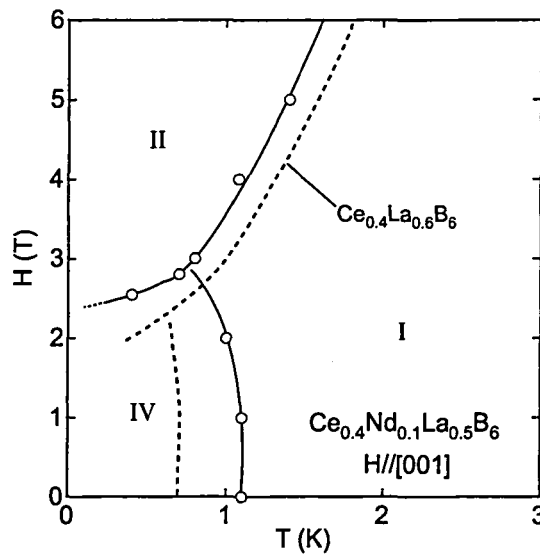
Fig. 5.59 Magnetic phase diagrams of $Ce_{0.4}Nd_{0.1}La_{0.5}B_6$ for $H \parallel [001]$. That for $Ce_{0.4}La_{0.6}B_6$ is also shown by the dashed lines.

Figures 5.57 and 5.58 show the T and H dependence of ρ of $Ce_{0.4}Nd_{0.1}La_{0.5}B_6$ for $H \parallel [001]$. Below 3.0 T, the ρ-T curve shows a broad maximum at $\sim$ 2.0 K and decreases smoothly with decreasing T as in the case of $Ce_{0.5}Nd_{0.1}La_{0.4}B_6$ at low magnetic fields . Thus, the sign of the phase transition could not be recognized in the ρ-T curve below 3.0 T. Above 4.0 T, an anomaly at T_Q is barely recognized. In the ρ-H curve, a small negative magnetoresistance is observed at low magnetic fields in all the temperature region. The arrows drawn in Fig. 5.58 mean the inflection points of the ρ-H curve which seem to correspond to the IV-II transition.

5.5.2   Magnetic phase diagram of $Ce_{0.4}Nd_{0.1}La_{0.5}B_6$

Figure5.59 shows the magnetic phase diagrams of $Ce_{0.4}Nd_{0.1}La_{0.5}B_6$ for $H \parallel [001]$ obtained by the present results. As in the case of $Ce_{0.5}R_{0.1}La_{0.4}B_6$, T_{IV-I} is largely enhanced but T_Q is suppressed by Nd doping. Before starting the experiments, we conjectured that the Nd doping may generates phase III in the finite magnetic fields because phase III becomes stabilized by Nd doping above $x = 0.5$. However, we could not recognize the existence of phase III in $Ce_{0.4}Nd_{0.1}La_{0.5}B_6$.

5.6   Nd concentration dependence

of the transition temperatures in $Ce_xNd_yLa_{1-x-y}B_6$

Figure 5.60 shows the y dependence of the transition temperatures of $Ce_xNd_yLa_{1-x-y}B_6$ ($x = 0.7, 0.65, 0.6$, 0.5 and 0.4). For $x = 0.7$, the Nd ion doping reduces the region of phase IV very rapidly. Phase IV seems to disappear at $y \sim 0.015 \sim 0.02$ above which only the AF magnetic state exists below T_N. The important result is that $T_N = 1.4$ K is the same as $T_{IV-I} = 1.4$ K independent of the y value at least up to $y = 0.05$. No discontinuity between T^{IV-I} and T_N is quite similar to that of $Ce_xLa_{1-x}B_6$ through $x \sim 0.8$. These seem to suggest the possible existence of some relation between the order parameters of phase IV and III. For $y = 0.1$, there exists phase V which exists in $Ce_xNd_{1-x}B_6$ ($x \geq 0.85$). Since T_N of $y = 0.1$ is ~ 1.7 K, T_N seems to be smoothly enhanced above $y \sim 0.05$. For $x = 0.65$, the overall features seem to be similar to those for $x = 0.7$. Phase IV seems to exist below $y \sim 0.35$. Considering the results for $x = 0.7$, we presume that phase V appears at $y \sim 0.08$. Here, it should be noted that phase IV becomes robust against Nd doping with decreasing x. For $x = 0.6$, phase IV still remains as the ground state up to $y = 0.05$. T_{IV-I} seems to slightly increase with increasing y. With increasing y, the IV-III phase boundary could not be observed, but phase V newly appears at the same time as phase IV suddenly disappears at $y \sim 0.06$. Namely, for $x = 0.6$, a discontinuous boundary exists at $y \sim 0.055$. With further increase of y, both T_{V-I}, and T_N are enhanced. For $x = 0.5$ and 0.4, the Nd doping effect is quite different from that for $x \geq 0.6$. The most important result is that T_{IV-I} is largely
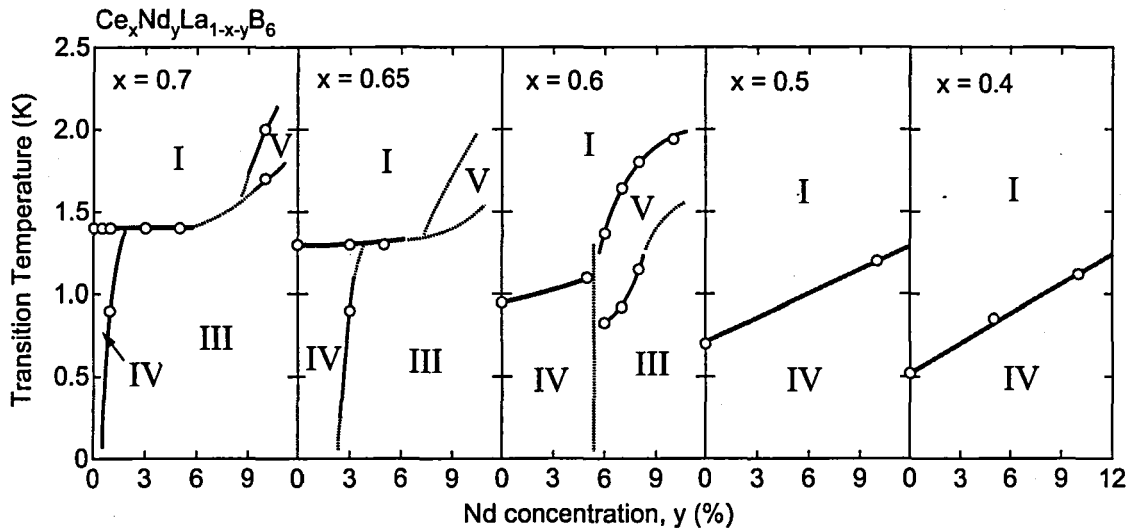
Fig. 5.60   Nd concentration (y) dependence of the transition temperatures of $Ce_xNd_yLa_{1-x-y}B_6$ ($x = 0.7, 0.65, 0.6, 0.5$ and 0.4). The dotted lines are the conjectured ones.

enhanced by the Nd doping, which could not be observed for $x \geq 0.6$. This result indicates that the Nd ions have a role to stabilize of phase IV for $x \leq 0.5$, and that the property of phase IV for $x \geq 0.6$ is different from that for $x \leq 0.5$.

Chapter 6

Discussion

In this chapter, we discuss the present experimental results of the R-ion doping effect on phase IV of $Ce_xLa_{1-x}B_6$. First, we discuss the effect of the Nd doping for the system with higher Ce concentraion, $x = 0.7$. Next, we discuss the origin of the enhancement of T_{IV-I} below $x = 0.5$.

6.1 The effect of the Nd doping for $Ce_xLa_{1-x}B_6$ for $x \geq 0.6$

As clearly observed from the largely y dependent magnetic phase diagrams, a small amount of Nd doping largely reduces the region of phase IV and stabilizes phase III. Only a small amount of Nd doping appears to be sufficient to suppress phase IV completely and make phase III the ground state. This implies that the free energies of phases IV and III are very close to each other in the present system of $Ce_{0.7}Nd_yLa_{0.3-y}B_6$ with a small y region. This is also supported by the appearance of phase (III + IV). In a very small y region, the effect of the Nd doping on phase IV appears to be small as far as we observe the magnetic phase diagram for $y = 0.005$. The temperature dependence of M in phase IV is similar to that of $Ce_{0.7}La_{0.3}B_6$. [?] This also indicates that the Nd ions do not affect the order in phase IV. On the other hand, as for the effect of the Nd doping on phase III, from the results of M and ρ in phase III, it is found that the effective FM interaction induced by the coexistence of the O_{xy}-AFQ and T_{xyz}-AFO interactions in phase III is reduced by the Nd doping. The suppression of this FM interaction appears to originate from the enhancement of the AF exchange interaction by the Nd doping.

The present results for $Ce_{0.7}Nd_yLa_{0.3-y}B_6$ indicate that there exists a critical concentration $y_c \sim 0.015$ above which the ground state is changed from phase IV to III. This is observed in Fig. 5.60. The existence of the critical concentration suggests that phase III in this sample is formed by connecting the locally reinforced AF magnetic state around the Nd ions in the entire region of the crystal. The fact that phases IV and III coexist at low magnetic fields initially after zero field cooling around $y \sim 0.01$ indicates that the free energies of these two phases are very close to each other. If we estimate the range of the reinforced AF state around the Nd ions from $y \sim 0.01$, one Nd ion is situated per $\sim 5 \times 5 \times 5$ sites, as shown in Fig. At $H = 0$, the reinforced AF magnetic (AFM) region around the Nd ions is barely connected and when the magnetic field is applied, by the aid of the effective FM interaction induced by the magnetic field, the AFM state is easily stabilized in the entire region of the crystal. As for the temperature dependence of the region of phases IV and III for $y = 0.01$, the following factors are considered. The region of the AFM state around the Nd ions, which is the largest at $T = 0$, shrinks with increasing temperature as a result of the reduction in the AFM moment and the first-order phase transition from III to IV occurs at 0.8 K. In phase IV, the Nd ions are considered to behave as paramagnetic ions. In the sample with $y = 0.005$, the ground state is phase IV. If the Nd ions are paramagnetic in phase IV, the Curie-like behavior is expected to be observed at very low temperatures. This should be examined in the future to clarify the electronic state around the Nd ions in phase IV in $Ce_{0.7}Nd_{0.005}La_{0.295}B_6$.

Next, we discuss the competition between the O_{xy}-AFQ interaction and that for realizing phase IV. For $y = 0.03$, there exists only one phase III below 1.4 K and the enhancement of M is observed in this phase. This indicates the existence of the effective FM interaction induced by the coexistence of the O_{xy}-AFQ and

$$y \sim 0.005 \qquad\qquad\qquad y = 0.01$$

phase IV   phase III $5 \times 5 \times 5$ sites
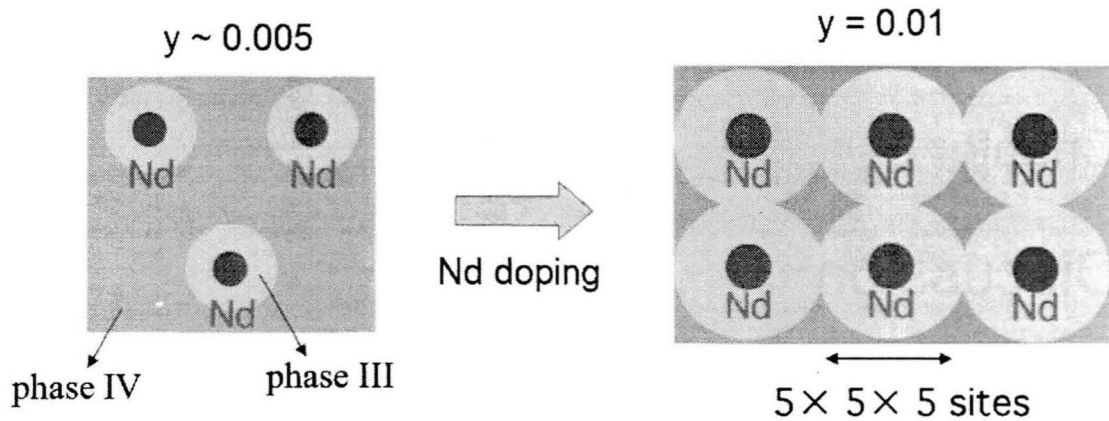
Fig. 6.1   Schematic picture of the coexistent phase of phase IV and III in $Ce_{0.7}Nd_yLa_{0.3-y}B_6$ with a small y region.

T_{xyz}-AFO interactions, which is also predicted from the magnetic phase diagram where phases II and III are connected by the second-order phase transition. Thus, the O_{xy}-AFQ interaction is expected to exist from a zero magnetic field, even though it appears by the aid of the AFM ordering in phase III. That is, in $Ce_{0.7}La_{0.3}B_6$, the O_{xy}-AFQ and T_{xyz}-AFO interactions are comparable to the interaction in phase IV even at $H = 0$. If the order parameter in phase IV is the Γ_{5u}-type AFO moment, the O_{xy}-AFQ interaction should suppress the O_{xy}-FQ moment accompanied by the Γ_{5u}-type AFO moment, and the magnetic susceptibility in phase IV is expected to be modified. However, such a behavior is not observed in the present experiments. On the other hand, microscopic measurements such as the resonant X-ray [63] and neutron diffractions [61] support the Γ_{5u}-type AFO order in phase IV. The origin of the nonexistence of the competition between the O_{xy}-AFQ interaction and the interaction in phase IV should be clarified to understand the overall features of $Ce_xLa_{1-x}B_6$.

6.2   The origin of the enhancement of T_{IV-I} for $x \leq 0.5$

Next, we discuss the present unexpected results for $x \leq 0.5$. The most important result of the present experiments is the drastic enhancement of T_{IV-I} by Pr and Nd doping in $Ce_{0.4}La_{0.6}B_6$ and $Ce_{0.5}La_{0.5}B_6$. As the origin of the enhancement of T_{IV-I}, we consider the following three cases. (1) The chemical pressure effect in the alloy systems. (2) The octupole moment of the Nd ion. (3) The variation of the order parameter due to the R-ion doping.

(1) The chemical pressure effect in the alloy systems

As shown in Fig. 6.2, T_{IV-I} of $Ce_{0.75}La_{0.25}B_6$ is slightly enhanced by applying pressure up to $P \sim 1$ GPa [76]. Then, we should check if the chemical pressure effect by R doping is the possible origin of the enhancement of T_{IV-I} or not. The ionic radius of Pr and Nd is smaller than that of Ce and La. Then, the chemical pressure effect by Pr or Nd doping is expected. The ionic radius of Pr is larger than that of Nd. Then, the chemical pressure effect is expected to be larger by Nd doping than by Pr doping. This contradicts the experimental results. Thus, the chemical pressure effect as the origin of the enhancement of T_{IV-I} is ruled out.

(2) The octupole moment of the Nd ion

Next, we consider the nature of the crystalline electric field (CEF) ground state of Pr and Nd ions in the present systems. The CEF ground state is the $\Gamma_8^{(2)}$ quartet and the Γ_5 triplet in NdB_6 and PrB_6, respectively [36]. In the present alloy systems, the CEF ground states of Nd and Pr ions in the present systems may not be different so much from those of NdB_6 and PrB_6, respectively. In the case of Nd ion, as there exists the dipole, quadrupole
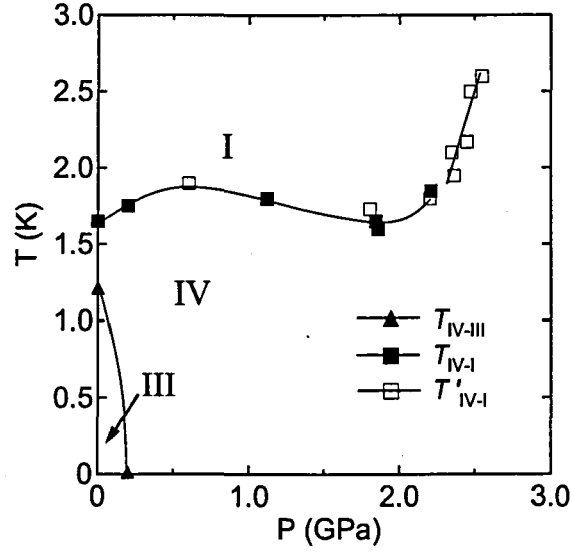
Fig. 6.2 Pressure dependence of the transition temperatures of $Ce_{0.75}La_{0.25}B_6$ [76].

and octupole moments, the octupole moment of Nd ion could contribute to the enhancement of T_{IV-I}. On the other hand, in the case of Pr ion, the octupole moment does not exist. By considering that the enhancement of T_{IV-I} appears in both doped systems, the contribution of the octupole moment of Nd ion as the origin of the enhancement of T_{IV-I} is ruled out. T_Q in finite magnetic fields is reduced by Nd and Pr doping in the same way as is seen in Fig. 5.51 and 5.52. This indicates that the quadrupole moment of Nd or Pr ion also does not contribute to the enhancement of T_{IV-I}. Thus, we conclude that the expansion of the regions of phases III and IV by Nd and Pr doping originates from the contribution of the dipole moment of Nd or Pr ion. If phase IV of $Ce_{0.5}La_{0.5}B_6$ and $Ce_{0.4}La_{0.6}B_6$ is Γ_{5u}-type AFO order as is proposed in phase IV of $Ce_{0.7}La_{0.3}B_6$ [65], the ground state is a nonmagnetic singlet. In this case, the dipole magnetic moment of Nd and Pr ion cannot couple with the Γ_{5u}-type octupole moment and does not enhance T_{IV-I}.

(3) The variation of the order parameter due to the R-ion doping

The Γ_{5u}-type AFO order parameter in phase IV proposed by Kubo and Kuramoto is the linear combination of $T_x^\beta + T_y^\beta + T_z^\beta/\sqrt{3}$. This type of the linear combination is favorable because it has the largest eigenvalue among the other linear combination or the single component of T_x^β, T_y^β and T_z^β. Such a linear combination with the equivalent weight is possible to be realized if the compound is pure. In the systems with lower Ce concentration as in the present case, the cubic symmetry is largely broken. Then, $T_x^\beta + T_y^\beta + T_z^\beta/\sqrt{3}$ is possible to be modified. Here, we consider the following two cases as the modified order parameter. (i) $T_x^\beta + T_y^\beta/\sqrt{2}$. (ii) T_z^β. We have performed the mean field calculation for the these order parameters. The Hamiltonian used in the present calculation is as follows.

$$\mathcal{H} = \mathcal{H}_{T_\beta} + \mathcal{H}_{\text{Zeeman}} \tag{6.1a}$$

$$\mathcal{H}_{T_\beta} = -K_\beta \sum_{ij} \mathbf{T}_\beta(i) \cdot \mathbf{T}_\beta(j), \tag{6.1b}$$

$$\mathbf{T}_\beta = \begin{cases} T_x^\beta + T_y^\beta/\sqrt{2} & \text{case (i)} \\ T_z^\beta & \text{case (ii)} \end{cases}$$

In the present calculation, we chose K_β so as to reproduce $T_{\text{oct}}^\beta = 1.7$ K, which is T_{IV-I}, of $Ce_{0.75}La_{0.25}B_6$. The calculated results of the T dependence of M and the energy levels for the above two cases are shown in
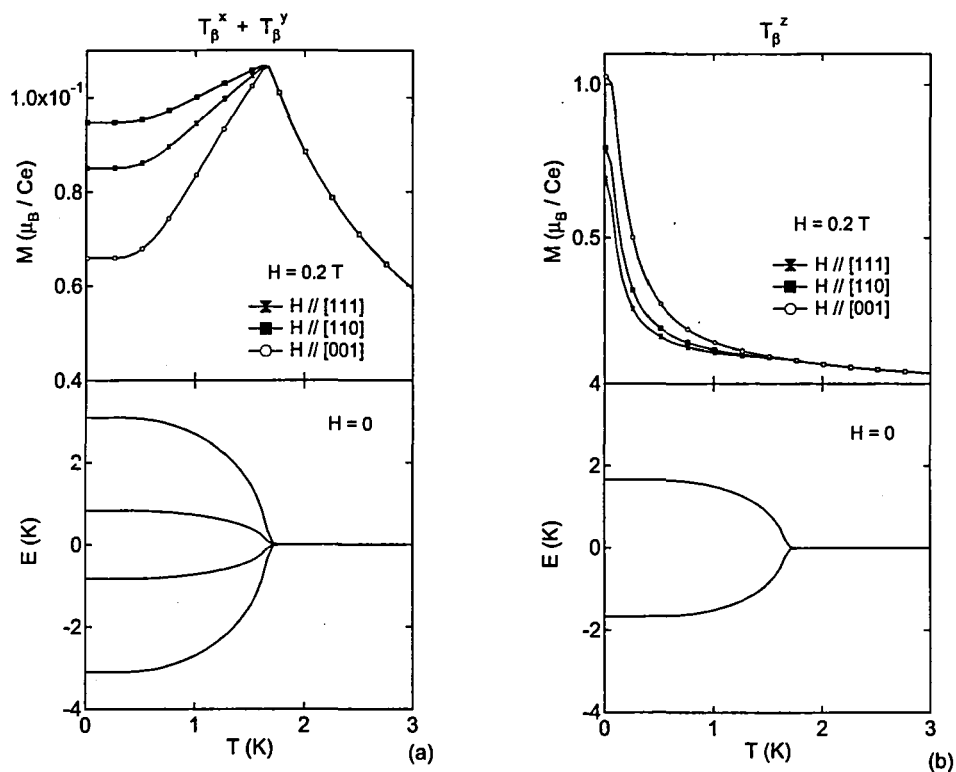
Fig. 6.3   Calculated results of the temperature dependence of the magnetization and the energy levels. The order parameter is (a) $T_x^\beta + T_y^\beta/\sqrt{2}$ and (b) T_z^β .

Fig. 6.3. In the case of (i), the ground state is the nonmagnetic singlet and the behaviors similar to the case of $T_x^\beta + T_y^\beta + T_z^\beta/\sqrt{3}$ are obtained as shown in Fig. 6.3. In the case of (ii), the ground state is the doublet and the Curie like behavior is obtained below the ordering temperature.

Thus, any of three types of the order parameters could not explain the present experimental results. In order to clarify the origin of the enhancement of T_{IV-I} by Nd and Pr doping in $Ce_x La_{1-x}B_6$ ($x \leq 0.5$), further studies, especially, the microscopic studies such as the neutron and X-ray diffractions are necessary.

Chapter 7

Conclusion

We have studied the physical properties of $Ce_x R_y La_{1-x-y} B_6$ in order to obtain the information on the order parameter of phase IV. We have also carried out the mean field calculation for the two-sublattice model in which the different kinds of the multipole interactions are taken into account in order to clarify the effect of the O_{xy}-AFQ and T_{xyz}-AFO interactions on the Γ_{5u}-type AFO ordering which is said to be the strong candidate of the LRO in phase IV in $Ce_x La_{1-x} B_6$. The obtained conclusions in the present study are follows.

· Mean Field Calculation for the Two-sublattice Model

1. We have performed the mean-field calculation for the two-sublattice model in which the Γ_{5u}-AFO, O_{xy}-AFQ, T_{xyz}-AFO and the AF exchange interactions are taken into account in order to clarify the effect of the latter interactions on the Γ_{5u}-AFO ordering. We found that a peak of the magnetic susceptibility in T_β-AFO phase which is one of the most characteristic properties in phase IV disappears easily by introducing the O_{xy}-AFQ interaction. This is because the O_{xy}-FQ order that accompanies the Γ_{5u}-AFO order is easily suppressed by the existence of the O_{xy}-AFQ interaction. Thus, we found that it is difficult to explain the overall properties of $Ce_x La_{1-x} B_6$ system containing phase IV at least only by assuming the T_β-AFO order in phase IV.

R-ion Doping Effect on Phase IV of $Ce_x La_{1-x} B_6$

1. For $x \geq 0.6$, phase IV is rapidly suppressed and phase III is stabilized by a small amount of R doping. The stabilization of phase III by R doping indicates that the R ions contribute to the formation of the AF magnetic order in phase III cooperatively with Ce ions. In addition, T_{IV-I} is independent of the y value and smoothly connects T_N as a function of y. This suggests the existence of some relationship between the order parameters of phases IV and III.

2. For $x \leq 0.5$, T_{IV-I} is largely enhanced by the R-ion doping, different from the rapid suppression for $x \geq 0.6$. This result indicates that the R ions have a role to stabilize phase IV for $x \leq 0.5$, and that the nature of phase IV for $x \geq 0.6$ is different from that for $x \leq 0.5$. The enhancement of T_{IV-I} and T_N by R-ion doping should originate from the contribution of the dipole moment of Nd and Pr ion in the stabilization in phase IV. If phase IV below $x = 0.5$ is Γ_{5u}-type AFO order as is proposed in phase IV for $x = 0.7$, the ground state is a nonmagnetic singlet. In this case, the dipole magnetic moment of Nd and Pr ion cannot couple with the Γ_{5u}-type octupole moment and does not enhance T_{IV-I}. By considering the possibility that phase IV is rapidly replaced by phase III by R doping due to the small energy difference between phase IV and III for $x \geq 0.6$, it is possible to say that the intrinsic nature of the interaction between the LRO in phase IV and the magnetic moment of R ion is seen for $x \leq 0.5$ where the energy difference between phase IV and III is large. Thus, we found that phase IV for $x \leq 0.5$ is stabilized by the magnetic moment of the doped R ion and pointed out the difficulty in the Γ_{5u}-type AFO order for phase IV. The possibility that the nature of phase IV is different between $x \geq 0.6$ and

$x < 0.5$ was pointed out.

Although the order parameter in phase IV was not determined definitely in the present study, we have got the big progress in the understanding of phase IV of $Ce_xLa_{1-x}B_6$. In order to clarify the origin of the enhancement of T_{IV-I} by Nd and Pr doping in $Ce_xLa_{1-x}B_6(x \leq 0.5)$, further studies, especially, the microscopic studies such as the neutron and X-ray diffractions are necessary.

Bibliography

[1] E. Zirngiebel, B. Hillebrands, S. Blumenroder, G. Guntherodt, M. Loewenhaupt, J. M. Carpenter, K. Winzer and Z.Fisk : Phys. Rev. B. **30** (1984) 4052.

[2] R. Shiina, H. Shiba and P. Thalmeier : J.Phys. Soc. Jpn. **66** (1997) 1741.

[3] http://home.hiroshima-u.ac.jp/matsumura/Research_files/quad.pdf

[4] S. Kobayashi : Doctoral Thesis in Hiroshima University (2002)

[5] M. Sera : Kotai Butsuri. 4 (2000) 229 [in Japanese].

[6] P. Link, A. Gukasov, J. M-Mignot, T. Matsumura and T. Suzuki: Phys. Rev. Lett. **80** (1998) 4779.

[7] H. Yamauchi, H. Onodera, K. Ohoyama, T. Onimaru, M. Kosaka, M. Ohashi and Y. Yamaguchi: J. Phys. Soc. Jpn. **68** (1999) 2057.

[8] T. Tayama, T. Sakakibara, K. Kitami, M. Yokoyama, K. Tenya, H. Amitsuka, D. Aoki, Y. Onuki and Z. Kletowski: J. Phys. Soc. Jpn. **70** (2001) 248.

[9] M. Kohgi, K. Iwasa, M. Nakajima, N. Metoki, S. Araki, N. Bernhoeft, J.-M. Mignot, A. Gukasov, H. Sato, Y. Aoki and H. Sugawara: J. Phys. Soc. Jpn. **72** (2003) 1002.

[10] C. Schwartz: Phys. Rev. **97** (1955) 380.

[11] H. Kusunose and Y. Kuramoto : Kotai Butsuri. 9 (2006) 597 [in Japanese].

[12] Y. Murakami, H. Kawada, H. Kawata, M. Tanaka, T. Arima, Y. Moritomo, and Y. Tokura : Phys. Rev. Lett. **80** (1998) 1932.

[13] J.A. Paixao, C. Detlefs, M.J. Longfield, R. Caciuffo, P. Santini, N. Bernfoeft, J. Rebizant and G.H. Lander : Phys. Rev. Lett. **89** (2002) 187202.

[14] A. Kiss and P. Fazekas : Phys.Rev.B. **71** (2005) 054415

[15] M. Yoshizawa, Y. Nakanishi, M. Oikawa, C. Sekine, I. Shirotani, S.R. Saha, H. Sugawara and H. Sato : J. Phys. Soc. Jpn. **74** (2005) 2141.

[16] A. Takase, K. Kojima, T. Komatsubara and T. Kasuya : Solid State commun. 36 (1980) 461.

[17] J.M.Effantin, J. Rossat-Mignod, P. Burlet, S. Kunii and T. Kasuya : J.Magn. Magn.Master. **47&48** (1985) 145.

[18] T. Goto, A. Tamaki, S. Kunii, T. Nakajima, T. Fujimura, T. Kasuya, T. Komatsubara and S. B. Woods : J.Magn. Magn.Master. **47&48** (1983) 419.

[19] T. H. Geballe, B. T. Matthias, K. Andres, J. P. Maita, A .Cooper and E. Corenzwit : Science. 160 (1968) 1443.

[20] J. C. Nickerson and R. M. White : J.Appl.phys. **40** (1969) 1011.

[21] K. N. Lee and B. Bell : Phys.Rev.B. **6** (1972) 1032.

[22] T . Fujita, M. Suzuki, T. Komatsubara, S. Kunii, T .Kasuya and T. Ohtsuka : Solid State Commun. 35 (1980) 569.

[23] N. Sato, S. Kunii, I. Oguro and T. Kasuya : J.Phys. Soc. Jpn. **53** (1984) 3967.

[24] K. Hanzawa et al : High Field Magnetism,ed.M.Date (North-Holland,Amsterdam) (1982) 171.

[25] W. A. C. Erlelents, L. P. Renault, P. Burlet, J. Rossat-Mignod, S. Kunii and T. Kasuya : J.Magn. Magn.Master. **63&64** (1987) 61.

[26] M. Takigawa, H. Yasuoka, T. Tanabe and Y. Ishizawa: J. Phys. Soc. Jpn. **52** (1983) 728.

[27] K. Ueda and Y. Ōnuki : *Physics of Heavy Electron Systems* (Shokabo, Tokyo, 1998) [in Japanese].

[28] F. J. Ohkawa : J.Phys.Soc.Jpn. **52** (1983) 3897.

[29] R. Shiina, H. Shiba and P. Thalmeier : J.Phys. Soc. Jpn. **67** (1998) 941.

[30] M. Hiroi, M. Sera, N. Kobayashi and S. Kunii : Phys. Rev. B. **55** (1997) 8339.

[31] M. Hiroi, S. Kobayashi, M. Sera, N. Kobayashi and S. Kunii : Phys. Rev. Lett. **81** (1998) 4243.

[32] Y. Kuramoto and N. Fukushima : J. Phys.Soc.Jpn. **67** (1997) 583.

[33] O. Sakai, R. Shiina, H. Shiba and P. Thalmeier : J. Phys. Soc. Jpn. **66** (1997) 3005.

[34] M. Sera and S. Kobayashi : J. Phys. Soc. Jpn. **68** (1999) 1664.

[35] T. Furuno, N. Sato, S. Kunii, T. Kasuya and W. Sasaki : J. Phys. Soc. Jpn. **54** (1985) 1899.

[36] M. Loewenhaupt and M. Prager : Z. Phys. B **62** (1986) 195.

[37] C. M. McCarthy and C. W. Thompson : J. Phys. Chem. Solid **41** (1980) 1319

[38] M. Sera, S. Itabashi and S. Kunii : J. Phys. Soc. Jpn. **66** (1997) 548

[39] S. Awaji, N. Kobayashi, S. Sakatsume, S. Kunii and M. Sera : J. Phys. Soc. Jpn. **68** (1999) 2518.

[40] S. Tsuji, T. Endo, M. Sera, K. Kojima, M. Kawakami and S. Kunii : J. Phys. Soc. Jpn. **69** (2000) 1974

[41] Y. Yoshino, S. Kobayashi, S. Tsuji, H. Tou, M. Sera, F. Iga, Y. Zentani and J. Akimitsu : J. Phys. Soc. Jpn. **73** (2004) 29

[42] J.-M. Mignot, J. Robert, G. André, M. Sera and F. Iga : Phys. Rev. B **79** (2009) 224426

[43] S. Kobayashi, Y. Yoshino, S. Tsuji, M. Sera and F. Iga : J. Phys. Soc. Jpn. **72** (2003) 25.

[44] M. Sera, F. Iga, S. Kobayashi, H. Sugamoto, K. Nagatomo, K. Umeo, S. Tsuji, K. Kojima, J. Akimitsu and Y. Zenitani : *Proc. Int. Conf. Strongly Correlated Electrons with Orbital Degrees of Freedom (ORBITAL2001)*, J. Phys. Soc. Jpn. **71** (2002) Suppl., p. 52

[45] S. Kobayashi, M. Sera, M. Hiroi, T. Nishizaki, N. Kobayashi and S. Kunii: J. Phys. Soc. Jpn. **70** (2001) 1721

[46] P. Burlet, J. M. Effantin, J. Rossat-Mignod, S. Kunii and T. Kasuya : J. Phys. (Paris) C **8** (1988) 459.

[47] S. Kishimoto, A. Kondo, M.-S. Kim, H. Tou, M. Sera and F. Iga : J. Phys. Soc. Jpn. **74** (2005) 2913

[48] J.-M. Mignot, G. Andree, J. Robert, M. Sera, and F. Iga : : Phys. Rev. B **78** (2008) 014415

[49] S. Nakamura, T. Goto and S. Kunii : J. Phys. Soc. Jpn. **64** (1995) 3941.

[50] S. Kobayashi, M. Sera, M. Hiroi, N. Kobayashi, and S. Kunii: J. Phys. Soc. Jpn. **69** (2000) 926.

[51] S. Kobayashi, Y. Yoshino, S. Tuji, H. tou, M. Sera and F. Iga : J. Phys. Soc. Jpn. **72**(2003) 2947.

[52] O. Suzuki, T. Goto, S. Nakamura1, T. Matsumura and S. Kunii : J. Phys. Soc. Jpn. **67** (1998) 4243.

[53] T. Tayama, T. Sakakibara, K. Tenya, H. Amitsuka and S. Kunii : J. Phys. Soc. Jpn. **66** (1997) 2268.

[54] M. Hiroi, S. Kobayashi, M. Sera, N. Kobayashi, S. Kunii *et al* : J. Phys. Soc. Jpn. **66** (1997) 1762.

[55] M. Hiroi, S. Kobayashi, M. Sera, N. Kobayashi and S. Kunii: J. Phys. Soc. Jpn. **67** (1998) 53

[56] T. Sakakibara, K Tenma, M. Yokoyama and H. Amitsuka : *Proc. Int. Conf. Strongly Correlated Electrons with Orbital Degrees of Freedom (ORBITAL2001)*, J. Phys. Soc. Jpn. **71** (2002) Suppl., 48.

[57] M. Akatuka, T.Goto, Y. Nemoto, O. Suzuki, S. Nakamura and S. Kunii : J. Phys. Soc. Jpn. **72** (2002) 205.

[58] P. Fischer, K. Iwasa, K. Kuwahara, M. Kohgi, T. Hansen, and S. Kunii: Phys. Rev. B **72** (2005) 014414.

[59] K. Magishi, M. Kawakami, T. Saito, K. Koyama, K. Mizuno, and S. Kunii: Z. Naturforsch. A **57a** (2002) 441.

[60] H. Takagiwa, K. Ohishi, J. Akimitsu, W. Higemoto, R. Kadono, M. Sera, and S. Kunii: J. Phys. Soc. Jpn. **71** (2002) 31.

[61] K. Kuwahara, K. Iwasa, M. Kohgi, N. Aso, M. Sera, and F. Iga : J. Phys. Soc. Jpn. **76** (2007) 093702

[62] R. Shiina, O. Sakai and H. Shiba : J. Phys. Soc. Jpn. **76** (2007) 094702

[63] D. Mannix, Y. Tanaka, D. Carbone, N. Bernhoeft, and S. Kunii: Phys. Rev. Lett. **95** (2005) 117206.

[64] H. Kusunose and Y. Kuramoto: J. Phys. Soc. Jpn. **70** (2001) 1751.

[65] K. Kubo and Y. Kuramoto : J. Phys. Soc. Jpn. **73** (2004) 216.

[66] T. Morie, T. Sakakibara, T. Tayama, and S. Kunii: J. Phys. Soc. Jpn. **73** (2004) 2381.

[67] H. Kusunose and Y. Kuramoto: J. Phys. Soc. Jpn. **74** (2005) 3139.

[68] http://home.hiroshima-u.ac.jp/matsumura/Research_files/resoXray1227.pdf

[69] S. Kobayashi and Y. Otsuka : *Teion Gijutsu* (University of Tokyo Press, 1998) [in Japanese].

[70] T. Sakakibara, H. Mitamura, T. Tayama and H. Amitsuka: Jpn. J. Appl. Phys. **33** (1994) 5067.

[71] A. Tamaki, T. Goto, M. Yoshizawa, T. Fujimura, S. Kunii, and T. Kasuya: J. Magn. Magn. Mater. **52** (1985) 257.

[72] M. Sera, S. Itabashi, and S. Kunii : J. Phys. Soc. Jpn. **66** (1997) 548.

[73] H. Tanida *et al.* : private communication.

[74] T. Tayama, S. Honma, K. Tenya, H. Amitsuka, T. Sakakibara, and S. Kunii : physica B **259-261** (1999) 32.

[75] Y. Nemoto, M. Akatsu, T. Goto, O. Suzuki, S. Nakamura and S. Kunii : Physica B **312-313** (2002) 191.

[76] S. Ikeda : Master's thesis in Hiroshima University (2007).

Acknowledgment

公表論文

(1) Comments on the Hidden Order in Phase IV of $Ce_xLa_{1-x}B_6$
A. Kondo, H. Tou, M. Sera, and F. Iga
J. Phys. Soc. Jpn. **76** (2007) 013701.

(2) Rapid Suppression of Phase IV by Nd Doping in $Ce_{0.7}La_{0.3}B_6$
A. Kondo, H. Tou, M. Sera, F. Iga, and T. Sakakibara
J. Phys. Soc. Jpn. **76** (2007) 103708.

(3) Stabilization of phase IV in $Ce_xLa_{1-x}B_6$ (x=0.4, 0.5) by Pr and Nd ion doping
A. Kondo, T, Taniguchi, H. Tanida, T. Matsumura, M. Sera, F. Iga, H. Tou,
T. Sakakibara and S. Kunii
To be published in J. Phys. Soc. Jpn. **78** No.9.

(4) Nd-doping effect on phase IV of $Ce_xLa_{1-x}B_6$
A. Kondo, H. Tou, M. Sera and F. Iga
Physica B **383** (2006) 35.

(5) Magnetic rare-earth ion doping effect on phase IV of $Ce_{0.7}La_{0.3}B_6$
A. Kondo, H. Tou, M. Sera, F. Iga, T. Morie and T. Sakakibara
Magn. & Magn. Mater **310** (2007) e160

(6) Suppression of Phase IV in $Ce_xLa_{1-x}B_6$ by R-Ion Doping
A. Kondo, H. Tou, M. Sera, F. Iga, and T. Sakakibara
J. Phys. Soc. Jpn. **77** (2008) Suppl. A 285